PROGRESS IN DEVELOPING AN OVARIAN CANCER SCREEN BASED ON WHISPERING GALLERY MODE IMAGING

By

Heath A. Huckabay
B.S., Sam Houston State University, 2006

Submitted to the Department of Chemistry and the Faculty of the Graduate School of the University of Kansas in partial fulfillment of the requirements for the degree of Doctor of Philosophy

_____
Robert C. Dunn, Ph.D. (Chairman)

_____
Richard S. Givens, Ph.D.

_____
Mario Rivera, Ph.D.

_____
David D. Weis, Ph.D.

_____
Wonpil Im, Ph.D.

Date Approved: March 15, 2012

The Dissertation Committee for Heath A. Huckabay certifies
that this is the approved version of the following dissertation:

PROGRESS IN DEVELOPING AN OVARIAN CANCER SCREEN BASED ON WHISPERING GALLERY MODE IMAGING

Committee:

_____
Robert C. Dunn, Ph.D. (Chairman)

_____
Richard S. Givens, Ph.D.

_____
Mario Rivera, Ph.D.

_____
David D. Weis, Ph.D.

_____
Wonpil Im, Ph.D.

Date Approved: March 15, 2012

Abstract

Despite considerable research devoted to identifying biomarkers for ovarian cancer, no screening method is currently available for routine early detection of the disease. While highly treatable in its early stages, a lack of symptoms early in the disease progression often results in the cancer spreading to other tissues before being diagnosed, significantly reducing the survival rate. CA-125 is currently the most common biomarker used for the detection of ovarian cancer; however its poor diagnostic reliability when measured alone necessitates the use of a multiplexed biomarker screen for accurate early-stage diagnosis. Numerous protein biomarkers have been identified for this purpose as well as small, noncoding oligonucleotides referred to as microRNAs. New assays for screening this combination of multiple analyte types require the capability of detecting any class of target, including proteins and nucleic acids.

This work describes progress in developing a label-free, multiplexed assay for the early detection of ovarian cancer. The instrumental approach exploits tiny microresonators that take advantage of a phenomenon referred to as whispering gallery mode (WGM) resonances. This method is based on the ability of circular dielectrics to store light through continuous total internal reflection, where the wavelengths stored are dependent upon the surrounding refractive index. By attaching capture agents to the sensor surface, binding events change the local RI and shift the resonant wavelength which can be used to quantify analyte binding. To combine the favorable attributes of two traditional WGM techniques, in Chapter 2 we introduce a new approach for biosensing which combines microsphere WGM resonators with fluorescence imaging to create a flexible platform for multiplexed biosensing. It is shown that the multiplexing capability is vastly increased using this imaging technique as compared to other WGM methods, enabling the detection of multiple targets in a single assay. The feasibility of using this method for biomarker measurement is demonstrated by detecting two

biomarkers linked to ovarian cancer pathogenesis, CA-125 and tumor necrosis factor-α. To advance the WGM imaging technique toward clinical use, we show in Chapter 3 that non-specific binding is not limiting by detecting CA-125 doped into serum samples. The eventual clinical utility of this approach is illustrated by measuring CA-125 levels in serum collected from a healthy donor and a patient diagnosed with ovarian cancer.

Although whispering gallery detection is effective in biomarker measurement, in practice the sensing region covers a very small area. As in all label-free assays, non-specific binding can be an issue for WGM detection and it is desirable that all immobilized antibodies be active. It is crucial, therefore, that all capture antibodies are immobilized in the appropriate orientation for efficient analyte binding. To maximize sensor performance, therefore, new techniques capable of characterizing antibody orientation at the single molecule level are required. A new approach for measuring single antibody orientations is therefore introduced and validated in well-characterized test systems using model lipid membranes.

It has been shown that polarized total internal reflection fluorescence microscopy (PTIRF-M) is capable of directly determining the three-dimensional orientation of single molecules. Using Langmuir-Blodgett monolayers of DPPC, we show in Chapter 5 that these orientations can be used to track membrane structure at the molecular level. We utilize this to find the characteristic "equivalent surface pressure" between lipid monolayers formed by Langmuir-Blodgett deposition and supported lipid bilayers formed by vesicle fusion. The single molecule approach is further explored by comparing the condensing effects of sterol additives in each system. These measurements show that orientations respond to the addition of condensing sterols, further supporting the notion that this technique can track structural changes at the molecular level. As future single-molecule work will be used to determine antibody orientations in a dynamic, fluid environment, it is important to explore the time-

resolved capabilities of this approach. In Chapter 6 we show that single molecule orientational changes can be captured with ~1s temporal resolution. By increasing the hydration levels of model membrane systems through changes in relative humidity, we show that both structural and dynamic changes occur within the membrane at the molecular level. In addition, it was observed that this technique is capable of measuring three-dimensional orientational changes in real time. Future goals include employing this method to probe antibody orientations on substrates in situ, so these studies are an important step for understanding how the technique may be applied in fluidic systems.

Acknowledgements

While many of my accomplishments to date have been in part due to my own efforts, none of my success would be possible without the help of others. In the context of graduate school, I owe a great deal of thanks to my advisor, Bob Dunn. He has been instrumental in encouraging me to solve problems with a keen eye, he has challenged me intellectually, and he has pushed me to think creatively. In addition, he has provided a work environment that has allowed me to work independently when I need space, and to have guidance when I hit dead ends. For all of this, Bob, I thank you for your support.

I would also like to thank the members of the Dunn group for their friendship, and for being there when I needed someone to bounce ideas off of. When I first joined the lab, I was warmly welcomed by two excellent students, Nick Dickenson and Phil Livanec, who both shared their knowledge and helped give me the initial skills necessary for graduate work, to which I am very grateful. Since their departure, I have had the pleasure of working with Kevin Armendariz. We've had many useful conversations over the years to get through the many challenges of novel research, and I wish him the best in completing his own work. Recently, the addition of three graduate students to our lab, Sarah Wildgen, Will Newhart, and Daniel Kim, has shown me that the quality of work being performed in this lab will continue for years to come. I thank you all for your support during my graduate career, and I'm confident you'll be successful in your careers.

Here at KU, the faculty and staff of the chemistry department are exceptional, and I owe them all thanks for their support during these past years. With the knowledge and skills gained from the faculty through my studies, I feel that I am well prepared to tackle any future challenges that I'll come across. I should say, though, that none of my accomplishments would be remotely possible if it weren't for the support staff here at KU. These people are the fundamental gears of the department, they deserve the greatest of respect, and I am in their debt for their efforts. Specifically, I would like to thank

Sonjia Payne, Jan Akers, Terrie Lindholm, Bev Johnson, Yvonne Martinez, Patricia McCaffrey, Susan Teague, Jill Headrick, Ann Smith, and Gary Webber. Through my graduate career, I've known that if I needed something done, these were the people to rely on. I appreciate everything you've done for me, and I hope that in my future endeavors I work with a support staff that is as helpful as you have been.

In addition to my studies here at KU, I've had the opportunity to garner numerous valuable friendships. Spending time with these people has made life as a graduate student a little easier, and I'll remember the great times we've had for the rest of my life. Specifically, I'd like to thank Phil and Maggie Livanec, Carl Cooley, Megan Dorris, Tom Linz, Dan Clark, Sam Alnasleh, Kevin Armendariz, and Sarah Wildgen. It's been a joy to spend the time we've had together, and while we'll all eventually go our own way, I hope to keep in touch and get together from time to time. Thank you for making my time at KU a great experience.

I would like to thank my family for their unconditional support. If it weren't for the opportunities given to me by my parents, I would not be here today. I was taught not to squander these opportunities, and I think that has pushed me to achieve great things thus far, and hopefully great things to come. Mom, thank you for your unwavering confidence in me, and your unending support. You have my utmost gratitude.

And last, but definitely not least, I would like to thank my wife, Emily, for coming with me to KU and supporting me through the good times and bad. You have joined me in my brightest days and been there for me in my darkest hours, through thick and thin. The amount of love and support you've given me through these times cannot appreciably be put into words. You've kept me above water in so many situations; I honestly think I couldn't have made it through this without you. I thank you, I love you, and I look forward to spending the rest of my life with you.

Table of Contents

List of Figures

List of Tables

Chapter 1: Introduction and Overview

1.1 Ovarian Cancer

Ovarian cancer is both the most prevalent and deadly gynecological malignancy.[1, 2] While it accounts for only ~3% of cancer cases in women, it is the fifth-leading cause of cancer related death, carrying a 1-in-70 lifetime risk and exhibiting a 60% fatality rate.[1, 2] This fatality rate is not solely related to the aggressiveness of the disease, however, as the cancer is entirely treatable if caught early in its progression. Consider the following graph, which illustrates the 5-year survival rate of women versus their diagnosed stage of ovarian cancer:

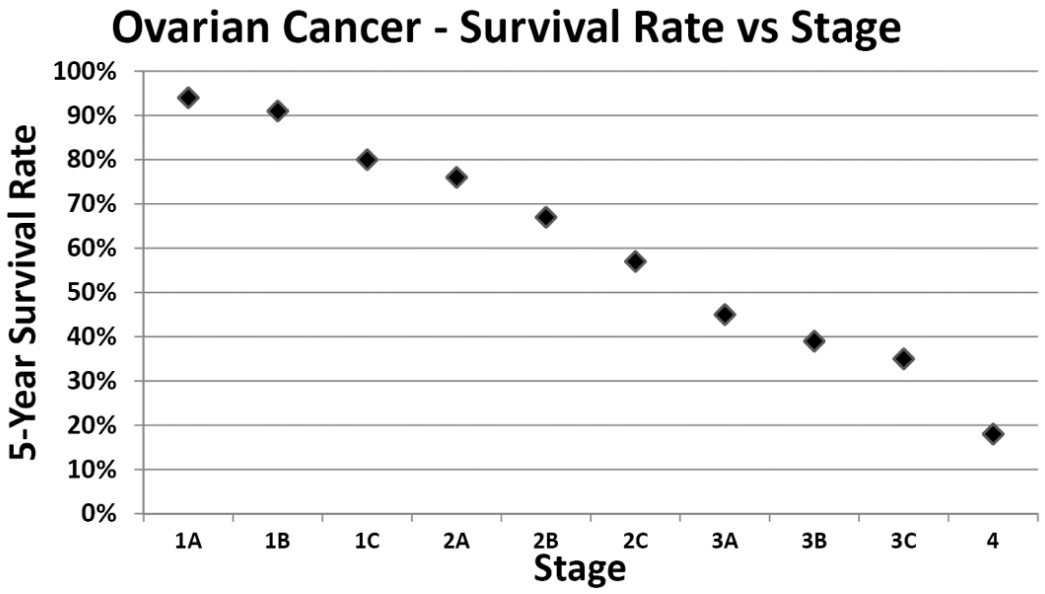

Figure 1.1: Ovarian cancer 5-year survival rate versus stage of diagnosis.

Clearly, the early stages of this cancer are highly treatable, with survival rates of over 90%.[1, 3, 4] These rates steadily decline from ~75%-35% between stages 2-3, until the disease advances well beyond the ovaries and invades other tissues, reaching a 5-year survival rate below 20% in stage four.[2, 4, 5]

What makes this disease a major issue facing society is the lack of early screens that enable routine detection. A number of factors combine to make this disease elusive to diagnose at a more treatable stage. Ovarian cancer is asymptomatic in its early stages when the malignant tissue is largely confined to the ovaries. This complicates early detection since the lack of early symptoms provides no

warning to screen during routine examinations. When symptoms finally do appear, cancer progression makes surgical interventions difficult and much less effective at eliminating the infected tissue. Because of the largely asymptomatic nature of ovarian cancer in early stages, over 70% of cases are diagnosed in some advanced stage, contributing to the difficulty of treatment.[6] Clearly, new approaches that enable routine screening for early stage ovarian cancer are needed.

1.2 Detection Methods in Ovarian Cancer Screening

1.2.1 The Physical Approach for Ovarian Cancer Detection

While early detection of this disease is difficult, physical methods can be used to aid in finding infected tissue.[7] The physical approach involves the use of a pelvic ultrasound to image the ovaries. Abnormal masses of ~1cm or greater can be detected using this approach which can lead to further exams such as serum sampling or a biopsy. While this technique is simple to perform and can be done in a point-of-care setting, it faces a number of issues. The method is inherently problematic in that it can only detect tumors after they reach ~1cm in size.[8] While locating tumors of this size confined to the ovaries would place diagnosis at stage 1, our goals are to push the point of diagnosis to the earliest point possible. More importantly, this method is highly invasive, so it is not performed routinely and is utilized only after symptoms appear. This pushes the stage of diagnosis to a later point, where successful treatment is much more difficult to achieve. Although easy to perform and helpful for tumor detection, the physical approach is ill suited for routine screening and, therefore, early diagnosis. This has motivated the ongoing effort to identify protein and other biomarkers in serum that correlate with the onset of disease pathogenesis.

1.2.2 Biomarkers for Ovarian Cancer Detection

The most widely utilized biomarker for detection of ovarian cancer is cancer antigen 125, or CA-125.[5, 9-15] While this protein biomarker is present in all women, its serum concentration is elevated in 60% of women with ovarian cancer and 80% of women with disseminated ovarian cancer.[1, 4, 5, 12, 16-18]

Detecting elevated concentrations may be indicative of disease progression, but CA-125 is also elevated in 1% of healthy women, 3% with nonlethal ovarian diseases, and 6% with benign conditions such as pregnancy or menstruation.[16-19] If only CA-125 concentration is measured, therefore, the false positive rate would be above medically acceptable levels. To develop an early screen for ovarian cancer, multiple biomarkers must be measured routinely for effective diagnostic capability.

Since it is generally agreed that CA-125 levels alone are insufficient for early diagnosis of ovarian cancer, new and reliable targets must be identified. Research in this field has found numerous candidate biomarkers; however, no single target has been found that exhibits the requisite diagnostic relevance. To illustrate this problem, let us consider Table 1.1, which lists some identified potential targets for diagnostic use.

Table 1.1: Candidate biomarkers for ovarian cancer and their diagnostic capabilities.

Biomarker	Sensitivity	Specificity	Notes
Protein			
Cancer antigen-125	61% (Stage 1-2)	86% (Stage 1-2)	The most commonly screened protein for ovarian cancer diagnosis. Poor performance alone. [5, 9-15]
HE4	86% (Stage 1)	60% (Stage 1)	Recently FDA approved for post-surgical relapse monitoring.[20]
Osteopontin	70%	90%	Up-regulated in early stage cancer. Also implicated in cardiovascular disease.[21]
Cathepsin L	80%	85%	Elevated in ~80% of patients with Stage 1 carcinoma.[22]
OVX-1	40%	80%	Elevated in Stage 1 carcinoma. Also implicated in breast and prostate cancer.[23]
CA-72-4	54%	91%	Also elevated in numerous cancers, such as breast, colon, pancreatic, and gastric carcinoma.[23]
Prolactin	42% (Stage 1+2)	90% (Stage 1+2)	Also correlates with seizures, and breast, prostate, and colon cancers.[21]
micro RNA			
miR-342-3p	80%	90%	Down-regulated in ovarian cancer.[24]
miR-141	--	--	While the sensitivity & specificity were not reported, miR's 141, 200a, and 205 were shown to be differentially expressed between healthy and diseased patients to a significant degree starting at stage 1 of ovarian carcinoma.[25]
miR-200a	--	--	
miR-205	--	--	

In Table 1.1, diagnostic sensitivity is the probability of a test producing a true positive (positive test on an ill patient), defined as:[26]

$$Sensitivity = \frac{\#\ of\ true\ positives}{\#\ of\ true\ positives + \#\ of\ false\ negatives} \quad \text{Eq. 1.1}$$

The diagnostic specificity is the probability of a test producing a true negative (negative test on a healthy patient), given by:[26]

$$Specificity = \frac{\#\ of\ true\ negatives}{\#\ of\ true\ negatives + \#\ of\ false\ positives} \quad \text{Eq. 1.2}$$

Finally, the positive predictive value (PPV) of a test is the probability that a person is actually infected when a positive result is seen.[27] This is represented by:

$$PPV = \frac{\#\ of\ true\ positives}{\#\ of\ true\ positives + \#\ of\ false\ positives} \quad \text{Eq. 1.3}$$

The PPV is a defining quantity in the search for a successful screening strategy. The consensus of researchers in clinical diagnostics is that in order for an assay to be acceptable for use in the general population, it must exhibit a PPV of 10%, translating to no more than nine false positives for each true positive.[28] To reach a 10% PPV in the population of postmenopausal women who exhibit an ovarian cancer incidence of 40/100,000 per year, an acceptable assay for the disease must achieve a minimum of 99.6% specificity.[28, 29] Considering the specificities outlined in Table 1.1, this stringent requirement is challenging for any single biomarker identified thus far. It is these statistics that has led the clinical diagnostics community to agree that an assay which combines the measurement of multiple biomarkers is necessary for reliable routine ovarian cancer screening.

1.2.3 The Enzyme-Linked Immunosorbent Assay (ELISA)

A common assay employed for biomarker detection is the enzyme-linked immunosorbent assay, or ELISA.[30] The method is based on the capture and subsequent detection of target proteins in biofluids utilizing antibody-antigen interactions which is outlined schematically in Figure 1.2.

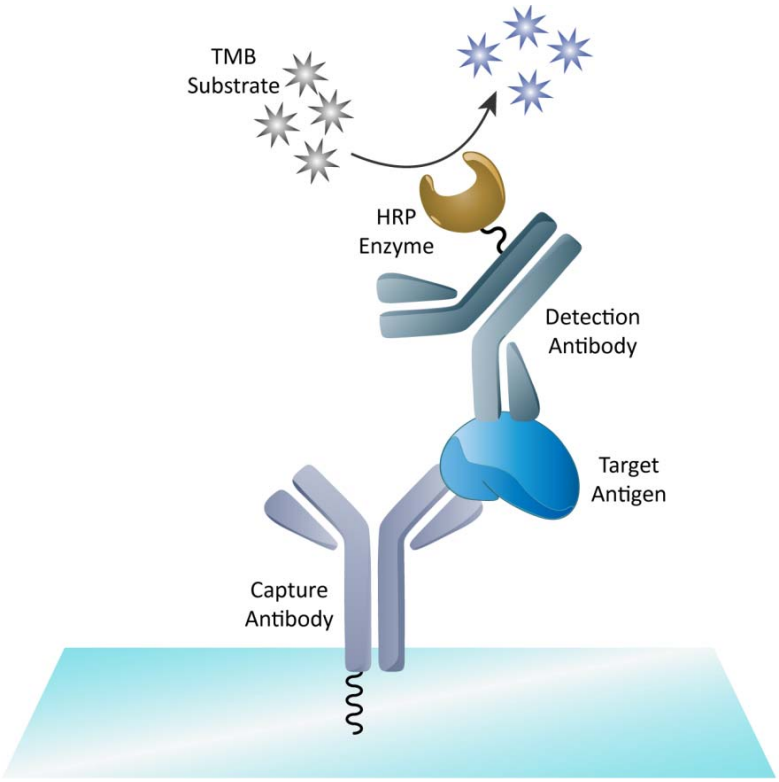

Figure 1.2: Sandwich-based ELISA method.

By incubating a sample solution with the immobilized antibody, antigen affinity to the bound immunogen will capture the target on the substrate surface. After binding occurs, a secondary antibody bound to an enzyme, such as horseradish peroxidase (HRP), is incubated with the antibody-antigen complex. Following incubation, the captured antigen is "sandwiched" between the two antibodies, leaving the enzyme exposed to the surrounding buffer. By adding a reagent such as 3,3',5,5'-tetramethylbenzidine (TMB) in the presence of hydrogen peroxide, HRP catalyze oxidation leads to the formation of a diimine product with a λ_{max} of 450nm.[31] The reaction is halted after adding an acidic stop reagent. The measured absorbance at 450nm is then compared to a calibration curve and used to determine the protein concentration.

1.2.4 ELISA Advantages

The ELISA approach is widely accepted as the "gold standard" in the diagnostics community and has been utilized for many years due to its sensitivity, specificity, and robust nature. Through employing

enzyme-catalyzed detection, the signal from TMB oxidation is amplified relative to incubation time, resulting in low detection limits. Furthermore, by utilizing a secondary antibody for detection reduces cross-reactivity issues with the capture antibody, which increases analyte specificity. Finally, the entire procedure can be performed on multi-well plates, allowing for automated protein detection. These attributes make the ELISA technique appealing for biomarker measurement; however, the approach exhibits some serious drawbacks which make it challenging to implement in point-of-care settings for routine screening of ovarian cancer biomarkers.

1.2.5 ELISA Disadvantages

The first disadvantage with ELISA-based sensing is that it is considered a "one-shot" detection method: detection of each target analyte requires a separate assay. This creates logistical issues if the method is to be applied in routine multiplexed biomarker detection, as it scales poorly for point-of-care screening. Scalability is also affected by reagent requirements, as continuous monitoring would be costly if numerous assays are performed on a regular basis. Additionally, the immunoreactivity of the secondary antibody can be adversely affected by enzyme labeling. Taking these issues into account, the ELISA approach, while effective for single-target monitoring, is ill-suited to achieving the necessary performance requirements of a routine multiplexed assay in the point-of-care setting.

Clearly, new approaches are needed for routine screening which can monitor multiple biomarkers simultaneously. As there are a number of requirements to be addressed for such a screening technique, let us consider the attributes that an effective assay should exhibit.

1.3 Desired Performance Metrics for an Effective Ovarian Cancer Screening Assay

1.3.1 Multiplexed Biomarker Detection

The medical consensus is that a multiplexed biomarker assay capable of routine monitoring is required to achieve early diagnosis of ovarian cancer. As discussed in Section 1.2.2, a PPV of 10% or better must be achieved to have an assay reliable enough for screening of the general population.[28, 29]

This requires a biomarker diagnostic sensitivity of 99.6%, and as seen in Table 1.1, no single biomarker has yet been found which can satisfy this requirement.[28, 29] The assay must therefore be capable of multiplexed biomarker detection to achieve acceptable reliability.

1.3.2 Label-Free Detection

Referring back to Table 1.1, in addition to protein biomarkers for disease detection, recent work has suggested that small, noncoding ribonucleotides, called micro RNAs, can also act as signatures for ovarian cancer.[25, 32-34] Introducing non-protein targets presents an additional requirement for the assay in that it must be capable of detecting numerous classes of target materials. To achieve this type of detection, the most straightforward manner of sensing involves a label-free detection scheme. This approach avoids the additional chemistry required by introducing labels which can also lead to a loss of biomolecule function. Label-free detection, therefore, simplifies the chemistry and reduces the cost as fewer reagents are required. These approaches also provide more flexibility in analyte detection, increase the speed of the assay, and are amenable with the point-of-care environment.

1.3.3 Low Detection Limits

ELISA is considered the "gold standard" in clinical diagnostics, due in part to its low detection limits, generally in the pM range.[35] Our assay goals are to push these detection limits beyond the current capabilities of ELISA for several reasons. First, research has shown that not only the absolute level of CA-125 and other biomarker concentrations is important for diagnosing ovarian cancer, but very small changes over time are indicators of cancer progression or relapse.[36, 37] Also, the serum concentration of some identified biomarkers is either below the limits of detection in ELISA or totally absent in healthy individuals, so in order to capture their upregulation at the earliest stage of pathogenesis, we must strive to achieve the lowest limits of detection possible.[37]

1.3.4 Point-of-Care Amenability

In addition to multiplexed biomarker detection, routine screening is necessary for diagnosing ovarian cancer in its early stages since during this time it is largely asymptomatic. Numerous studies suggest that while the absolute concentration of biomarkers is important, the change of these levels over time both exhibits diagnostic importance and is helpful for monitoring the effectiveness of cancer treatment.[36, 37] The eventual technique must be easily carried out in point-of-care settings for incorporation into well-woman examinations. Since the goals of this method are to ultimately screen the general population, this stipulation requires that the approach be cost-effective.

1.4 A Comparison of Common Label-Free Approaches to Biomarker Detection

Considering the criteria outlined in Section 1.3, there are numerous label-free methods which could potentially satisfy our goals. The required criteria, such as good throughput, low cost, multiplexing capability and point-of-care applicability must all be taken into account when developing a screen. Listed in Table 1.2 are popular label-free methods which are commonly used in biomarker detection. In the following sections, we will consider each technique individually for comparison.

Table 1.2: Label-free approaches for biomarker detection.

Sensing Technique	Point of Care Applicability	Multiplexing Capability	Detection Limits	Throughput	Cost
SPR[38]*	Moderate	Good	uM-pM	Good	High
Ellipsometry[39]	Difficult	Moderate	nM-pM	Poor	Moderate
Interferometric Techniques[40]	Moderate	Poor	pM-fM	Poor	Moderate
Microcantilever Resonance[41]	Very Difficult	Poor	ng/mL	Good	High
Mass Spectrometry[42, 43]	Very Difficult	Good	µM-pM	Moderate	Very High
Optical Resonator Sensors[44]	Mixed	Mixed	µM to Single Molecule	Mixed	Moderate

*Surface Plasmon Resonance

1.4.1 Surface Plasmon Resonance

Surface plasmon resonance uses a metal coated dielectric material excited with incident laser light. The valence electrons in the metal layer will absorb the incident radiation if it matches their collective oscillations, termed plasmons. These resonances can be measured by examining the reflected light intensity as a function of reflection angle or wavelength.[45] The plasmons are sensitive to refractive index changes in the region directly surrounding the metal coating. By immobilizing capture materials such as antibodies on the metal surface, binding events may be measured in real time using this approach. This method has multiplexing capabilities and appreciable throughput if used in an automated serial analysis approach or imaging format. However, the detection limits of affordable designs are poor, and the technique is not generally amenable to point-of-care settings.

1.4.1 Ellipsometry

Ellipsometry uses the changes in the polarization of light as it is reflected from a target surface to measure the substrate's dielectric properties and thickness. Polarized light is reflected off the substrate surface and the polarization shift can be correlated to changes in the refractive index of the substrate. This method can achieve detection limits ranging from nM to pM in antigen binding assays, providing good sensor performance at relatively low cost.[39] The drawback to this approach is that it suffers from poor multiplexing capability and is challenging to integrate into a point-of-care setting.

1.4.2 Interferometry

Interferometric biosensors rely on the change in optical phase velocity resulting from biomolecule accumulation on a sensing strip coated with a recognition moiety. For an example, Schmitt et al utilized a singular beam that was split and coupled into waveguides representing a sensing path and reference path.[46] These two paths were subsequently recombined, and the resulting interference was used to measure the degree of analyte binding in the sensing path. Techniques based on interferometry are very sensitive and exhibit detection limits in the femtomolar range.[40] In addition, the

method is relatively cheap and has the capability of being applied in a point of care setting. Unfortunately, though, it suffers from poor multiplexing capabilities and has low throughput, limiting its usefulness for potential ovarian cancer screens.

1.4.3 Microcantilever Resonance Methods

Some interesting methods involving microcantilevers as balances have been explored as label-free biosensors. A small cantilever functionalized with a biorecognition element is oscillated at its natural resonance frequency in a sample solution. The attachment of its target antigen causes a shift in the cantilever resonance frequency, which can be correlated to analyte concentration. This method offers detection limits in the ng/mL range and has relatively good throughput, however the method is not user friendly and would be difficult to implement in a clinical lab setting.[41] In addition, the instrumentation is somewhat expensive, and the approach is prone to artifacts that limit its robustness as a potential screen.

1.4.4 Mass Spectrometry

Mass spectrometry is used to measure the mass-to-charge ratio of charged materials and has proven to be extremely important in the discovery of protein biomarkers in numerous diseases.[43] While effective in biomarker identification, mass spectrometry is better suited for qualitative purposes and has some difficulty when attempting to quantify targets. In addition, it is highly cost-prohibitive and is not suitable for the point-of-care environment.

1.4.5 Optical Resonator Sensors

One very promising approach for label-free sensing exploits tiny microstructures that take advantage of a phenomenon referred to as whispering gallery mode (WGM) resonances. These methods are based on the ability of circular dielectrics to store light through continuous total internal reflection.[44] The wavelength that is supported within each structure is dependent on the surrounding refractive index (RI) and changes in the RI shifts the resonant wavelength that is supported within the

cavity.[47] This phenomenon can be exploited as a sensing mechanism by immobilizing capture materials on the sensor surface. Binding events at the sensor surface will change the local RI and shift the resonant wavelength which can be used to quantify analyte binding.[44, 48] These techniques demonstrated excellent detection limits and are becoming increasingly popular for biomarker detection. In addition, their small size and relatively low cost make them ideal for point-of-care settings. The goals of the research discussed here, therefore, are to combine the favorable metrics from several resonator designs to create a multiplexed assay amenable for routine ovarian cancer screens. Before discussing their use in further detail, it is informative to first discuss the concept of total internal reflection, or TIR.

1.5 Total Internal Reflection and the Evanescent Wave

Consider an incident beam of light passing from a medium of high refractive index to a medium of lower refractive index. Snell's law for light incident on the interface states that:

$$n_1 sin\theta_1 = n_2 sin\theta_2 \qquad \text{Eq. 1.4}$$

Where n_1 and n_2 are the refractive indices of the first and second medium, respectively, and θ_1 and θ_2 are the incident and refracted angles of the light beam measured from the interface normal. As light passes from a high index to a low index material, Snell's Law states that the refracted light waves will be bent at greater angles from the surface normal as the incident angle increases. This is shown schematically in Figure 1.5. The point at which $\theta_2 = 90°$, results in all the light being reflected back into medium n_2 and is referred to as the critical angle, θ_c:

$$\theta_c = sin^{-1}\left(\frac{n_2}{n_1}\right) \qquad \text{Eq. 1.5}$$

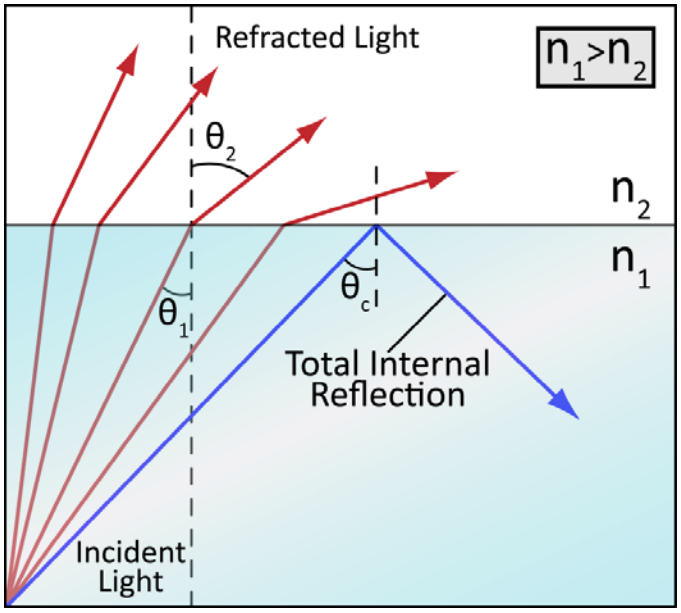

Figure 1.3: Light refraction and total internal reflection at the critical angle.

Reaching and surpassing this incident angle results in a situation where light is no longer refracted into the less optically dense medium but is completely reflected into the medium of incidence. This special condition is referred to as total internal reflection (TIR) and is illustrated by Figure 1.3. Even though all of the light is reflected at the interface under TIR, there exist a non-propagating, exponentially decaying evanescent wave which extends into the second medium. This is illustrated in Fig. 1.4. This non-propagating field extending into the second medium can excite molecules located near the interface. This phenomenon has been exploited extensively in fluorescence microscopy for surface sensitive measurements.

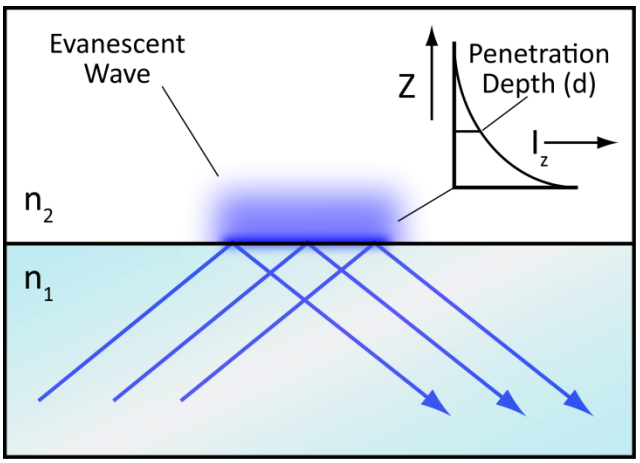

Figure 1.4: Exponential intensity decay of an evanescent wave.[49]

The intensity of this field is described by:[49]

$$I_Z = I_0 e^{-z/d} \quad \text{Eq. 1.6}$$

Where I_z is the intensity of the field at distance z (perpendicular to the interface), I_0 is the intensity of the field at the interface, and d is the penetration depth of the field, given by:[49]

$$d = \frac{\lambda}{\sqrt{4\pi\left(n_1^2 sin^2\theta_i - n_2^2\right)}} \quad \text{Eq. 1.7}$$

where n_1 and n_2 is the refractive index of medium 1 and medium 2 in Fig. 1.3, respectively. The depth is dependent on the incident wavelength, the refractive indices of the two materials, and the incident angle of the wave. Generally, the penetration depth ranges from approximately 50-500nm for visible light.[49]

These are both useful phenomena – TIR is commonly exploited in both scientific and commercial applications, and the evanescent wave has uses in research-based applications. Total internal reflection is the underlying principle which allows light to be guided long distances through fiber optics in telecommunications, and the evanescent field has been extensively employed as a noise-reduction technique in microscopy. The work in this dissertation will be centered on exploiting both TIR and the evanescent field for bioanalytical applications ranging from biosensing to fundamental molecular studies.

1.6 The Whispering Gallery Mode

As mentioned in Section 1.4.5, WGM resonators take advantage of continuous total internal reflection to confine light within their structures.[44, 50-53] The term whispering gallery was first used by Lord Rayleigh in 1878 to describe an acoustical phenomenon observed in St. Paul's Cathedral in London. Sound waves from whispers directed at one side of the dome would carry to the opposite side of the gallery, leading Rayleigh to suggest they were confined to the boundary of the dome. A similar phenomenon can be observed in the continuous confinement of light within circular dielectrics.

Although the existence of this phenomenon has been known for many years, only recently has their usefulness and applicability in sensing started to emerge.[44, 50]

Figure 1.5 schematically illustrates the optical whispering gallery mode. Light incident upon an interface undergoes total internal reflection. If a dielectric sphere is brought near this boundary, light is coupled into the structure through interaction with the evanescent wave at the substrate surface. If the

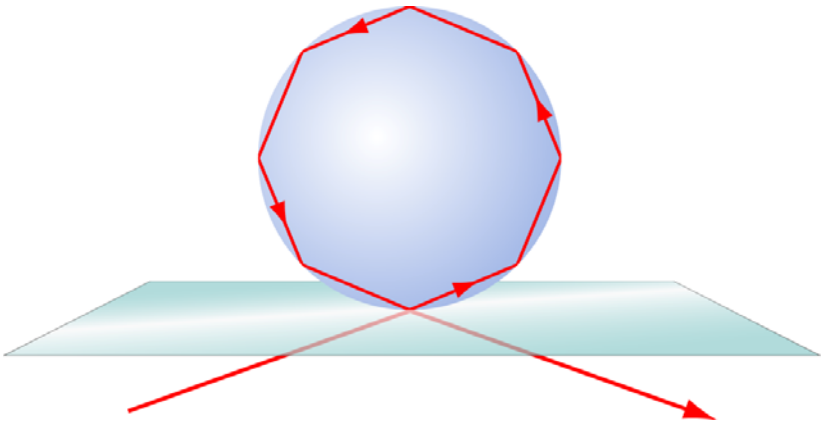

Figure 1.5: Ray tracing schematic of a whispering gallery mode.

sphere has a refractive index greater than its surroundings, light coupled into the structure undergoes total internal reflection at each interaction with the sphere surface as illustrated in Fig. 1.5. When the roundtrip distance of the light within the sphere is an integer multiple of the coupled wavelength, the light coherently drives itself by returning in phase which leads to constructive interference.[44, 52, 54, 55] On resonance, this constructive interference results in a build-up of light intensity within the sphere. This resonant condition is termed an optical whispering gallery mode, in tribute to the phrase coined over a century ago. This phenomenon is quite useful for sensors and other applications and is at the epicenter of a rapidly emerging field of study.[44, 50, 52, 56]

For each resonator, there are specific wavelengths which may be efficiently trapped within the cavity under certain conditions. These resonant wavelengths lead to enhanced light storage within the resonator, and arise when the following equation is satisfied.[44, 47, 57]

$$\lambda_r = \frac{2\pi r n_{eff}}{m} \qquad \text{Eq. 1.8}$$

In Eq. 1.8, λ_r is the resonant wavelength, r is the radius of the cavity, n_{eff} is the effective refractive index surrounding the sphere, and m is an integer multiple of the wavelength. For sensing applications, the important value to consider in this equation is n_{eff}, as it takes into account the refractive index of the optical resonator as well as its surroundings. Any changes in this value due to an alteration of the cavity's surrounding refractive index will result in an alteration of λ_r. By measuring changes in the resonant wavelength, therefore, WGMs may be exploited for sensing methods which rely on refractive index changes.

For biosensing applications, recognition elements may be bound to the resonator surface, and subsequent analyte binding will change n_{eff} and shift the resonant wavelength.[44, 48] The shift in WGM resonance, therefore, can be used to track and quantify analyte binding without the use of labels. Further, since light confined in the WGM at resonance undergoes multiple revolutions within the cavity, the effective light-sample interaction length is significant, leading to low limits of detection.[57]

There are a number of challenges associated with WGM sensor development, such as expanding their use to multiplexed analyte detection and making them amenable for point-of-care screening. The common implementations of WGM techniques, their advantages and drawbacks, as well as our progress in developing and improving a new approach to WGM sensing for biomarker measurement will be discussed in the chapters to come.

1.8 Motivation and Overview of Dissertation

While much research is devoted to the identification and detection of ovarian cancer biomarkers, no screening method is currently available for early detection of the disease.[6] This is due to the asymptomatic nature of the disease in its early stages, necessitating an accurate assay that can be routinely performed on the female population. The research performed in this dissertation is motivated with the goal of developing a flexible, sensitive platform that can be used for multiplexed biomarker

detection. While our intent revolves around ovarian cancer screens, the techniques developed here are general and will be widely amenable to other sensing applications.

In Chapter 2, the fundamental properties of WGMs are discussed and how the resonant condition can be exploited for biosensing purposes.[58] Common approaches used for WGM biosensing are introduced along with a discussion of their merits and disadvantages in biosensor applications.[59-62] In an attempt to combine the favorable attributes of these techniques, we introduce a new approach for biosensing which combines microsphere WGM resonators with fluorescence imaging. We show that the multiplexing capability is vastly increased using this imaging approach, enabling the detection of multiple targets in a single assay. The feasibility of using this method for biomarker measurement is demonstrated by detecting two biomarkers linked to ovarian cancer pathogenesis.

Chapter 3 introduces a simplified method for launching WGMs into labeled microspheres by employing a Dove prism; this approach enables much larger fields of spheres to be excited and imaged. To advance the WGM imaging technique toward clinical use, we also show that non-specific binding is not limiting by detecting CA-125 doped into serum samples. The eventual clinical utility of this approach is illustrated by measuring CA-125 levels in serum collected from a healthy donor and a patient diagnosed with ovarian cancer. In addition, through changes to the instrumentation, the increase in signal to noise has revealed that the mode structure within each microsphere cavity can be imaged using this approach, providing exciting new opportunities for measuring analyte binding. Finite element analysis is introduced to assist in exploring resonator geometries and conditions which lead to changes in the fundamental mode structure observed with analyte binding.[63, 64]

Although whispering gallery detection is effective in biomarker measurement, in practice the sensing region covers a very small area. As in all label-free assays, non-specific binding can be an issue for WGM detection and it is highly desirable that all immobilized antibodies be active. It is

crucial, therefore, that all capture antibodies are immobilized in the appropriate orientation for efficient binding of target analytes.[65-67] Chapter 4 discusses current techniques employed for antibody immobilization, as well as common methods used for measuring the resulting antibody activity.[65-73] Since binding strongly depends on antibody orientations on the surface, we discuss the challenges associated with measuring these orientations. Current techniques involve indirect measurements or are performed using ensemble averaged methods, which reduces site-specific information. To maximize sensor performance, therefore, new techniques capable of characterizing antibody orientation at the single molecule level are required. Chapter 4 discusses our work to employ an emerging fluorescence technique to characterize the three-dimensional orientation of single molecules. To test and validate this method, we present studies on well-characterized test systems, using model lipid membranes. This groundwork will allow for the eventual use of single-molecule orientation measurements to probe antibody orientation as a function of immobilization chemistry, thus maximizing the potential of antibody-based sensors.

Previous studies have shown that polarized total internal reflection fluorescence microscopy (PTIRF-M) is capable of directly determining the three-dimensional orientation of single molecules.[74-78] We exploit this approach in Chapter 5, and extract the orientation of single molecule reporter probes to examine the structural characteristics of DPPC model membrane films at the molecular level.[79] We then utilize this technique to find the characteristic "equivalent surface pressure" between lipid monolayers formed by Langmuir-Blodgett deposition and supported lipid bilayers formed by vesicle fusion. The single molecule approach is further explored by comparing the condensing effects of sterol additives in each system. This method is therefore capable of measuring heterogeneous properties of supported films at the molecular level, and is an appealing compliment to bulk measurements of membrane properties.

Our single-molecule studies to this point are employed on static systems in a dry atmosphere. As future single-molecule work will be used to determine antibody orientations in a dynamic, fluid environment, it is important to explore the time-resolved capabilities of this approach. In Chapter 6 we explore the effects of hydration on model membrane structure using single-molecule orientations.[80] We show that by increasing the hydration levels of model membrane systems, both structural and dynamic changes occur within the membrane at the molecular level. We also observe that this technique is capable of measuring three-dimensional orientational changes in real time. Future goals include employing this method to probe antibody orientations on substrates in situ, so these studies are an important step for understanding how the technique may be applied in fluidic systems.

Having tested and validated the single-molecule orientation approach, Chapter 7 introduces our initial research directed at examining antibody orientations. The antibody 4-4-20 and its binding properties to the fluorescent probe Fluo-3 are discussed which will serve as the model system.[81, 82] Initial studies suggest that the Fluo-3 fluorophore is sufficiently fluorescent for single-molecule studies, making it feasible for measuring its orientation while present in its corresponding antibody complex. In the context of WGM sensor development, additional studies towards improving sensor performance are presented, including the optimization of dye loading increase resonator Q-factor. An approach to reduce the whispering gallery mode volume is also discussed as a potential improvement on WGM sensitivity to protein binding.

References

1. Chambers, A. F.; Vanderhyden, B. C., *Clin. Cancer. Res.* **2006,** *12* (2), 323-327.
2. Yap, T. A.; Carden, C. P.; Kaye, S. B., *Nat. Rev. Cancer* **2009,** *9* (3), 167-81.
3. Badgwell, D.; Bast, R. C., *Dis. Markers* **2007,** *23* (5-6), 397-410.
4. Nossov, V.; Amneus, M.; Su, F.; Lang, J.; Janco, J. M.; Reddy, S. T.; Farias-Eisner, R., *Am. J. Obstet. Gynecol.* **2008,** *199* (3), 215-23.
5. Karlan, B. Y.; McIntosh, M., *J. Clin. Oncol.* **2007,** *25* (11), 1303-4.
6. Balch, C.; Fang, F.; Matei, D. E.; Huang, T. H. M.; Nephew, K. P., *Endocrinology* **2009,** *150* (9), 4003-4011.
7. Twickler, D. M.; Moschos, E., *Am. J. Roentgenol.* **2010,** *194* (2), 322-329.
8. Ng, A.; Swanevelder, J., *CEACCP* **2011,** *11* (5), 186-192.
9. Gupta, D.; Lis, C. G., *J. Ovarian Res.* **2009,** *2*, 13.
10. Moore, R. G.; McMeekin, D. S.; Brown, A. K.; DiSilvestro, P.; Miller, M. C.; Allard, W. J.; Gajewski, W.; Kurman, R.; Bast, R. C.; Skates, S. J., *Gynecol. Oncol.* **2009,** *112* (1), 40-46.
11. Bast, R. C., Jr., *J. Clin. Oncol.* **2003,** *21* (10 Suppl), 200s-205s.
12. Hermsen, B. B.; von Mensdorff-Pouilly, S.; Berkhof, J.; van Diest, P. J.; Gille, J. J.; Menko, F. H.; Blankenstein, M. A.; Kenemans, P.; Verheijen, R. H., *J. Clin. Oncol.* **2007,** *25* (11), 1383-9.
13. Moore, R. G.; Brown, A. K.; Miller, M. C.; Skates, S.; Allard, W. J.; Verch, T.; Steinhoff, M.; Messerlian, G.; DiSilvestro, P.; Granai, C. O.; Bast, R. C., *Gynecol. Oncol.* **2008,** *108* (2), 402-408.
14. Sok, D.; Clarizia, L. J.; Farris, L. R.; McDonald, M. J., *Anal. Bioanal. Chem.* **2009,** *393* (5), 1521-3.
15. Tian, C.; Markman, M.; Zaino, R.; Ozols, R. F.; McGuire, W. P.; Muggia, F. M.; Rose, P. G.; Spriggs, D.; Armstrong, D. K., *Cancer* **2009,** *115* (7), 1395-403.
16. Saksela, E., *Int. J. Gynecol. Pathol.* **1993,** *12* (2), 156-161.
17. Farghaly, S. A., *Gynecol. Obstet. Inves.* **1992,** *34* (2), 65-72.
18. Welander, C., *Acta Obstet. Gynecol. Scand. Sup.* **1992,** *155*, 85-93.
19. Cancer Antigen CA125 ELISA Test Kit User Manual. Panomics: 2007.
20. Hellstrom, I.; Raycraft, J.; Hayden-Ledbetter, M.; Ledbetter, J. A.; Schummer, M.; McIntosh, M.; Drescher, C.; Urban, N.; Hellstrom, K. E., *Cancer Res.* **2003,** *63* (13), 3695-3700.
21. Visintin, I.; Feng, Z.; Longton, G.; Ward, D. C.; Alvero, A. B.; Lai, Y.; Tenthorey, J.; Leiser, A.; Flores-Saaib, R.; Yu, H.; Azori, M.; Rutherford, T.; Schwart, P. E.; Mor, G., *Clin. Cancer. Res.* **2008,** *14* (21), 7158-7158.
22. Nishida, Y.; Kohno, K.; Kawamata, T.; Morimitsu, K.; Kuwano, M.; Miyakawa, I., *Gynecol. Oncol.* **1995,** *56* (3), 357-361.
23. Woolas, R. P.; Conaway, M. R.; Xu, F.; Jacobs, I. J.; Yu, Y.; Daly, L.; Davies, A. P.; O'Briant, K.; Berchuck, A.; Soper, J. T.; Clarke-Pearson, D. L.; Rodriguez, G.; Oram, D. H.; Bast, R. C., *Gynecol. Oncol.* **1995,** *59* (1), 111-116.
24. Hausler, S. F. M.; Keller, A.; Chandran, P. A.; Ziegler, K.; Zipp, K.; Heuer, S.; Krockenberger, M.; Engel, J. B.; Honig, A.; Scheffler, M.; Dietl, J.; Wischhusen, J., *Brit. J. Cancer.* **2010,** *103* (5), 693-700.
25. Hui, A.; How, C.; Ito, E.; Liu, F. F., *Bmc Cancer* **2011,** *11*.
26. Altman, D. G.; Bland, J. M., *Brit. Med. J.* **1994,** *308* (6943), 1552-1552.
27. Altman, D. G.; Bland, J. M., *Brit. Med. J.* **1994,** *309* (6947), 102-102.
28. Zhang, B.; Cai, F. F.; Zhong, X. Y., *Eur. J. Obstet. Gyn. R. B.* **2011,** *158* (2), 119-123.
29. Dutta, S.; Wang, F. Q.; Phalen, A.; Fishman, D. A., *Cancer Biol. Ther.* **2010,** *9* (9), 668-677.
30. Wild, D., *The Immunoassay Handbook*. Elsevier Ltd.: 2005.
31. Marquez, L. A.; Dunford, H. B., *Biochemistry-Us* **1997,** *36* (31), 9349-9355.

32. Dahiya, N.; Sherman-Baust, C. A.; Wang, T. L.; Davidson, B.; Shih, I. M.; Zhang, Y. Q.; Wood, W.; Becker, K. G.; Morin, P. J., *Plos One* **2008,** *3* (6).
33. Iorio, M. V.; Visone, R.; Di Leva, G.; Donati, V.; Petrocca, F.; Casalini, P.; Taccioli, C.; Volinia, S.; Liu, C. G.; Alder, H.; Calin, G. A.; Menard, S.; Croce, C. M., *Cancer Res.* **2007,** *67* (18), 8699-8707.
34. Taylor, D. D.; Gercel-Taylor, C., *Gynecol. Oncol.* **2008,** *110* (1), 13-21.
35. Hayashi, Y.; Matsuda, R.; Maitani, T.; Imai, K.; Nishimura, W.; Ito, K.; Maeda, M., *Anal. Chem.* **2004,** *76* (5), 1295-1301.
36. Jacobs, I. J.; Menon, U., *Mol. Cell. Proteomics* **2004,** *3* (4), 355-366.
37. Dobrzycka, B.; Terlikowski, S. J.; Kowalczuk, O.; Kinalski, M., *Eur Cytokine Netw.* **2009,** *20* (3), 131-134.
38. Hiep, H. M.; Endo, T.; Kerman, K.; Chikae, M.; Kim, D. K.; Yamamura, S.; Takamura, Y.; Tamiya, E., *Sci. Technol. Adv. Mat.* **2007,** *8* (4), 331-338.
39. Qi, C.; Zhu, W.; Niu, Y.; Zhang, H. G.; Zhu, G. Y.; Meng, Y. H.; Chen, S.; Jin, G., *J. Viral Hepatitis* **2009,** *16* (11), 822-832.
40. Ozkumur, E.; Needham, J. W.; Bergstein, D. A.; Gonzalez, R.; Cabodi, M.; Gershoni, J. M.; Goldberg, B. B.; Unlu, M. S., *P. Natl. Acad. Sci. USA* **2008,** *105* (23), 7988-7992.
41. Wu, G. H.; Datar, R. H.; Hansen, K. M.; Thundat, T.; Cote, R. J.; Majumdar, A., *Nat. Biotechnol.* **2001,** *19* (9), 856-860.
42. Carr, S. A.; Anderson, L., *Clin. Chem.* **2008,** *54* (11), 1749-1752.
43. Diamandis, E. P., *Mol. Cell. Proteomics* **2004,** *3* (4), 367-378.
44. Vollmer, F.; Arnold, S., *Nat. Methods* **2008,** *5* (7), 591-596.
45. Biacore, *Technical Note 1 - Surface Plasmon Resonance.* [Online] http://www.proteomics.iastate.edu/seminars/BIACore/TechnologyNotes/TechnologyNote1.pdf (accessed Mar 1, 2012).
46. Schmitt, K.; Schirmer, B.; Hoffmann, C.; Brandenburg, A.; Meyrueis, P., *Biosens. Bioelectron.* **2007,** *22* (11), 2591-2597.
47. Hanumegowda, N. M.; Stica, C. J.; Patel, B. C.; White, I.; Fan, X., *Appl. Phys. Lett.* **2005,** *87* (20), 201107.
48. Fan, X. D.; White, I. M.; Shopoua, S. I.; Zhu, H. Y.; Suter, J. D.; Sun, Y. Z., *Anal. Chim. Acta.* **2008,** *620* (1-2), 8-26.
49. Olympus Microscopy Primer. http://www.olympusmicro.com/primer/ (accessed Mar 2, 2012).
50. Vahala, K. J., *Nature* **2003,** *424* (6950), 839-846.
51. Oraevsky, A. N., *Quantum Electron+* **2002,** *32* (5), 377-400.
52. Chiasera, A.; Dumeige, Y.; Feron, P.; Ferrari, M.; Jestin, Y.; Conti, G. N.; Pelli, S.; Soria, S.; Righini, G. C., *Laser Photonics Rev.* **2010,** *4* (3), 457-482.
53. Soria, S.; Berneschi, S.; Brenci, M.; Cosi, F.; Conti, G. N.; Pelli, S.; Righini, G. C., *Sensors* **2011,** *11* (1), 785-805.
54. Matsko, A. B.; Ilchenko, V. S., *IEEE J. Sel. Top. Quant.* **2006,** *12* (1), 3-14.
55. Quan, H.; Guo, Z., *J Micro-Nanolith. Mem.* **2009,** *8* (3), 033060-7.
56. Ilchenko, V. S.; Matsko, A. B., *IEEE J. Sel. Top. Quant.* **2006,** *12* (1), 15-32.
57. Fan, X.; White, I. M.; Zhu, H.; Suter, J. D.; Oveys, H. In *Overview of novel integrated optical ring resonator bio/chemical sensors*, San Jose, CA, USA, Kudryashov, A. V.; Paxton, A. H.; Ilchenko, V. S., Eds. SPIE: San Jose, CA, USA, 2007; pp 64520M-20.
58. Huckabay, H. A.; Dunn, R. C., *Sensor. Actuat. B-Chem.* **2011,** *160* (1), 1262-1267.
59. Knight, J. C.; Cheung, G.; Jacques, F.; Birks, T. A., *Opt. Lett.* **1997,** *22* (15), 1129-1131.
60. Vollmer, F.; Braun, D.; Libchaber, A.; Khoshsima, M.; Teraoka, I.; Arnold, S., *Appl. Phys. Lett.* **2002,** *80* (21), 4057-4059.

61. Yalcin, A.; Popat, K. C.; Aldridge, J. C.; Desai, T. A.; Hryniewicz, J.; Chbouki, N.; Little, B. E.; Oliver, K.; Van, V.; Sai, C.; Gill, D.; Anthes-Washburn, M.; Unlu, M. S.; Goldberg, B. B., *IEEE J. Sel. Top. Quant.* **2006,** *12* (1), 148-155.
62. Washburn, A. L.; Gunn, L. C.; Bailey, R. C., *Anal. Chem.* **2009,** *81* (22), 9499-9506.
63. Cheema, M. I.; Kirk, A. G. In *COMSOL Conference*, Boston, **2010**.
64. Oxborrow, M., *IEEE T. Microw. Theory.* **2007,** *55* (6), 1209-1218.
65. Seurynck-Servoss, S. L.; Baird, C. L.; Rodland, K. D.; Zangar, R. C., *Front. Biosci.* **2007,** *12*, 3956-3964.
66. Jung, Y.; Jeong, J. Y.; Chung, B. H., *Analyst* **2008,** *133* (6), 697-701.
67. Bae, Y. M.; Oh, B.-K.; Lee, W.; Lee, W. H.; Choi, J.-W., *Biosens. Bioelectron.* **2005,** *21* (1), 103-110.
68. Wang, H.; Castner, D. G.; Ratner, B. D.; Jiang, S. Y., *Langmuir* **2004,** *20* (5), 1877-1887.
69. Xu, H.; Zhao, X. B.; Grant, C.; Lu, J. R.; Williams, D. E.; Penfold, J., *Langmuir* **2006,** *22* (14), 6313-6320.
70. Caruso, F.; Rodda, E.; Furlong, D. N., *J. Colloid. Interf. Sci.* **1996,** *178* (1), 104-115.
71. Kausaite-Minkstimiene, A.; Ramanaviciene, A.; Kirlyte, J.; Ramanavicius, A., *Anal. Chem.* **2010,** *82* (15), 6401-6408.
72. Pei, Z. C.; Anderson, H.; Myrskog, A.; Duner, G.; Ingemarsson, B.; Aastrup, T., *Anal. Biochem.* **2010,** *398* (2), 161-168.
73. San Paulo, A.; Garcia, R., *Biophys. J.* **2000,** *78* (3), 1599-1605.
74. Bartko, A. P.; Dickson, R. M., *J. Phys. Chem. B* **1999,** *103* (51), 11237-11241.
75. Bartko, A. P.; Dickson, R. M., *J. Phys. Chem. B* **1999,** *103* (16), 3053-3056.
76. Forkey, J. N.; Quinlan, M. E.; Goldman, Y. E., *Biophys. J.* **2005,** *89* (2), 1261-1271.
77. Patra, D.; Gregor, I.; Enderlein, J., *J. Phys. Chem. A* **2004,** *108* (33), 6836-6841.
78. Toprak, E.; Enderlein, J.; Syed, S.; McKinney, S. A.; Petschek, R. G.; Ha, T.; Goldman, Y. E.; Selvin, P. R., *P. Natl. Acad. Sci. USA* **2006,** *103* (17), 6495-6499.
79. Livanec, P. W.; Huckabay, H. A.; Dunn, R. C., *J. Phys. Chem. B* **2009,** *113* (30), 10240-10248.
80. Huckabay, H. A.; Dunn, R. C., *Langmuir* **2011,** *27* (6), 2658-2666.
81. Herron, J. N.; He, X. M.; Mason, M. L.; Voss, E. W., Jr.; Edmundson, A. B., *Proteins: Struct., Funct., Genet.* **1989,** *5*, 271-80.
82. Whitlow, M.; Howard, A. J.; Wood, J. F.; Voss, E. W., Jr.; Hardman, K. D., *Protein Eng.* **1995,** *8*, 749-61.

Chapter 2: Employing a Fluorescence-Based Approach to Whispering Gallery Mode Imaging

2.1 The Whispering Gallery Resonator

Whispering gallery mode resonances arise when light is efficiently coupled into and stored within circular dielectric cavities. A number of different geometries are currently employed to achieve WGM excitation and detection, each possessing its own merits and disadvantages. Before discussing these various techniques, let us first consider the uses of these structures as sensing platforms, and how their performance is measured.

2.1.1 Employing Whispering Gallery Resonators for Biomarker Detection

The resonant condition of a WGM structure can be expressed by:[1-3]

$$\lambda_r = \frac{2\pi r n_{eff}}{m} \qquad \text{Equation 2.1}$$

where λ_r is the resonant wavelength, r is the radius of the structure, m is an integer multiple of the wavelength, and n_{eff} is the effective refractive index, which takes into account the refractive indices of both the resonator and its surroundings. If a biological recognition element, such as an antibody, is bound to the resonator surface, binding of the target antigen changes n_{eff} in Eq. 2.1 and results in a shift of the resonant condition,[4, 5] as illustrated in Figure 2.1. The magnitude of the shift is given by

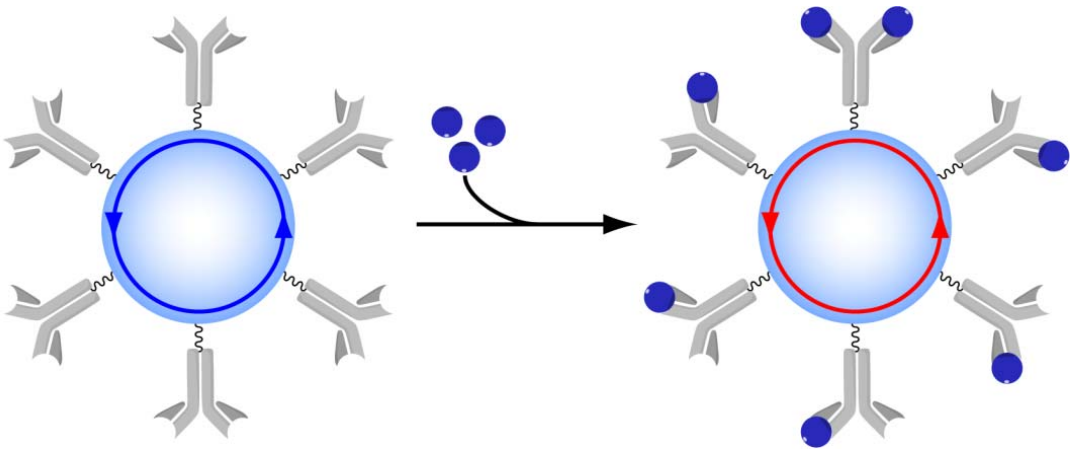

Figure 2.1: Resonant wavelength changes due to antigen binding.

Equation 2.2:[6, 7]

$$\frac{\Delta\lambda_r}{\lambda_r} = \frac{\alpha_{ex}\sigma_p}{\epsilon_0(n_s^2 - n_m^2)r} \quad \text{Equation 2.2}$$

where n_s and n_m are the refractive indices of the sphere and the surrounding medium, respectively. α_{ex} is the excess polarizability, σ_p is the surface coverage of the target biomarker, ϵ_0 is the vacuum permittivity, and r is the radius of the sphere. The dependence of the resonant wavelength on the surrounding refractive index is the central property that is exploited in WGM-based general sensing platforms. An important attribute of the sensor performance is how efficiently they trap light within the resonator. A number of independent factors affect this efficiency, and their collective contributions comprise a term referred to as the quality factor (Q-factor). The magnitude of the Q-factor is related to the overall performance metrics of a WGM resonator.

2.1.2 Resonator Q-factors and Their Impact on Detection Capabilities

The quality of a resonator is qualified by the Q-factor and is related to the efficiency of the cavity to confine light through continuous total internal reflections. It is empirically defined as:

$$Q = \frac{\lambda_r}{\delta\lambda_r} \quad \text{Equation 2.3}$$

where λ_r is the resonant wavelength, and $\delta\lambda_r$ is the full width at half maximum of the resonant wavelength intensity.

High Q resonators have very low light attenuation, and light trapped within these structures undergo multiple revolutions within the cavity. For sensing applications, high Q resonators result in increased light-sample interaction and improved sensor performance. It is therefore advantageous to strive for the highest possible Q-factor when designing WGM resonators. If we consider a sphere undergoing WGM excitation, the inherent Q factor of the structure has four independent contributions:[1, 8]

$$Q^{-1} = Q_{rad}^{-1} + Q_{mat}^{-1} + Q_{s.s.}^{-1} + Q_{cont}^{-1} \quad \text{Equation 2.4}$$

where Q_{rad}^{-1} characterizes the radiative losses associated with bending losses within the spherical cavity.[1, 8] These losses increase exponentially as sphere size decreases. For spheres with diameters ≥ 15λ, these losses essentially vanish. Q_{mat}^{-1} accounts for light attenuation due to material absorption of the circulating wave by the resonator structure. The Q-factor limitation due to Q_{mat} can be approximated by:[1, 8]

$$Q_{mat} = \frac{2\pi n}{\alpha\lambda} \qquad \text{Equation 2.5}$$

Where n is the refractive index, α is the material attenuation and λ is the wavelength. As an example, using fused silica and a wavelength of 633 nm, the Q factor is limited by Q_{mat} to approximately $9\ x\ 10^9$.

The major limiting factor for spheres ranging from ~40-80 μm in diameter is $Q_{s.s.}^{-1}$, which accounts for surface scattering losses on the sphere due to imperfections.[1, 8] Using reasonable values for scratch-dig inhomogeneities in fused silica, the fundamental Q-factor limit due to $Q_{s.s.}$ ranges from ~3x10^9 to ~6x10^9 for 40-80μm sized spheres.

Q_{cont}^{-1} is based on contributions from surface contaminants present on the sphere surface during fabrication; previous work demonstrated that a time-dependent process involving the adsorption of oxygen followed by atmospheric water on silicon dioxide resonators was the inherent mechanism that limited the Q-factor of fused silica resonators formed via microtorch.[1]

All of the above mechanisms contribute to the intrinsic Q-factor of a WGM resonator. Since the Q-factor characterizes the number of photon revolutions in a cavity, the effective path length, L_{eff}, is given by:[1, 3]

$$L_{eff} = \frac{Q\lambda}{2\pi n} \qquad \text{Equation 2.6}$$

This refers to the effective light-sample interaction length, and sensitivity and detection limits in turn will improve as this quantity is increased. As an example, using a Q-factor of ~4.5x10^9 at a wavelength of 633nm in fused silica, the effective light-sample interaction length is *352 meters*! This immense value illustrates the extraordinary capabilities afforded by using this technique for biomolecule detection.

The Q factor of WGM resonators influences the minimum measurable shift in resonant wavelength due to changes in the surrounding refractive index, and is represented by:[7]

$$(\Delta\lambda_r)_{min} = \frac{\lambda_r * F}{Q} \qquad \text{Equation 2.7}$$

where λ_r is the resonant wavelength and *F* is a "measurement acuity factor" which factors in experimental noise and the spectral bandwidth of the detection system. Finally, the biomolecule surface density detection limit of a WGM resonator is given by:[6, 7]

$$\sigma_{LOD} = \frac{r(n_r^2 - n_m^2)F}{(\alpha_{ex}/\varepsilon_0)Q} \qquad \text{Equation 2.8}$$

where r is the radius of the resonator, α_{ex} is the excess polarizability of the biomolecule, ε_0 is the vacuum permittivity, and n_r and n_m are the refractive indices of the resonator and surrounding medium, respectively. Eq. 2.6 suggests that to achieve the best limits of detection, r*/Q* must be minimized. This is difficult since *Q* is dependent on r, and reducing r will decrease the inherent Q factor due to contributions from Q_{rad}^{-1}. Consequently, the size of spheres used in WGM sensing should be minimized, but not to diameters below ~10μm since radiative losses will degrade the inherent Q factor. Using a sphere with a diameter of 50μm and a Q-factor of 4.5x10^9, the σ_{LOD} for detection of bovine serum albumin is ~1.7 fg/mm^2, several orders of magnitude lower than the best detection limits reported for SPR sensing, at ~1 pg/mm^2.[9] This shows that WGM sensing compares favorably with other label-free techniques used in refractive index and biomolecule detection.[10]

2.1.3 Sensing Approaches Using WGM Resonators

Experimentally, coupling light into WGM resonators is challenging to do efficiently. Exciting resonances in these structures requires using a phase-matched source optically coupled in the near field.[11] Free-space coupling into a WGM structure is very inefficient since the refractive indices of the two mediums are mismatched. Methods used to excite these resonances typically employ an index-matched material undergoing total internal reflection.[2, 7] Bringing a WGM resonator into the near-field

of the resulting evanescent wave causes light to couple into the resonator via frustrated total internal reflection. Several approaches can be used for this excitation, such as prism couplers, waveguides, and tapered fiber optics.[6-8] The similarity between these methods is that they are all based on light tunneling from a pump source into the dielectric resonator. While coupling can be a logistical issue in WGM instrumentation, the technique must also be capable of both exciting these resonances and recording the resulting resonant wavelength as well. Because the spectral linewidth of WGM resonances is exceedingly small ($\delta\lambda$ = 0.14 fm at 633 nm with a Q-factor of 4.5×10^9), tunable lasers used for excitation must have very narrow spectral bandwidths.[7] A variety of methods utilizing different geometries have been employed to meet these requirements.[1, 3, 6-8]

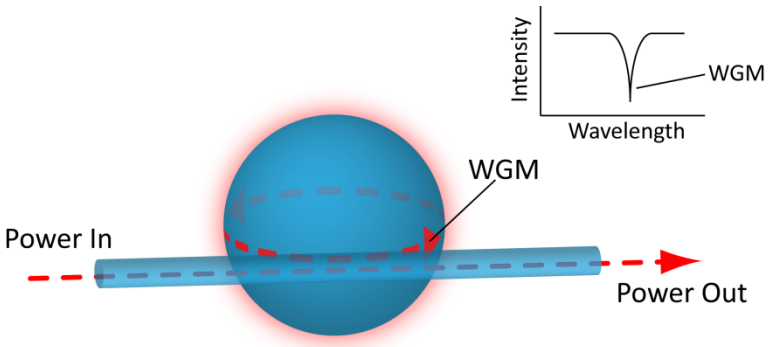

Figure 2.2: Microsphere-based WGM excitation and detection.

A common approach used for WGM detection with microsphere resonators involves a tunable laser launched into an optical fiber with an adiabatically tapered region.[2, 5] Light is coupled into the microsphere resonator using the evanescent field generated from the exposed fiber core at the tapered region. As the laser wavelength is scanned, a dip is observed in the light intensity transmitted through the fiber as the microsphere experiences a WGM resonance, as seen in Fig. 2.2. The dip reflects increased coupling of light from the fiber into the microsphere at the WGM resonance, resulting in a decrease of light transmitted to the distal end of the fiber.

Another commonly employed approach for WGM excitation utilizes high-index planar resonators coupled via on-chip waveguide structures.[12, 13] These resonators are fabricated in clean-room facilities by modern photolithographic techniques. An example of such a resonator is illustrated in Figure 2.3. In this experimental setup, a planar ring resonator and waveguide coupler comprised of

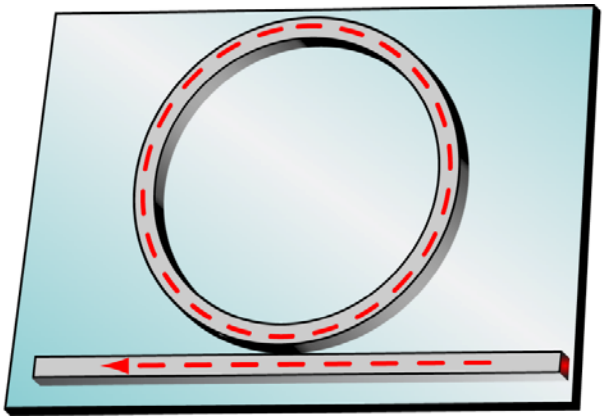

Figure 2.3: Microfabricated, waveguide-coupled planar ring WGM resonator.

fused silica are fabricated using photolithography. In order to excite WGMs of the ring structure, light is free-space coupled into the waveguide either through a grating coupler or by focusing light into the proximal end of the high index structure.[13] The gap between the linear waveguide and the resonator structure is designed to provide sufficient overlap of the evanescent field from light propagating through the waveguide with the ring resonator. As the wavelength of the excitation beam is tuned, WGM resonances in the ring structure are read out as transmission dips at the distal end of the waveguide on the microchip, similar to the approach used in fiber taper coupling.[13]

Of these two approaches for WGM sensing, microspheres exhibit the highest experimental Q-factors due to their fabrication by melting, causing them to surfaces to be extremely smooth and spherical. The greatest Q-factor observed using microspheres thus far is 10^9, as reported by Gorodetsky et al.[1] Microsphere-based methods are simple to employ and have been utilized for the detection of a wide array of materials due to their versatility. Initial work using this approach was reported by Vollmer et al. and involved the detection of streptavidin by microsphere resonators coated with biotinylated

BSA.[5] Saturation of their sensor through streptavidin injections was achieved at concentrations at or below 20 nM. The same group later reported multiplexing capability using this technique through the simultaneous detection of two ssDNA targets using two microspheres separately functionalized with complimentary sequences, showing limits of detection reaching 6 pg/mm^2.[14] Further work in this field by Hanumegowda et al. involved using protein coated microspheres to measure protease activity.[15] The authors stated that by using BSA-coated microspheres, instead of the traditional red-shift associated with analyte binding, blue-shifting of resonant frequencies after trypsin injections was attributed to protein digestion and removal. The limit of detection for trypsin using this approach was projected to be ~0.43 pM.[15] Using aptamer-based capture techniques, Fan's group later demonstrated the detection of thrombin on microsphere resonators, with limits of detection reaching ~23 nM.[16] Studies using this approach also include the measurement of additional oligonucleotides[17], heavy metal ions[18], and bacteria[19]. The major drawbacks to this technique are the logistical issues associated with finding the optimal location along the tapered fiber for optimal sphere coupling, and the mechanical fragility of the fiber taper itself. Moreover, scaling up this approach to detecting numerous targets is extremely difficult. The most amount of multiplexing reported using this method was by measuring two DNA targets;[14] further multiplexing using this technique has yet to be reported. This limitation has garnered interest toward other avenues of WGM excitation and sensing, most notably those formed via microfabrication techniques.

In microfabrication-based WGM sensing, the planar ring structure is chemically modified to incorporate a capture material such as a monoclonal antibody.[13, 20] This approach yields additional multiplexing capability since an array of ring resonators can be fabricated in parallel. By creating optical resonator sensors on a rigid substrate through scalable processes such as photolithography, possibilities are opened up that allow for both automated and multiplexed target detection. Using this approach, Bailey's group has recently reported the multiplexed detection of five cancer biomarkers in complex

media, displaying the efficacy of planar optical resonators for biomarker detection.[20] This method takes an additional step towards the clinical laboratory and since the resonators are fabricated using photolithography, it is amenable to mass producing WGM detection systems.

While this approach offers a number of advantages, it is inherently limited by the fabrication method, reducing the typical Q-factors attainable to several orders of magnitude lower than microsphere-based designs.[3] Secondly, each resonator structure must be individually addressed through its corresponding grating couplers to record any resonant wavelength shifts; this introduces complications when addressing and aligning the excitation and detection system with each resonator. Finally, the chemistry involved with functionalization must be performed post-fabrication, which introduces major complications. In order to perform multiplexed detection with this method, the immobilization chemistry for each antibody must be performed separately for each individual resonator on the chip. This makes the chemistry involved with planar ring resonators a highly rate-limiting step when considering scalability.

2.1.4 Resonator Designs: Advantages and Drawbacks

Shown in Table 2.1 is a summary of the current state of microsphere and microfabricated WGM-based sensor attributes and performance metrics. Unfortunately, there is a tradeoff inherent to each listed approach for WGM detection. As shown in Table 2.1, microsphere sensors exhibit the best limits of detection and are inexpensive. In addition, they are commercially available, come in various sizes and materials, and may be functionalized in batch processing which makes final assay designs flexible and

Table 2.1: Summary of common WGM sensor attributes.[3]

Design Attributes	Microsphere Sensors	Microfabricated Sensors
Q-Factor Limits	$\sim 1 \times 10^{9}$	$\sim 1 \times 10^{5}$
Limits of Detection	$\sim 3 \times 10^{-7}$ RIU	$\sim 2 \times 10^{-5}$ RIU
Multiplexing Capabilities	Very Difficult	Moderate
Fluid Handling	Very Difficult	Good
Throughput	Poor	Moderate
Cost	Excellent	Good

cost effective. To date, however, they have limited multiplexing capabilities and have proven difficult to integrate into fluidic systems.

Microfabricated resonators, on the other hand, are ideal for mass production since their construction is based on scalable photolithography processes. They are amenable to integration with microfluidics systems, so fluid handling is quite effective using these sensors. However the fabrication process inherently limits their maximum attainable Q-factor and range of materials. In addition, all chemistry must be performed on-chip after fabrication, which greatly limits the scalability of the technique.

Our goal for WGM detection is to combine the favorable attributes from both techniques that take advantage of the excellent performance metrics and ease of chemistry associated with microsphere resonators, retains the scalability of microfabricated sensors, and provides an easy approach to multiplexing WGM detection.

2.2 Development of a New WGM Technique by Utilizing Fluorescence Imaging

Here we present a new whispering gallery mode imaging (WGMI) scheme that uses sensitive fluorescence imaging of microsphere resonances to provide multiplexed detection capabilities. The motivation of this research is centered on the development of a sensing technique that is label-free, sensitive, and amenable to highly multiplexed detection. The WGMI approach utilizes an inverted total internal reflection (TIR) microscope to evanescently couple light from a tunable diode laser into a field of microsphere resonators. In the field of WGM sensing, all current designs have limitations with respect to their multiplexing capacity in large part due to the technique in which the WGM spectrum is collected. Instead of employing a single point detector at the distal end of a tapered fiber or waveguide, our goal is to examine the amount of light stored within a microsphere resonator using an imaging technique. As each resonator confines light through multiple total internal reflections within the cavity,

the approach takes advantage of the evanescent field created at the microsphere surface when a WGM resonance is reached. Outside of the sphere, the field decreases exponentially with *r* by:[21]

$$|E| \propto exp[-2\pi(\varepsilon\mu - 1)^{1/2}\frac{r}{\lambda}] \qquad \text{Equation 2.9}$$

where ε is the dielectric constant, μ is the magnetic permeability, and λ is the vacuum wavelength. While not propagating, this field can still excite fluorophores located near the surface of the sphere. By functionalizing the dielectric surface with a fluorescent dye, therefore, increases in sphere fluorescence can be used to detect WGM resonances as shown in Figure 2.4. This simple idea provides a

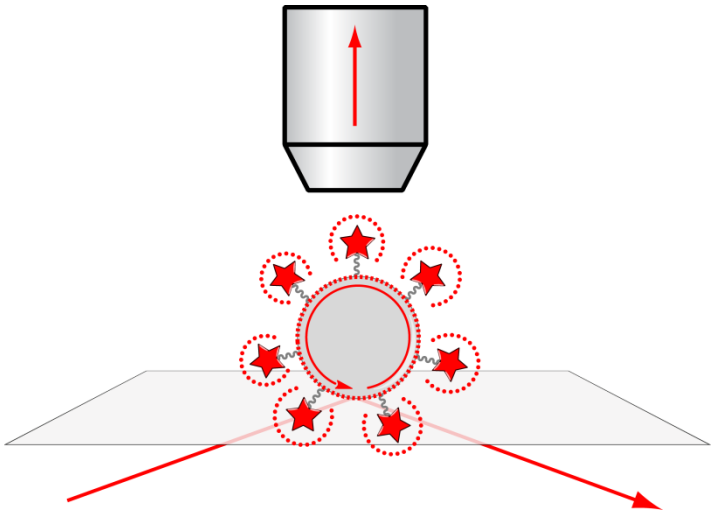

Figure 2.4: WGM measurement using fluorescence readout.

straightforward route for measuring changes in the WGM resonances of large fields of resonators using fluorescence imaging detection. On resonance, a distinctive ring of fluorescence is observed as the WGM excites the surface attached dye. As the wavelength of the tunable diode laser is scanned, therefore, the WGM resonance of each microsphere in the field of view is measured from enhanced fluorescence, which is imaged from above with an upright microscope.

The feasibility of biosensing using this approach is demonstrated by detecting two biomarkers of ovarian cancer - cancer antigen-125 (CA-125) and tumor necrosis factor-alpha (TNF-α).[22-27] Monoclonal antibodies specific for CA-125 and TNF-α were attached to 38 μm and 53 μm glass microspheres,

respectively. Using the relative intensity of the attached fluorescent marker to track changes in the resonant wavelength, linear calibration curves were measured for both antigens. For CA-125, we demonstrate detection limits more than threefold better than commercial ELISA kits. Using this approach, the identity of the detected analyte can be encoded in the sphere size and/or location, providing vastly improved multiplexing capabilities. Moreover, the chemistry associated with attaching antibodies to glass beads is well developed and all immobilization procedures are carried out before the spheres are deposited onto the substrate surface. This approach, therefore, vastly simplifies the chemistry associated with multiplexing over other WGM techniques. It also provides a sensitive and straightforward approach for multiplexed WGM detection that takes advantage of the superior optical properties of microsphere resonators.

2.3 Materials and Methods

2.3.1 Reagents

Soda-lime glass microspheres were obtained from Mo-Sci Corporation (Rolla, MO). Anti-CA-125 mouse monoclonal antibodies (SPM111), 3-aminopropyltriethoxysilane (APTES), glutaraldehyde, bovine serum albumin (BSA), and all solvents were obtained from Fisher Scientific (Hampton, NH). CA-125 antigen was obtained from a commercially available CA-125 screening kit (Panomics BC-1013). Anti-TNF-α antibodies were utilized from a commercial TNF-α screening kit (ESS0001, Fisher Scientific), and TNF-α antigen was purchased from Pierce Biotechnology (Rockford, IL). The amine reactive succinimidyl ester of Alexa Fluor 633 was obtained from Invitrogen Corporation (Carlsbad, CA). CoverWell perfusion chambers were obtained from Grace Bio-Labs (Bend, OR).

2.3.2 Microsphere Preparation

The 38 μm and 53 μm diameter microspheres were separately sonicated in an alconox solution, triply rinsed with 18 MΩ water, and rinsed with absolute ethanol. Each sphere set was placed in a 5%

APTES (v/v) solution in toluene and allowed to tumble overnight. Following amine modification, the spheres were rinsed once in toluene and triply washed in absolute ethanol. Each sphere set was then placed in a 6% glutaraldehyde (v/v) solution in PBS and tumbled for 2 hours. The sphere sets were each triply washed in PBS then placed into corresponding antibody solutions in PBS to tumble for 2 hours: The 38 μm diameter spheres were incubated in 2 μg/mL anti-CA125 solution while 53 μm diameter microspheres where incubated in 2 μg/mL anti-TNF-α. Following incubation, each sphere solution was washed in PBS and labeled with the fluorescent dye, Alexa 633. Finally, each microsphere set was tumbled in a 5% BSA, 5% sucrose (w/v) solution in PBS for 1 hour to block nonspecific adsorption sites.

2.3.3 WGM Measurement

For WGM analysis, spheres were dispersed onto a glass coverslip and placed in a CoverWell perfusion chamber containing PBS. Light was coupled into the spheres using the evanescent wave generated with an inverted total internal reflection fluorescence microscope (TIRF-M) (Olympus IX71, Center Valley, PA) equipped with a 60x objective (1.45 NA achromat, Olympus). The output from an external cavity diode laser (TLB-6904, New Focus, Santa Clara, CA) is offset on the back aperture of the objective to create total internal reflection at the substrate interface. The diode laser can be tuned from 632.86 to 633.12 nm with ≤300kHz linewidth. Fluorescence is collected from above using an Olympus 10x UMPlanFl (0.3 NA) objective lens, filtered (Thorlabs, Newton, New Jersey), and imaged onto a CCD camera (Cascade 650, Roper Scientific, Tuscon, AR). The laser was scanned using LabVIEW (National Instruments, Austin, TX) software and image collection and processing was controlled using Slidebook software (v4.2.0.3, Intelligent Imaging Innovations, Denver, CO).

2.4 Results and Discussion

2.4.1 Experimental Design

Here we report a general approach for combining WGM microsphere resonators with fluorescence imaging to develop a new approach for the multiplexed detection of analytes. The general approach is outlined schematically in Figure 2.5. Light from a tunable diode laser with narrow spectral

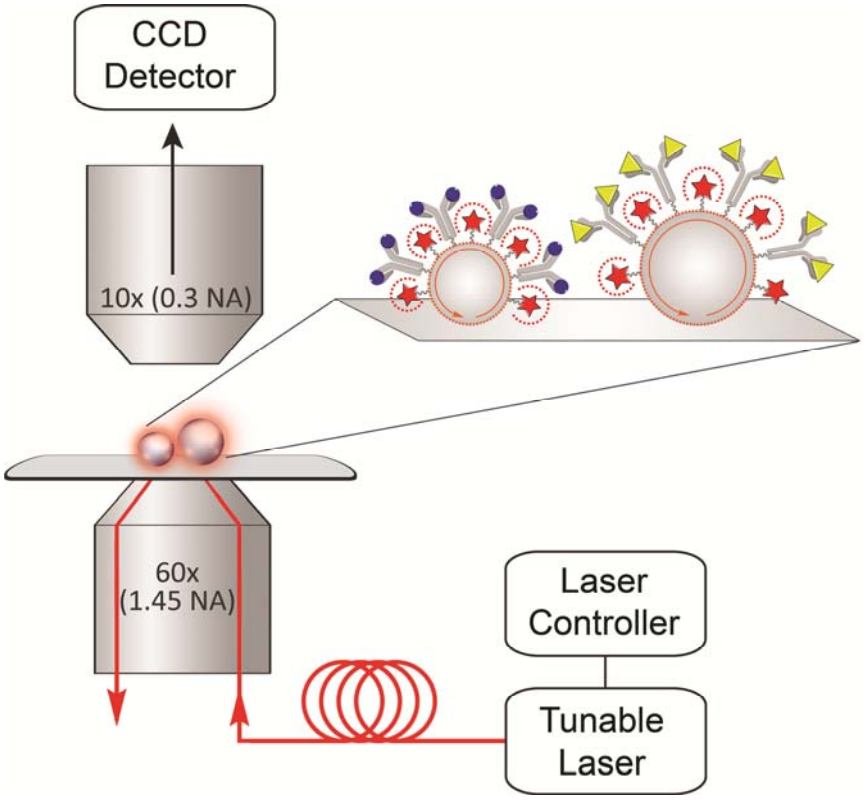

Figure 2.5: Schematic of the apparatus used to couple WGM excitation with fluorescence imaging.

linewidth (≤300kHz) is launched into an optical fiber and coupled into an inverted total internal reflection (TIR) microscope. The TIR microscope uses a high numerical aperture (1.45 NA) objective to couple light to the substrate surface beyond the critical angle, where total internal reflection takes place.[28] The associated evanescent field is used to launch light into the microsphere resonators on the substrate surface as shown schematically in Fig. 2.5.

As the excitation wavelength of the diode laser is scanned, the WGM resonance from each microsphere in the field of view is detected through fluorescence imaging. This is accomplished by

labeling all the microspheres with the same fluorescent dye (stars in Fig. 2.5), which acts as a reporter of the WGM resonance. When a particular microsphere reaches the resonance condition given by Eq. 2.1, a bright ring of enhanced fluorescence is observed as the evanescent field from the WGM resonance excites the surface attached dye. By collecting the fluorescence from above and imaging it onto a CCD camera, the WGM resonance for each sphere in the field of view can be simultaneously measured as the excitation wavelength is scanned.

To illustrate this approach, Figure 2.6 shows a series of fluorescence images taken of the same 38 μm diameter dye labeled soda-lime glass microsphere as the excitation wavelength is scanned.

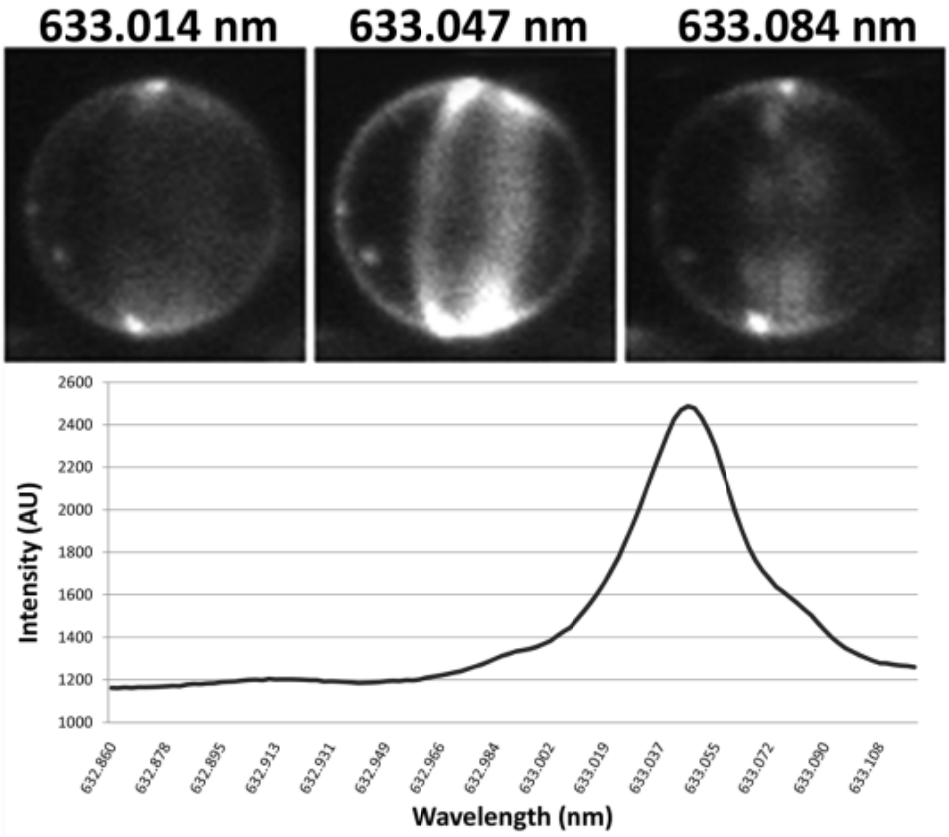

Figure 2.6: (Top) Fluorescence images of a 38 μm diameter microsphere labeled with Alexa 633. (Below) Excitation spectrum of fluorescence intensity with excitation wavelength, extracted from a series of fluorescence images.

When a WGM resonance is reached (center panel) a distinctive ring of enhanced fluorescence is observed as the evanescent field from the circumnavigating light within the resonator excites the surface bound dye. With the current coupling arrangement and dye labeling scheme, we routinely

measure 2- to 4- fold enhancements in the fluorescence intensity at resonance which makes them easily identifiable over the off-resonance background fluorescence. The excitation spectrum in Fig. 2.6 plots the fluorescence intensity from the sphere as the excitation wavelength is scanned. This approach, therefore, uses the fluorescence marker to measure the WGM resonance wavelength. Since the WGM resonance is an intrinsic property of the system, this approach is not as susceptible to complications that can arise from dye photobleaching or variable dye loading that are problematic for intensity based measurements. Typical Q-factors calculated from these spectra range from $2 – 5 \times 10^4$, which are on the order of Q-factors measured for microfabricated resonators, but orders of magnitude lower than that expected for microspheres.[1, 3] The dye attached to the surface of the microsphere acts as a source of loss in this arrangement which lowers the Q-factor. We are currently exploring optimal dye loading conditions to maximize the Q-factor.

2.4.2 Sensor Calibration

To demonstrate that the WGMI approach can track changes in WGM resonance wavelength, calibration plots were measured where the refractive index of the bathing solution was systematically increased. Figure 2.7 plots a typical calibration curve measured using the fluorescence imaging

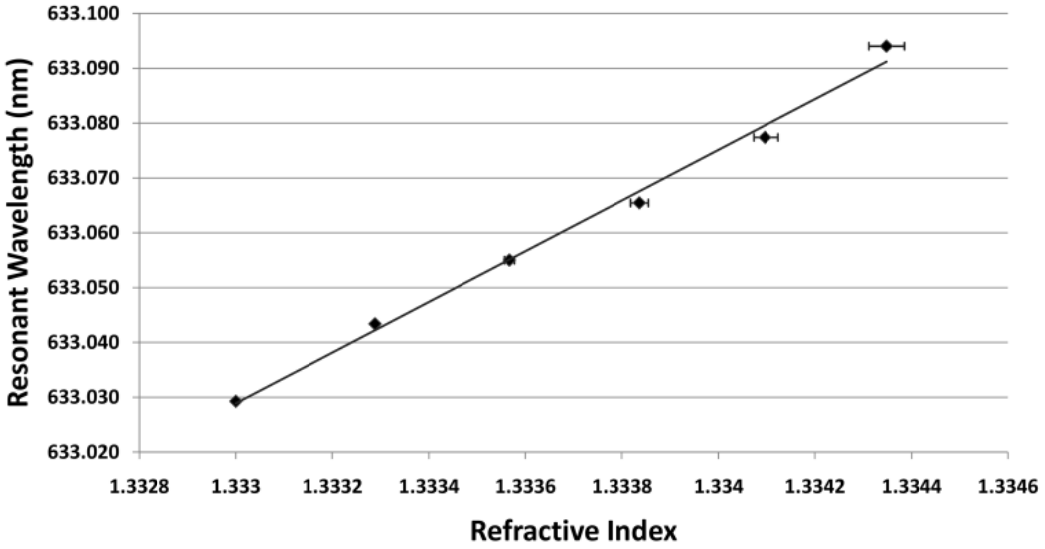

Figure 2.7: Refractive index calibration plot measured for a 53 μm sphere.

approach. In these experiments, microsphere resonators were bathed in 18 MΩ water to which injections of absolute ethanol were added to increase the surrounding refractive index.[29] As seen in Fig. 2.7, a linear response is observed as expected from the relationship between WGM resonance wavelength and refractive index (Eq. 2.1). The particular calibration plot shown in Fig. 2.7 was measured from a microsphere with a Q-factor of $\sim 2 \times 10^4$ and has a measured sensitivity of ~50 nm / RIU (refractive index units) and a detection limit of $\sim 2.6 \times 10^{-5}$ RIU. Linear calibration plots such as that shown in Fig. 2.7 illustrate the feasibility of using microsphere resonators combined with fluorescence imaging for biosensing.

2.4.3 Ovarian cancer biomarker detection by WGMI

Having demonstrated that the WGMI approach is sensitive to changes in the refractive index, the specific biosensing capabilities are demonstrated using antibodies specific for biomarkers of ovarian cancer. Two separate assays were performed with microspheres modified with antibodies specific for cancer antigen-125 (CA-125) and tumor necrosis factor-α (TNF-α), both implicated in the pathogenesis of ovarian carcinoma.[22-27] As illustrated in Fig. 2.5, the antibodies are attached to the sphere surface along with the fluorescent dye. Moreover, each antibody is attached to a distinct sphere size, thus encoding the analyte identity into the sphere diameter which is easily measured in the imaging approach. Here monoclonal antibodies specific for CA-125 were immobilized on 38 μm spheres while antibodies for TNF-α were attached to 53 μm spheres.

Figure 2.8 plots the shifts in WGM resonant wavelength as CA-125 was injected into the perfusion chamber. A linear shift in the resonant wavelength is observed with a measured CA-125 sensitivity of ~6 pm / U/mL and detection limit of ~1.5 U/mL. This detection limit is threefold better than the ~5 U/mL detection limit of commercial ELISA kits (Panomics BC-1013). Also shown in Fig. 2.8 is a similar calibration plot for the detection of TNF-α using 53 μm spheres functionalized with monoclonal antibodies for TNF-α. The linear response of TNF-α shown in Fig. 2.8 has sensitivity of ~108 pm / ng/mL

and a detection limit of ~240 pg/mL. Interestingly, the sensitivity is approximately an order of magnitude higher than previous microresonator reports using other antibody-antigen sensing

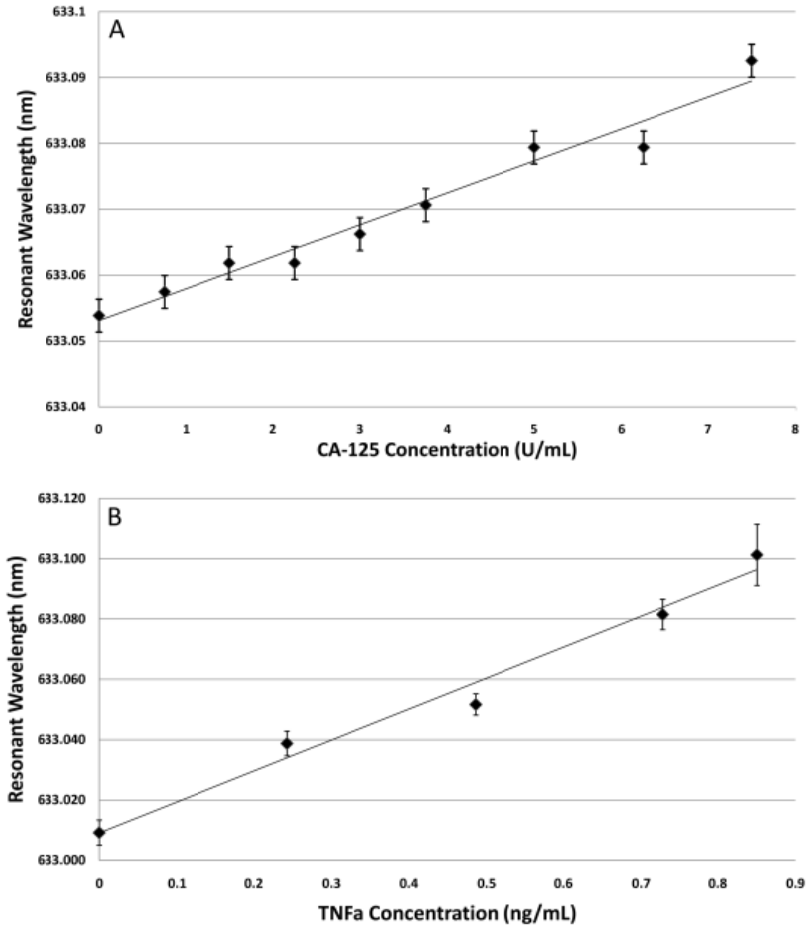

Figure 2.8: **(A)** Calibration plot of WGM resonance versus CA-125 measured using 38 µm microsphere resonators modified with anti-CA-125 antibodies and the fluorescent dye Alexa 633. Binding of CA-125 to the immobilized antibody alters the effective refractive index, leading to shifts in the WGM resonance. The linear calibration plot (R^2 = 0.9677) has a sensitivity of ~6 pm / (U/mL). **(B)** Calibration plot of WGM resonance versus TNF-α measured using 53 µm microsphere resonators modified with anti-TNF-α antibodies and the fluorescent dye Alexa 633. The linear calibration plot (R^2 = 0.9798) has a sensitivity of ~108 pm / ng/mL.

modalities. This may arise from differences in the specific K_D values for the antibody-antigen pairs used in these studies.[30-32] However, the shorter excitation wavelength used here may also influence microresonator sensor performance through changes in mode volume and mode density.[33] Future experiments are planned to quantify these effects.

The calibration plots shown in Fig. 2.8 demonstrate the specific detection of biomarkers using the WGMI approach. Coupling WGM resonators with sensitive fluorescence imaging offers many advantages for the multiplexed detection of biomarkers. The approach is label-free, sensitive, and rapid. Since the analyte identity is encoded in the sphere size or location, every sphere can be labeled with the same dye and excited with the same laser system. Since the WGM resonance wavelength is an intrinsic property of the system, the assay does not suffer from complications arising from dye photobleaching or variable labeling. Microspheres are readily available, inexpensive, come in a range of materials and sizes, and have extremely large Q-factors which are desirable for sensing applications. Finally, their small size makes them compatible with many of the developments taking place in the lab-on-a-chip field, which can further reduce assay costs.

2.5 Conclusions

Fluorescence imaging is combined with total internal reflection excitation of whispering gallery modes in resonators to develop a new approach for multiplexed biosensing. In this approach, microspheres are functionalized with a fluorescent dye that acts as a reporter of the WGM resonance. Light is coupled into a field of microspheres using the evanescent field created in a total internal reflection microscope. As the excitation wavelength is scanned, WGM resonances are detected through fluorescence imaging. As a particular sphere reaches a WGM resonance, a distinct ring of enhanced fluorescence is observed as the evanescent wave from light circumnavigating the sphere excites the surface attached dye. This approach enables the simultaneous measurement of WGM resonances from every microsphere in the field of view, thus enabling the development of highly multiplexed biosensors.

To demonstrate the feasibility of biosensing using the WGMI approach, antibodies specific for CA-125 and TNF-α were linked to 38 μm and 53 μm spheres, respectively. CA-125 and TNF-α are commonly used markers for the screening of ovarian cancer and by linking their antibodies to

differentially sized microspheres, detection specificity is encoded into sphere diameter. Binding of their associated antigens shifts the WGM resonance of the sphere, which is detected using fluorescence imaging. Calibration curves measured in separate assays reveals a linear response for both antigens with the detection limits for CA-125 over threefold better than that obtained with commercial ELISA approaches. These results confirm that fluorescence imaging can be used to simultaneously detect WGMs from a field of microsphere resonators where analyte identity can be encoded into sphere size and/or location, thus enabling significant multiplexing capabilities.

The major drawback associated with this approach is the method of excitation. Using a TIRF microscope for excitation introduces a considerable degree of cost to the instrumental design. Also, since a high-NA objective must be used, the field of view is limited and the coupling efficiency into the resonators is poor. The small region can excite only a limited number of resonators simultaneously, presenting scalability challenges using the TIR microscope. In addition, these studies were performed in buffer systems, and as with any viable screening method, the approach must be amenable for use in clinical serum samples. To address these issues, Chapter 3 will discuss instrumental modifications to increase the multiplexing ability of the WGMI technique, and the expansion of the method to measure cancer biomarkers present in clinical serum samples.

References

1. Gorodetsky, M. L.; Savchenkov, A. A.; Ilchenko, V. S., *Opt. Lett.* **1996,** *21* (7), 453-455.
2. Knight, J. C.; Cheung, G.; Jacques, F.; Birks, T. A., *Opt. Lett.* **1997,** *22* (15), 1129-1131.
3. Fan, X.; White, I. M.; Zhu, H.; Suter, J. D.; Oveys, H. In *Overview of novel integrated optical ring resonator bio/chemical sensors*, San Jose, CA, USA, Kudryashov, A. V.; Paxton, A. H.; Ilchenko, V. S., Eds. SPIE: San Jose, CA, USA, 2007; pp 64520M-20.
4. Teraoka, I.; Arnold, S.; Vollmer, F., *J. Opt. Soc. Am. B* **2003,** *20* (9), 1937-1946.
5. Vollmer, F.; Braun, D.; Libchaber, A.; Khoshsima, M.; Teraoka, I.; Arnold, S., *Appl. Phys. Lett.* **2002,** *80* (21), 4057-4059.
6. Soria, S.; Berneschi, S.; Brenci, M.; Cosi, F.; Nunzi Conti, G.; Pelli, S.; Righini, G. C., *Sensors* **2011,** *11* (1), 785-805.
7. Vollmer, F.; Arnold, S., *Nat. Methods* **2008,** *5* (7), 591-596.
8. Chiasera, A.; Dumeige, Y.; Feron, P.; Ferrari, M.; Jestin, Y.; Conti, G. N.; Pelli, S.; Soria, S.; Righini, G. C., *Laser Photonics Rev.* **2010,** *4* (3), 457-482.
9. Hoa, X. D.; Kirk, A. G.; Tabrizian, M., *Biosens. Bioelectron.* **2007,** *23* (2), 151-160.
10. Fan, X. D.; White, I. M.; Shopoua, S. I.; Zhu, H. Y.; Suter, J. D.; Sun, Y. Z., *Anal. Chim. Acta.* **2008,** *620* (1-2), 8-26.
11. Kippenberg, T. J. A. Nonlinear optics in ultra-high-Q whispering-gallery optical microcavities. 2004.
12. Yalcin, A.; Popat, K. C.; Aldridge, J. C.; Desai, T. A.; Hryniewicz, J.; Chbouki, N.; Little, B. E.; Oliver, K.; Van, V.; Sai, C.; Gill, D.; Anthes-Washburn, M.; Unlu, M. S.; Goldberg, B. B., *IEEE J. Sel. Top. Quant.* **2006,** *12* (1), 148-155.
13. Washburn, A. L.; Gunn, L. C.; Bailey, R. C., *Anal. Chem.* **2009,** *81* (22), 9499-9506.
14. Vollmer, F.; Arnold, S.; Braun, D.; Teraoka, I.; Libchaber, A., *Biophys. J.* **2003,** *85* (3), 1974-1979.
15. Hanumegowda, N. M.; White, I. M.; Oveys, H.; Fan, X., *Sens. Lett.* **2005,** *3*, 315-319.
16. Zhu, H.; Suter, J.; White, I.; Fan, X., *Sensors* **2006,** *6* (8), 785-795.
17. Nuhiji, E.; Mulvaney, P., *Small* **2007,** *3* (8), 1408-1414.
18. Hanumegowda, N. M.; White, I. M.; Fan, X., *Sensor. Actuat. B-Chem.* **2006,** *120* (1), 207-212.
19. Ren, H.-C.; Vollmer, F.; Arnold, S.; Libchaber, A., *Opt. Express* **2007,** *15* (25), 17410-17423.
20. Washburn, A. L.; Luchansky, M. S.; Bowman, A. L.; Bailey, R. C., *Anal. Chem.* **2009,** *82* (1), 69-72.
21. Oraevsky, A. N., *Quantum Electron+* **2002,** *32* (5), 377-400.
22. Tian, C.; Markman, M.; Zaino, R.; Ozols, R. F.; McGuire, W. P.; Muggia, F. M.; Rose, P. G.; Spriggs, D.; Armstrong, D. K., *Cancer* **2009,** *115* (7), 1395-403.
23. Kenemans, P.; Yedema, C. A.; Bon, G. G.; von Mensdorff-Pouilly, S., *Eur. J. Obstet. Gynecol. Reprod. Biol.* **1993,** *49* (1-2), 115-124.
24. Dobrzycka, B.; Terlikowski, S. J.; Kowalczuk, O.; Kinalski, M., *Eur. Cytokine. Netw.* **2009,** *20* (3), 131-134.
25. Gupta, D.; Lis, C. G., *J. Ovarian. Res.* **2009,** *2*, 13.
26. Hermsen, B. B.; von Mensdorff-Pouilly, S.; Berkhof, J.; van Diest, P. J.; Gille, J. J.; Menko, F. H.; Blankenstein, M. A.; Kenemans, P.; Verheijen, R. H., *J. Clin. Oncol.* **2007,** *25* (11), 1383-9.
27. Dobrzycka, B.; Terlikowski, S. J.; Garbowicz, M.; Niklinska, W.; Bernaczyk, P. S.; Niklinski, J.; Kinalski, M.; Chyczewski, L., *Folia Histochemica Et Cytobiologica* **2009,** *47* (4), 609-613.
28. Axelrod, D., Total internal reflection fluorescence microscopy. In *Method. Cell Biol.*, Dr. John, J. C.; Dr. H. William Detrich, III, Eds. Academic Press: 2008; Vol. 89, pp 169-221.
29. Lide, D. R., 91 ed.; CRC Press: Boca Raton, FL, 2011.
30. Maynard, J.; Georgiou, G., *Annu. Rev. Biomed. Eng.* **2000,** *2*, 339-376.

31. Rathanaswami, P.; Babcook, J.; Gallo, M., *Anal. Biochem.* **2008,** *373* (1), 52-60.
32. Liu, G. Q.; Liu, Y.; Zhang, W.; Yu, X.; Zhang, H. W.; Zhao, R.; Shangguan, D.; Li, Y.; Shen, B. F., *Sens. Actuators, B* **2004,** *99* (2-3), 416-424.
33. Matsko, A. B.; Ilchenko, V. S., *IEEE J. Sel. Top. Quant.* **2006,** *12* (1), 3-14.

Chapter 3: Serum Biomarker Quantification Using Whispering Gallery Mode Imaging

3.1 Introduction

In Chapter 2, we discussed how fluorescence imaging can be used to track individual WGM resonances in glass microspheres. Using total internal reflection (TIR) microscopy to excite a field of microspheres, individual excitation spectra are extracted from fluorescence images collected as the wavelength is scanned. The approach was validated by measuring binding of CA-125 and tumor necrosis factor α (TNF-α) in buffer solution using fluorescently labeled microspheres with immobilized antibodies. Here we introduce a simplified method for launching WGMs into labeled microspheres by employing a Dove prism; this approach enables much larger fields of spheres to be simultaneously excited and imaged. Using this approach, we demonstrate the simultaneous measurement of WGM resonances from over 120 individual microresonators, illustrating the substantial multiplexing capabilities afforded by this method. To advance this technique toward clinical use, we also show that non-specific binding is not limiting by detecting CA-125 doped into serum samples. The eventual clinical utility of this approach is illustrated by measuring CA-125 levels in serum collected from a healthy donor and a patient diagnosed with ovarian cancer.

Through changes in the instrumental technique, the increased signal from microsphere resonators has revealed that the underlying mode structure within each cavity can be imaged. Imaging these patterns provides an opportunity to track analyte binding through changes in mode structure which would simplify the WGM imaging method even further. We introduce finite element analysis as a way to assist in exploring resonator geometries and conditions which optimize sensor performance, and discuss initial work using simulations which could eventually relate fundamental mode structure to observed patterns.

3.2 Materials and Methods

Barium-titanate glass microspheres were obtained from Mo-Sci Corporation (Rolla, MO). Anti-CA-125 mouse monoclonal antibodies (X75) were purchased from Abcam (Cambridge, MA). CA-125 ovarian tumor marker antigen was obtained from MP Biomedicals (Solon, OH) and used without further purification. The amine reactive succinimidyl ester of Alexa 633 fluorescent dye was obtained from Invitrogen Corporation (Carlsbad, CA), and perfusion chambers were obtained from Grace Bio-Labs (Bend, OR). Clinical human serum samples were acquired from Proteogenex Inc. (Culver City, CA). StartingBlock blocking solution was obtained from Thermo Pierce Products (Rockford, IL), and all other reagents, unless otherwise noted, were purchased from Fisher Scientific (Hampton, NH) and used without further purification.

To prepare the spheres for use in a WGM assay, 53µm diameter barium titanate microspheres were soaked in a 10% Contrad 70 solution in 18MΩ nanopure water for 1h and triply rinsed with nanopure. The spheres were then incubated in 30% hydrogen peroxide solution for 1hr to increase the number of hydroxyl groups on the surface.[1] After triply rinsing with nanopure water, ethanol, and toluene, the spheres were tumbled overnight in 6% APTES in toluene, and triply rinsed in toluene and ethanol to form an amine terminated surface. To attach antibodies to the spheres, samples were subsequently tumbled for 2hr in 6% glutaraldehyde solution in PBS and triply rinsed with PBS, then incubated overnight with anti-CA-125 mouse monoclonal antibodies overnight to immobilize the capture agent on the sensor surface. The microspheres were triply rinsed with PBS and labeled with Alexa 633 fluorescent dye. In order to block nonspecific adsorption sites, the spheres were tumbled for 2hr in a StartingBlock solution containing 5% BSA, 5% sucrose (w/v %) and refrigerated until used.

To perform WGM measurements on the prepared samples, microsphere resonators were deposited into PDMS wells adsorbed to glass coverslips and enclosed in a CoverWell perfusion chamber,

and subsequently immersed in a 1:1 solution of PBS:serum. Coverslips were attached to an uncoated BK7 Dove prism (Edmund Optics, Barrington, NJ) and mounted onto a three-axis robotic micromanipulator (MP-285, Sutter Instruments, Novato, CA). Light from an external cavity diode laser (TLB-6904, Newport Corporation, Irvine, CA) was free space coupled into the Dove prism resulting in total internal reflection, forming an evanescent wave at the center of the prism for coupling light into the resonators. Fluorescence was collected from above the sample with an upright microscope (Olympus BXFM, Center Valley, PA) equipped with a 10X UMPlanFL (0.3 NA) objective lens (Olympus), filtered (Thor Labs, Newton, New Jersey), and imaged on a CCD camera (Cascade 650, Roper Scientific, Tuscon, AR). Diode laser wavelength was controlled using LabVIEW (National Instruments, Austin, TX) and image collection and processing was performed with SlideBook software (Version 4.2.0.3, Intelligent Imaging Innovations, Denver, CO).

3.3 Results and Discussion

3.3.1 Incorporating Dove Prism Coupling Into Whispering Gallery Mode Imaging

In Chapter 2, we demonstrated the fluorescence imaging of WGM resonances using the evanescent field from a total internal reflection (TIR) microscope to launch into a field of dye labeled microspheres. The high numerical aperture (1.45 NA) objective needed to create the TIR field, however, limited the number of microspheres that could be simultaneously excited, increased the cost of the apparatus, and lowered the coupling efficiency of excitation into the microresonators.[2] Here we show that the much simpler arrangement shown schematically in Fig. 3.1 overcomes these drawbacks. As shown in Figure 3.1, excitation from a computer controlled tunable diode laser is sent into a Dove prism which directs light towards the substrate surface beyond the critical angle. This creates an evanescent field which is used to couple light into a field of microsphere resonators. By imaging the sample from

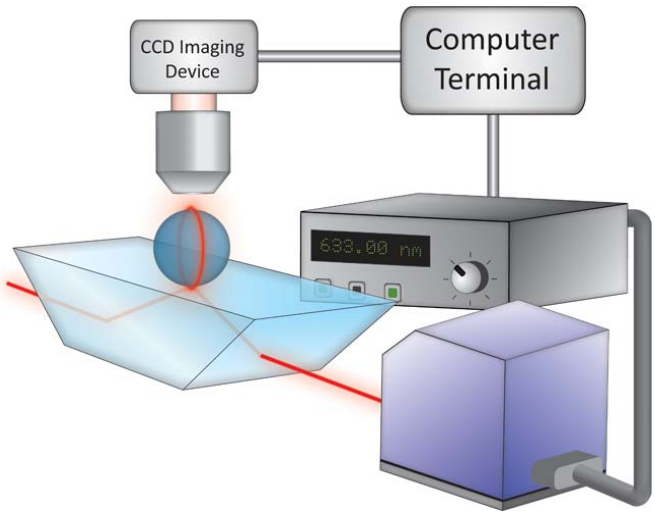

Figure 3.1: Schematic of the instrumental arrangement used for fluorescence imaging of WGM resonances in a field of microsphere resonators incorporating Dove prism excitation.

above, fluorescence excited from light stored within the microresonators is collected and detected in a similar manner as discussed in Chapter 2.

3.3.2 Highly Multiplexed Microsphere WGM Excitation

Figure 3.2 shows a representative fluorescence image from a field of microsphere resonators mounted on a Dove prism. The 868 µm x 654 µm field of view contains over 120 microspheres with mixed diameters of 53 µm and 63 µm. The microspheres exhibit a ring of fluorescence as light

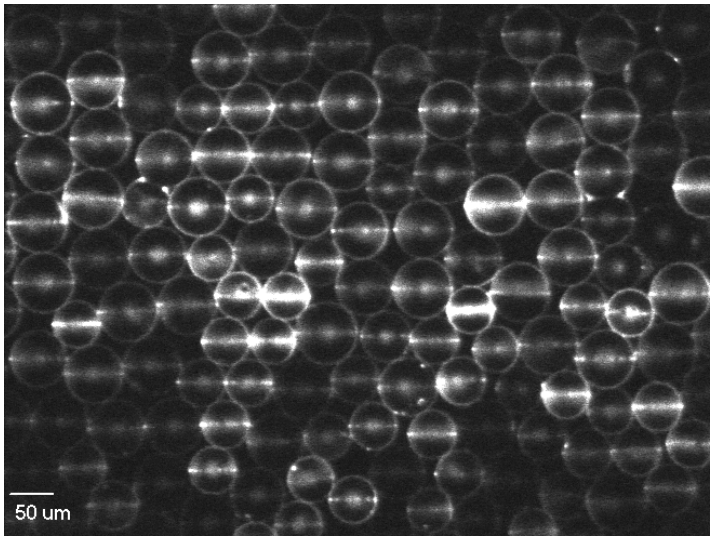

Figure 3.2: Snapshot of a size mix of fluorescently labeled microspheres mounted on a Dove prism undergoing WGM excitation.

circumnavigating within the sphere excites the surface attached dye through the associated evanescent field. While the fluorescent stripe around most spheres appears weak, a few spheres show particularly strong fluorescent stripes. These microspheres have WGM resonances near the excitation wavelength used to collect this image. As the excitation wavelength is scanned, different spheres come in and out of resonance which is easily tracked in the fluorescence imaging approach.

3.3.3 Sensor Validation and Characterization of Nonspecific Adsorption

In Chapter 2 we demonstrated that fluorescence imaging of WGM resonances can quantify the presence of the ovarian cancer marker CA-125 in buffer solutions. Here we extend those measurements to CA-125 detection in serum samples, where nonspecific interactions can play a more important role. Label-free detection schemes, like the one developed here, are generally susceptible to interference signals arising from non-specific binding.[3] These can be problematic for label-free approaches and often pose a significant challenge in developing new sensing schemes. In order to reduce nonspecific interference, a number of blocking approaches were utilized to test our WGM sensors' response following serum additions. To examine the effects of non-specific binding, the response of two microsphere resonators were compared with one another – one microsphere was labeled with dye and blocked using the approach outlined in section 3.2, while the other was labeled with dye but received no further treatment. The spheres were immersed in PBS and exposed to additions of human serum into the perfusion chamber. The spectral response of each sensor is illustrated in Figure 3.3. As seen in Figure 3.3, the blocked spheres **(A)** exhibit a linear red-shift in sensor response due to serum injections in PBS. Since the refractive index of human serum is greater than the PBS immersion medium, the bulk refractive index surrounding the resonator increases with each injection, resulting in a linear red-shift in the resonant wavelength, similar to the refractive index assay seen in Fig. 2.7. What is important in this graph is the lack of a nonlinear spike in the resonant wavelength, which would be indicative of a large degree of nonspecific protein binding, indicating that matrix effects due to human serum have been

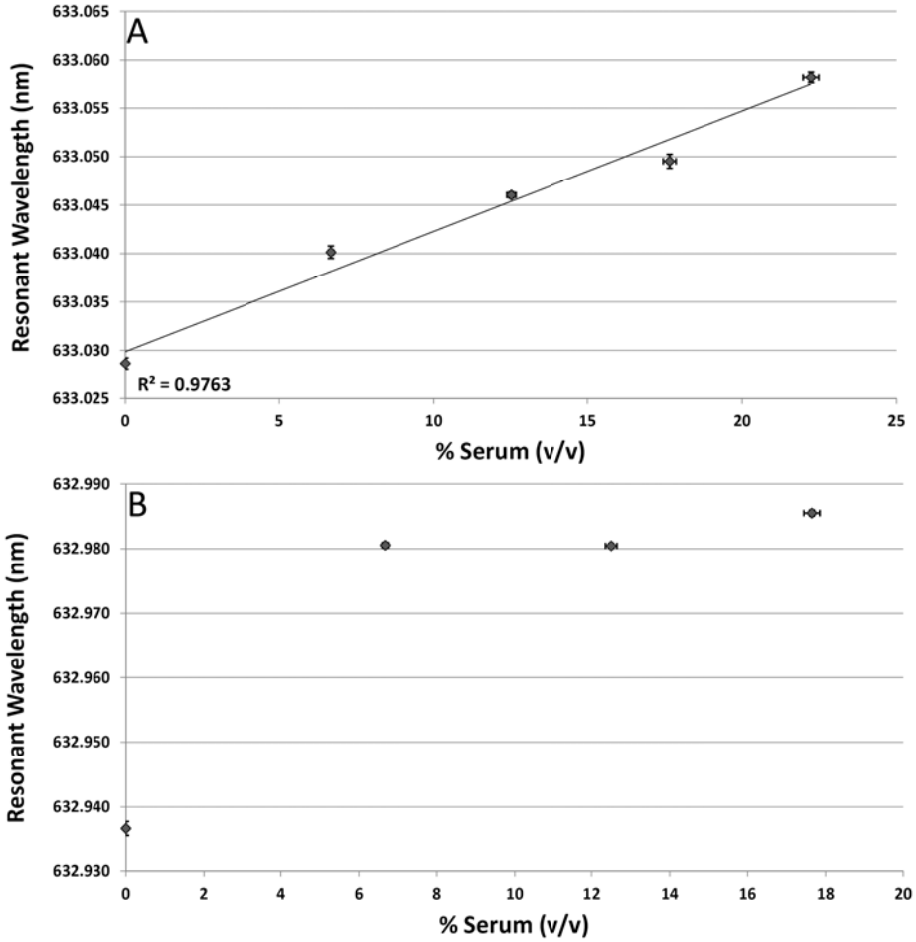

Figure 3.3: Comparison between **(A)** blocked and **(B)** unblocked responses to serum injections in PBS immersed WGM sensors.

reduced using this blocking method. As seen in graph **(B)** in Fig. 3.3, however, the unblocked sensor exhibits an immediate nonlinear red-shift upon the addition of serum to the immersion buffer. This is attributed to nonspecific adsorption of serum protein components to the sensor surface, resulting in the saturation of response from the unblocked sensor. The results outlined in Fig. 3.3 show that treatment with the appropriate blocking materials can sufficiently reduce nonspecific interactions in human sera, making measurements in complex media feasible using the WGM imaging method.

3.3.4 Detection of CA-125 in Complex and Clinical Samples

After employing the modified blocking agent, Fig. 3.4 shows a calibration plot for the detection of CA-125 in serum using pre-treated microspheres. The fluorescently labeled and blocked

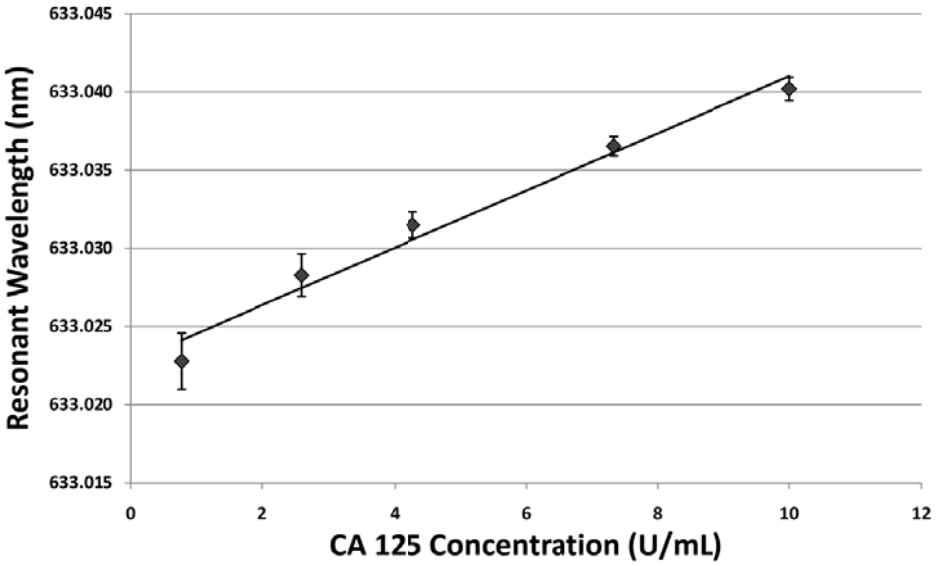

Figure 3.4: Calibration plot for the detection of the ovarian cancer marker CA-125 in serum.

microspheres were functionalized with anti-CA-125 monoclonal antibodies and immersed in a 1:1 solution of PBS:Serum. Sequential injections of CA-125 antigen in a 1:1 solution of PBS:Serum were added and the resonant wavelength shifts due to antigen binding were recorded to generate the calibration curve shown in Figure 3.4. The linear response has a measured sensitivity of 1.8 pm / (U/mL) and a detection limit of ~1.8 U/mL. These measurements show an improvement over a comparable commercial ELISA kit which exhibits detection limits of ~5 U/mL.

These encouraging results suggest that modified blocking agents are sufficient to minimize non-specific binding and enable the collection of linear calibration curves in complicated biological fluids. To explore the clinical utility of this approach, CA-125 was quantified in serum samples obtained from a healthy donor and from an ovarian cancer patient diagnosed with stage II adenocarcinoma. Each serum sample was diluted 1:1 in PBS and subjected to matrix-matched injections of CA-125; extrapolation of each linear plot is used to determine serum CA-125 levels. The results are displayed in Figure 3.5.

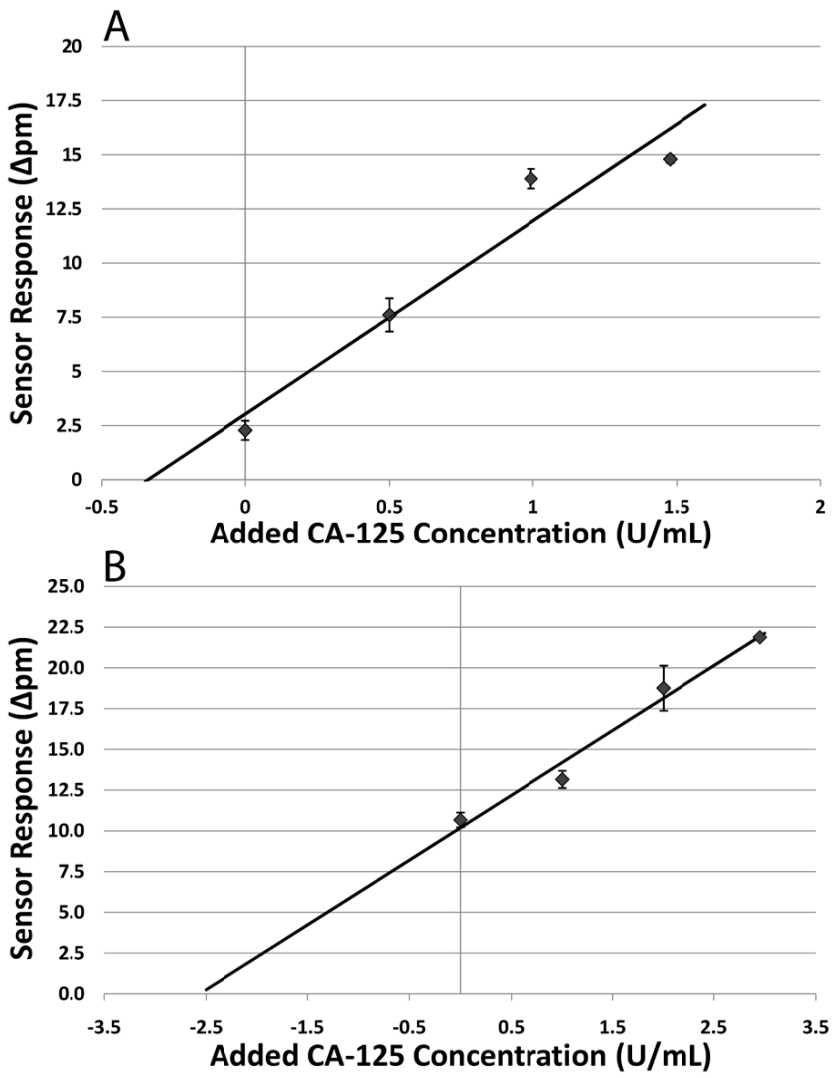

Figure 3.5: Standard addition assays carried out on serum samples obtained from a **(A)** healthy donor and **(B)** a patient diagnosed with stage II adenocarcinoma.

Plot **(A)** in Fig. 3.5 shows the results of measurements made on a serum sample collected from a healthy donor. Extrapolation of the standard addition curve reveals a CA-125 level of ~42 U/mL, consistent with the general baseline of levels of ~35 U/mL expected for healthy women.[4] Plot **(B)** in Fig. 3.5 represents a standard addition curve obtained with serum from a patient diagnosed with stage II adenocarcinoma; extrapolation of the curve results in a measured CA-125 serum concentration of ~316 U/mL, consistent with the elevated levels associated with ovarian cancer. This level is somewhat greater than the

reported value of ~224 U/mL obtained from the supplier. The elevated CA-125 concentration in the cancer patient is nearly an order of magnitude greater than baseline levels, consistent with levels expected for the pathogenesis of the disease. These measurements illustrate the utility of using fluorescence imaging of WGM markers to develop new assays that are compatible with complex biological media such as human serum.

The results presented in Figures 3.4 and 3.5 suggest that fluorescence imaging of WGM resonances provides a sensitive method for biomarker detection and quantification in complex biological media. For multiplexed sensing, Fig. 3.2 illustrates this potential where over 120 microspheres are simultaneously detected in an area less than a square millimeter. Additional goals in assay improvement include increasing resonator Q-factor by reducing dye loading to minimal concentrations and exploring different immobilization chemistries to examine and reduce their deleterious effects on Q-factor.

3.3.5 Fluorescence Imaging of Whispering Gallery Mode Structure

By employing a Dove prism for WGM excitation, the increase in signal to noise leads to the observation of patterns in the fluorescence intensity along the light path as seen in Figure 3.3. This

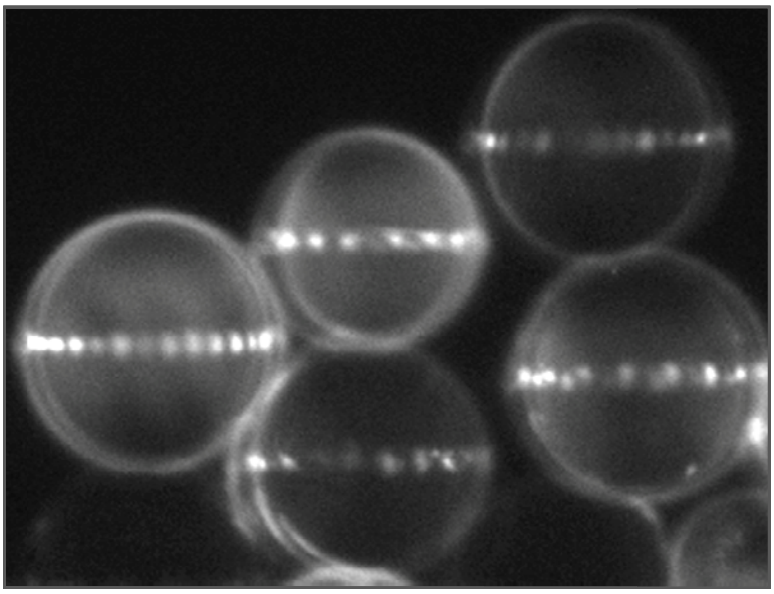

Figure 3.6: Whispering gallery mode structure visualized by fluorescence imaging.

structure is reflective of the underlying electromagnetic fields confined in the dielectric, and gives us a new approach for directly measuring whispering gallery mode structure. One advantage afforded by this phenomenon is the possibility of exploiting these patterns for new approaches to quantify refractive index changes or to track analyte binding. Using this property for sensing would be advantageous as the high resolution laser system used to measure the narrow WGM resonances would no longer be needed. Moreover, analyte quantification from mode structure measurements would greatly reduce the complexity of instrumentation used for point-of-care screens.

To examine mode structure response to refractive index changes, the series of images shown in Fig. 3.7 are far-field fluorescence images of a sphere taken as the surrounding refractive index is

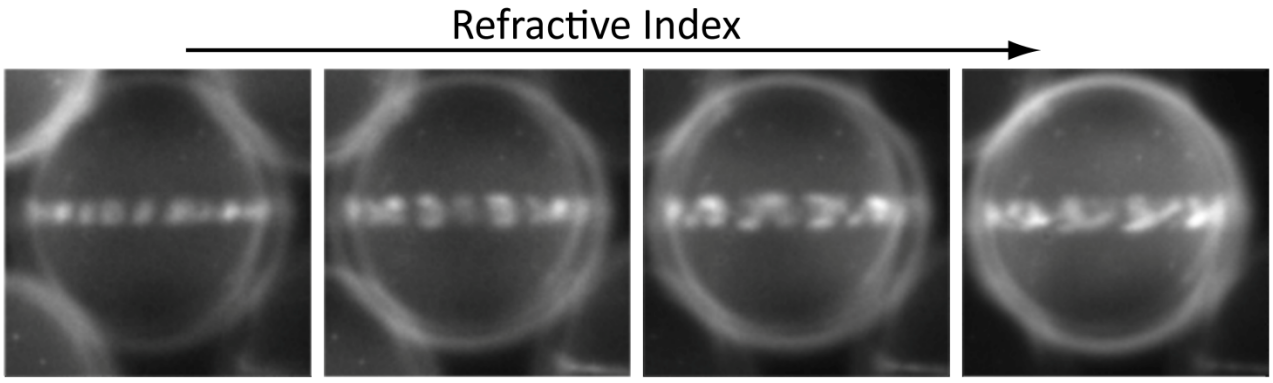

Figure 3.7: Mode structure changes in response to increasing refractive index.

increased. It is apparent in Figure 3.7 that the mode structure is altered as refractive index is increased, and could therefore be used for sensing purposes. The complex patterns seen are likely due to the interference of several modes excited in the resonator; multiple WGMs can be excited simultaneously since both the Q-factor of the sphere is finite, as is the bandwidth of the excitation source.[5] To exploit this property for sensing, future goals include using the banding patterns to create an image recognition algorithm calibrated by known refractive index standards. Post-calibration, an immunoassay would then be performed and target analyte concentration would be calculated using the calibrated algorithm. These measurements could result in a new direction for WGM sensor development that would obviate

the need for a high resolution laser system and enable the development and implementation of WGM sensors and assays using inexpensive conventional laser sources.

3.3.6 WGM Modeling Using Finite Element Analysis

One possible approach to interpret simple patterns formed from the mode structure seen in the previous section is through finite element analysis. The simulation program, COMSOL Multiphysics, has shown promise in simulating the EM fields in WGM resonances; a simplified example of this modeling process is shown in Figure 3.5. The geometry is first defined with a high-index circular structure encased

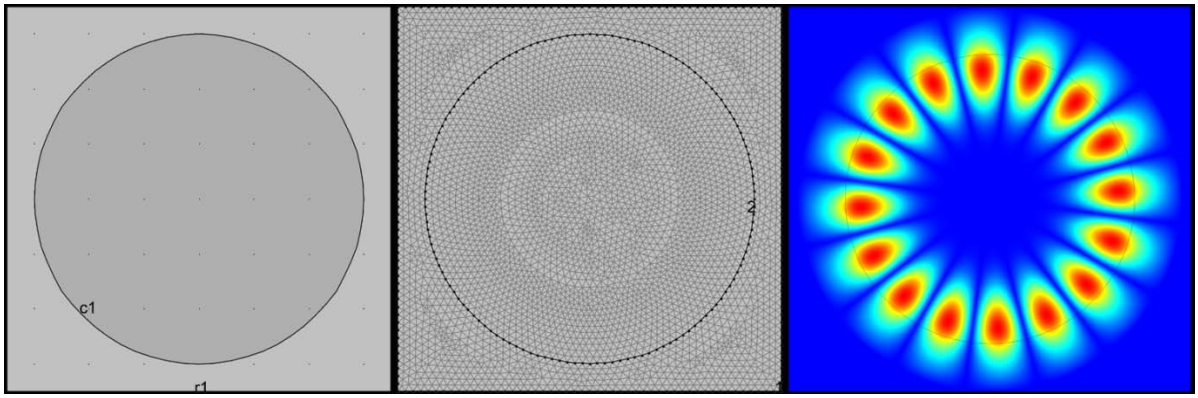

Figure 3.8: COMSOL model construction, meshing, and simulation of a simple WGM resonance.

in low-index surroundings, seen at left in Fig. 3.5. While our sensors are spherical, our initial studies reduce the problem to two dimensions for simplicity – future studies will incrementally work toward a full three-dimensional model of our system. After building the model, it is broken down into discrete, finite elements in a meshing process, seen in the center panel of Fig. 3.5. By solving Maxwell's equations for EM fields within the resonator, solutions can provide insight into simple WGM resonances. The right panel of Fig. 3.5 shows the simulated resonance of a 15μm diameter barium titanate cylinder in air with $m = 16$ (see Eq. 2.1). While these simulations are relatively easy to perform on simple geometries, scaling this process to the dimensions of our current experiment must be performed incrementally.[6, 7] Using this information, a pattern recognition algorithm may eventually be developed to correlate resonator mode structure changes with analyte binding.

3.4 Conclusion

A simplified method for launching WGMs into labeled microspheres by employing a Dove prism is introduced which enables much larger fields of spheres to be excited and imaged. We demonstrate the large multiplexing potential of this fluorescence approach by imaging over 120 microsphere resonators in an area less than 1 mm^2. To advance this technique toward clinical use, we also show that non-specific binding is not limiting by detecting CA-125 doped into serum samples. Linear calibration plots of sensor response with CA-125 levels were collected in 1:1 PBS:serum solutions, suggesting that non-specific interactions can be sufficiently minimized using standard blocking protocols. The immunoassay displayed a linear response with a sensitivity of ~1.8 pm / U/mL and limit of linearity of ~10 U/mL CA-125. The measured detection limit of ~1.8 U/mL is more than a factor of two better than commercial ELISA detection of CA-125.[8] Finally, we demonstrate the clinical utility of this approach by quantifying the CA-125 levels in a serum sample collected from an ovarian cancer patient diagnosed with stage II adenocarcinoma and compare that with levels measured in serum from a healthy donor. The measured CA-125 level in the healthy donor was ~42 U/mL, consistent with general baseline value of ~35 U/mL expected for healthy women. The measured CA-125 level in the cancer patient, however, was ~316 U/mL, nearly an order of magnitude higher than the normal baseline level and indicative of ovarian cancer pathogenesis. These results illustrate the utility of using fluorescence imaging of whispering gallery modes to quantify biomarkers in complex biological media. The large multiplexing potential of this label-free approach is of particular interest as the discovery of new biomarkers continues to expand.

Through changes in the instrumental technique, we demonstrate that the increased signal from microsphere resonators can be used to image the underlying mode structure within each cavity. Imaging these patterns provides an opportunity to track analyte binding through changes in mode structure which would simplify the WGM imaging method even further, potentially removing the

necessity of using high-resolution laser sources for WGM sensing. We also introduce using finite element analysis to assist in exploring resonator geometries and conditions which optimize sensor performance, and discuss initial work using simulations which could eventually relate fundamental mode structure to observed patterns.

As in all label-free assays, non-specific effects remain a concern for WGM detection and it is highly desirable that all immobilized antibodies be active. Despite the long historical development in immunoassay technology, however, immobilization protocols for antibodies remain surprisingly inefficient, often resulting in the amount of active immobilized antibody to less than 10-20%.[9-11] This obviously has deleterious effects on any immunoassay, but is particularly problematic with the WGM imaging method since the sensing region of our microsphere WGM resonators is restricted to a small area surrounding their equator. Moreover, if we consider the mode structure within the cavity, this further reduces the surface area sensed by the circulating light (see Fig. 3.9).

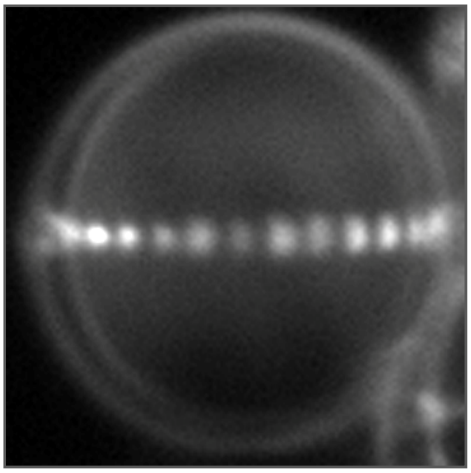

Figure 3.9: Microsphere WGM displaying mode structure.

These operational constraints place strict demands on the quality of the immobilized antibody sensing layer. It is well known that the orientation of immobilized antibodies is directly related to their binding efficiency. Antibodies oriented improperly may have their recognition site blocked, reducing sensor performance. The techniques employed to determine immobilized antibody orientations, however,

generally rely on indirect measurements and often simply correlate good assay performance with good orientation. Clearly, new methods are needed which can directly probe antibody orientation, specifically at single molecule levels. A technique capable of these measurements would help determine attachment protocols that optimize antibody activity, thus maximizing immunosensor performance. The following chapters are devoted to developing and validating an emerging fluorescence-based approach for determining the three-dimensional orientation of single molecules to obtain structural information in biological systems at the molecular level. Before these measurements can be applied to antibody systems, however, the fluorescence technique must first be validated in a well-controlled test system. The following chapters discuss the development of this technique, with the eventual goal of optimizing immobilization protocols to maximize antibody performance.

References

1. Chang, S. J.; Liao, W. S.; Ciou, C. J.; Lee, J. T.; Li, C. C., *J. Colloid. Interf. Sci.* **2009,** *329* (2), 300-305.
2. Huckabay, H. A.; Dunn, R. C., *Sensor. Actuat. B-Chem.* **2011,** *160* (1), 1262-1267.
3. Zhu, H. Y.; Dale, P. S.; Caldwell, C. W.; Fan, X. D., *Anal. Chem.* **2009,** *81* (24), 9858-9865.
4. Nossov, V.; Amneus, M.; Su, F.; Lang, J.; Janco, J. M.; Reddy, S. T.; Farias-Eisner, R., *Am. J. Obstet. Gynecol.* **2008,** *199* (3), 215-23.
5. Savchenkov, A. A.; Matsko, A. B.; Ilchenko, V. S.; Strekalov, D.; Maleki, L., *Phys. Rev. A* **2007,** *76* (2).
6. Cheema, M. I.; Kirk, A. G. In *COMSOL Conference*, Boston, **2010**.
7. Oxborrow, M., *IEEE T. Microw. Theory.* **2007,** *55* (6), 1209-1218.
8. Panomics, Cancer Antigen CA125 ELISA Test Kit User Manual - BC1013.
9. Jung, Y.; Jeong, J. Y.; Chung, B. H., *Analyst* **2008,** *133* (6), 697-701.
10. Plant, A. L.; Locasciobrown, L.; Haller, W.; Durst, R. A., *Appl. Biochem. Biotech.* **1991,** *30* (1), 83-98.
11. Herron, J. N. W., H.-K.; Janatova, V.; Durtschi, J.D.; Christensen, D.A.; Caldwell, K.D.; Chang, I.N.; Huang, S.-C., Orientation and Activity of Immobilized Antibodies. In *Biopolymers at Interfaces*, 2 ed.; Malmstein, M., Ed. Marcel Dekker: New York, 2003; pp 115-163.

Chapter 4: Antibody Immobilization Techniques and the Introduction of a Test System for Orientation Measurements at the Single Molecule Level

4.1 Antibody Efficiency Due to Preparation Procedures

In immunoassay design and execution, the crux of the technique relies on an antibody-antigen interaction. Commonly, the antibody is first immobilized on a substrate surface which can significantly impact both the orientation and the function of the antibody and can ultimately define how efficient an assay performs. Immobilization procedures strive to bind antibodies with their active site exposed to maximize binding efficiency. An example of antibodies bound in both random and directed orientations is illustrated schematically in Figure 4.1. Since the quality of the assay depends on efficient antibody-

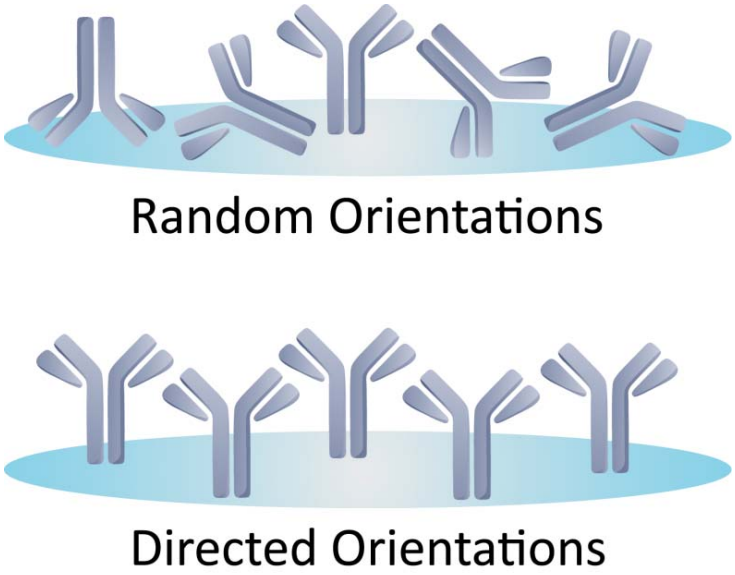

Figure 4.1: Directed and random antibody configurations.[1]

antigen binding and the diagnostics industry relies so heavily on immunoassay technology, there is considerable interest in developing immobilization procedures which maximize these interactions. Understanding the orientation of bound antibodies *in situ* and relating this information to assay efficiency is crucial for improving both the label-free techniques discussed in Chapters 2 and 3 and all capture techniques which rely on antibody-antigen interactions.

4.1.1 Antibody Immobilization Methods

The approaches used for antibody immobilization can be broadly grouped into three categories: adsorption, covalent binding and specific interaction-based methods. The most common immobilization techniques within these broad categories are outlined in Table 4.1. Out of all approaches listed,

Table 4.1: Common Ab immobilization approaches and their attributes, adapted from Ref 1, 2.

Immobilization Method	Surface Chemistry	Attachment Site	Advantages	Disadvantages
Adsorption	Agarose Polyacrylamide Nitrocellulose Poly-L-lysine Amino	Nonspecific Binding	Easy to perform.	Random orientations.
Covalent Binding	Maleimide Hydrazine Succinimidyl Ester Epoxide Aldehyde	Thiol Carbohydrate Amine Amine Amine	Stable binding & easy to perform.	Antibody pretreatment sometimes needed. Random orientations occasionally.
Affinity Based	Protein A/G Streptavidin Cellulose Nickel Copper Glutathione	Fc Region Biotin CBM* Histidine Tag Histidine Tag GST Tag	Directed orientation.	Must be used for specific antibody classes. Labor-intensive, and long-term stability problems

*CBM – Carbohydrate Binding Molecule

nonspecific adsorption approaches offer the quickest route to antibody immobilization. Many multi-well plate-based ELISA techniques employ the adsorption technique in plastic wells without pretreatment, making this approach appealing since there is little labor involved. Unfortunately, the adsorption method inherently results in random antibody orientations. In addition, the antibodies are bound only by electrostatic interactions, so certain buffer conditions will result in desorption and thus loss of activity. Since this approach offers no control over antibody orientation, it is a poor choice to employ for assays requiring maximal antibody performance as binding efficiencies for random orientations is generally ~10%.[2, 6, 7]

Covalent approaches are slightly more labor intensive but are still considered easy to perform. Since the antibody is covalently bound to the substrate surface, this method is the most stable approach to immobilization. The drawbacks to this technique are that some methods require additional modification of the antibody which can result in loss of function, and binding can attach to numerous functional groups on the structure, often resulting in randomly oriented antibodies and again reducing efficiency to ~10%.[2, 6, 7]

Affinity-based methods currently provide the greatest degree of orientation control, with antibody-antigen binding efficiencies reported to be as high as ~83%.[8] This approach employs natural proteins and engineered materials to bind antibodies in a designed to expose their active region for near-maximum binding efficiency. The drawbacks associated with this technique are that it is quite labor intensive and the stability of the macrostructure is much less robust than that obtained through covalent binding. Ion screening in some buffer conditions can cause these complexes to break down, and long-term storage capabilities are difficult as compared with other techniques.[2, 6, 7]

While considerable work is being invested in finding the most efficient antibody immobilization procedure, there is a need for techniques capable of measuring the resulting orientation of the immunogen. This information can be used to fine-tune immobilization protocols to maximize antibody activity in immunoassay design.

4.2 Common Methods Used to Measure Antibody Efficiency and Orientation

As mentioned in the previous section, proper orientation of the antibody is crucial for efficient immunoassay performance. Just as there is a substantial amount of effort directed towards antibody immobilization techniques, there are numerous techniques which are utilized to approximate antibody orientation. An overview of these methods and their attributes is outlined in Table 4.2.

Table 4.2: Instrumental techniques used to measure antibody orientation.

Technique	Mechanism	Advantages	Disadvantages
Antibody Binding Measurements[9, 10] (Numerous)	Comparison of instrument response (SPR, ELISA turnover, fluorescence intensity, etc.) to different immobilization strategies.	Generally easy to perform	Can only assume orientation. No direct information provided.
Microbalance[11, 12]	Mass measurement (approximates orientation via antibody loading)	Straightforward	Assumes homogenous antibody distribution. Cannot distinguish Fab-up versus Fab-down.
AFM*[13, 14]	Topographically infers orientation	Effective at approximating numerous orientations.	Very difficult in liquid samples. Poor throughput.
TOF-SIMS**[15]	Amino acids exposed to outer surface are compared to known sequence.	Has promise in directly observing Ab orientation.	Extremely difficult. Must be performed in dry samples (ex situ).
Neutron Reflection[14, 16]	Measures protein density as a function of surface distance.	Can use information to infer absolute protein orientation	Difficult and expensive. Cannot directly probe orientations.

*AFM – Atomic Force Microscopy
**TOF-SIMS – Time-of-Flight Secondary Ion Mass Spectrometry

4.2.1 Antibody Binding Measurements

In antibody binding measurements, the orientation is inferred through the efficiency of binding in immunoassays, simply correlating good signal with good orientation. These techniques, however, cannot distinguish between antibody orientation and degree of denaturation due to the immobilization process. The methods can determine which immobilization procedures result in higher instrumental response, but provide no information regarding antibody orientation.

4.2.2 Microbalance Measurements

Microbalance approaches approximate antibody orientation through mass loading by making a broad assumption that the antibody distribution is homogenous. Like the above measurements, this technique cannot discern between denatured or differentially oriented antibodies. As discussed previously, nonspecific adsorption and covalent binding often result in randomly oriented antibodies, rendering this technique incapable of measuring antibody orientations.

4.2.3 AFM Studies

Atomic force microscopy uses topographical features to approximate orientation by visualizing the domain structure and height differences formed from immobilized antibodies. While this technique can provide some degree of information regarding antibody orientation, the information it provides is often quite ambiguous and difficult to interpret. In addition it has extremely low throughput and is difficult to perform in aqueous samples, making in situ measurements problematic.

4.2.4 Time-of-Flight Secondary Ion Mass Spectrometry

In TOF-SIMS, an antibody-functionalized substrate is bombarded with an ion source and the chemical profile of ejected amino acid secondary ions is compared to a known sequence of the immobilized immunogen. While this technique has shown promise in determining the orientation of surface bound antibodies, it is highly complex, expensive, and must be performed on dry samples in vacuum. This is a substantial drawback, as method is not amenable to probing antibodies in relevant buffered solutions, and introducing the substrate to such conditions may result in antibody denaturation. The TOF-SIMS approach is therefore ill-suited for our goals.

4.2.5 Neutron Reflection

This technique measures the degree of neutron reflection with respect to distance from a target substrate. Using this method, the protein density versus surface distance can be used to approximate antibody orientation in a sample. The drawback with this method is that it is both difficult to perform and expensive in practice. In addition, this technique is based on ensemble averaged measurements, and therefore may average heterogeneous behavior, which is again an issue for random antibody orientations.

4.2.6 Probing Antibody Orientation

The previous sections provide a brief overview of the methods currently employed for inferring antibody orientation on substrate surfaces. Most of these methods cannot directly determine antibody

orientations, but generally correlate good activity with proper orientation based on immunoassay performance. In addition, most of these methods rely on information gathered from bulk measurements. This ensemble averaging can miss heterogeneous behavior such as domain formation in substrate bound antibody systems. As most antibody immobilization approaches result in random attachment, averaging techniques would fail to discern the full distribution of antibody orientations.

Clearly, a new approach is needed which can directly measure antibody orientation and correlate this information with immobilization protocol. The method must be capable of obtaining all molecular orientations within the system independently in order to capture any heterogeneous behavior. In addition, the method must have the ability to perform these measurements both in situ and without disturbing the immobilized antibodies. We therefore must explore a new approach to probe molecular orientation free from ensemble averaging.

4.2 An Emerging Fluorescence Approach for Measuring Molecular Orientations

Previously it has been shown that an emerging fluorescence technique can measure the three-dimensional orientation of single-molecule reporter probes. This technique provides a unique opportunity to directly probe molecular orientations in model and biological systems. Consider a beam of light impinging on an interface between a medium of high refractive index and a medium of lower refractive index as illustrated in Fig. 4.2. When the incident angle increases beyond the critical angle, θ_c, light is no longer refracted into medium n_2, but is totally internally reflected back into medium n_1. While the light beam is totally reflected into medium n_1, an exponentially decaying evanescent wave is still produced which extends into the medium of lower

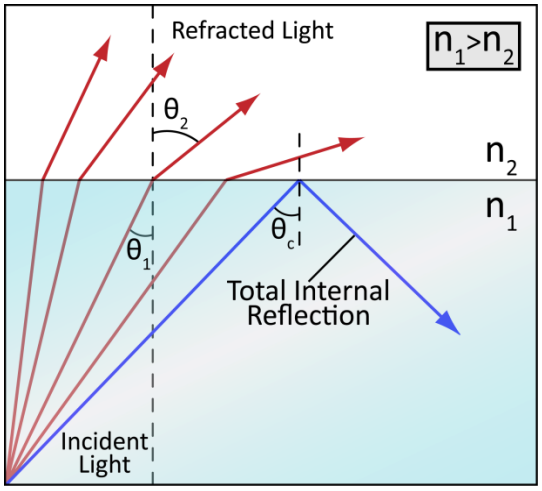

Figure 4.2: Light incident upon a refractive index-mismatched boundary.

refractive index. This field may be utilized in microscopy to excite fluorescent markers close to the imaging surface and has been employed as a background reduction method since the evanescent tail reaches only hundreds of nanometers above the surface.[17, 18] An example of the geometry employing total internal reflection fluorescence microscopy (TIRF-M) is illustrated in Figure 4.3. In this setup, laser light is directed into a high numerical aperture objective lens. If the excitation beam is offset from the center of the back aperture of the lens, the incident angle on the substrate is increased. As this offset progresses, TIR is eventually reached and an evanescent field is produced at the sample surface. Resulting fluorescence from reporter molecules on the substrate are collected in an epifluorescence fashion and imaged onto a detector array. The field has progressed to a point where the fluorescence from single molecules can easily be measured. An example of this capability is shown in Figure 4.4. Each Gaussian feature in the image represents the fluorescence from a single fluorophore, showing the high signal-to-noise ratio capable using this approach.

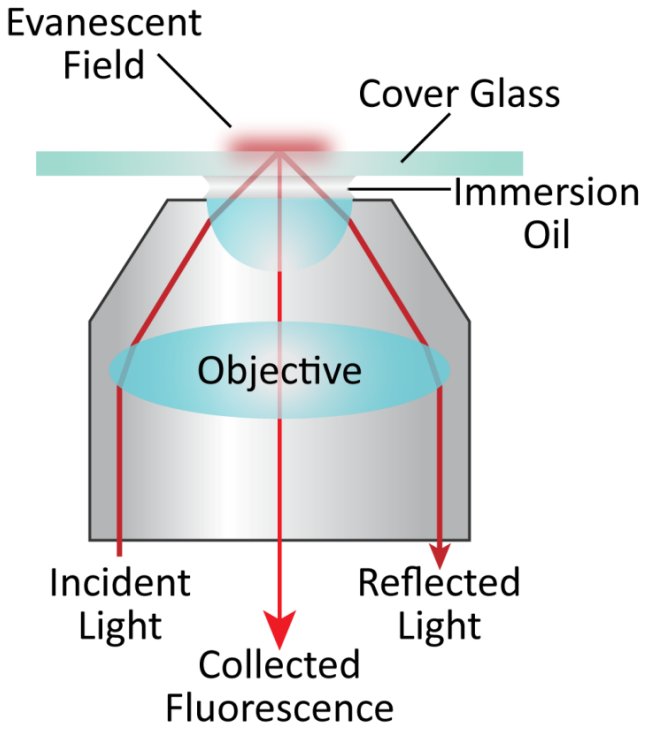

Figure 4.3. Fluorescence microscopy employing total internal reflection.[3]

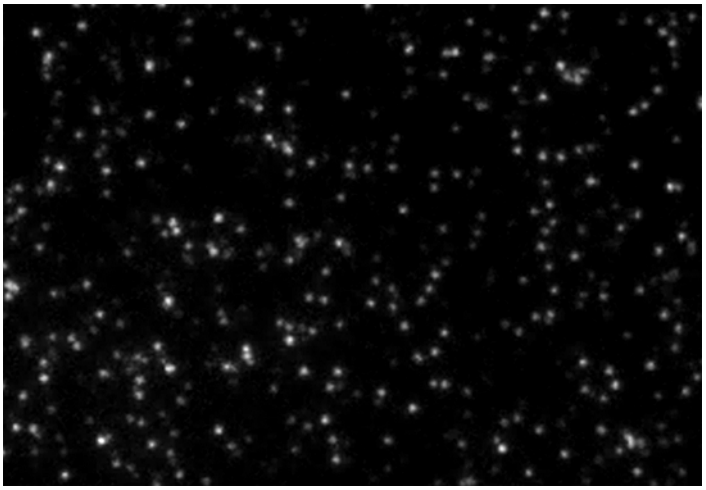

Figure 4.4: Fluorescence microscopy image of single molecule fluorophores in focus.

Several groups have shown that polarized total internal reflection fluorescence microscopy (PTIRF-M) can be used not only to image single molecules but capture their three-dimensional orientation in the sample.[19-23] When in free space, the emission dipole of a single molecule emits light in a sine squared pattern, illustrated schematically in Figure 4.5. If this emission dipole is brought near an interface that is refractive index mismatched, however, this emission pattern gets distorted as it is coupled into the interface. An example of this distortion is illustrated in Figure 4.6. The key feature of the radiation patterns shown in Figure 4.6 is that parallel and perpendicular emission dipoles couple emission into the collection optics at different angles. This shows that the orientation of single fluorophores will affect how fluorescence is coupled into the imaging optics. However, as seen in the microscopy image in Figure 4.4, single molecule fluorescence images produce

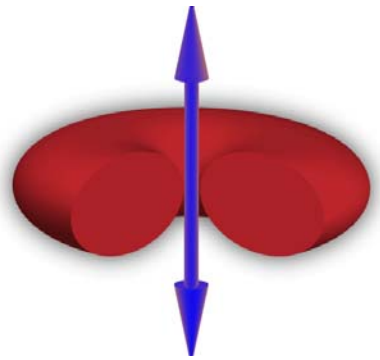

Figure 4.5: Fluorescence emission in free space, with the emission dipole indicated by the arrow.

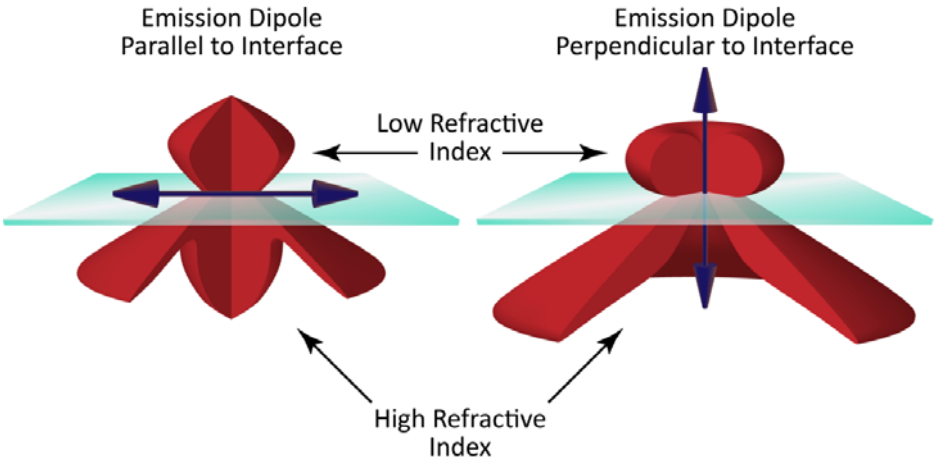

Figure 4.5: Schematic representation of emission dipoles oriented parallel and perpendicular to a glass interface.[3]

Gaussian emission profiles as light from all collection angles is brought to the same focal point. In order to capture the emission dipole information, spherical aberrations must be introduced into the optics train. These aberrations arise when light coupled into the periphery of an objective is not focused to the same point as light coupled into the center of the lens, an example of this is seen in Figure 4.7. In an instrumental setup, spherical aberrations will cause light entering the objective at different angles to ultimately be focused onto different regions of the detector array. Imaging single molecule fluorescence with spherical aberrations introduced into the collection optics, therefore, will produce intensity patterns on the detector array that reflect the emission dipole orientations. Experimentally, the most straightforward way to introduce these aberrations is by defocusing the collection optics ~500nm. An example of a single-molecule fluorescence image where spherical aberrations have been introduced is seen in Figure 4.8. As shown in Figure 4.8, a variety of emission patterns are observed in the

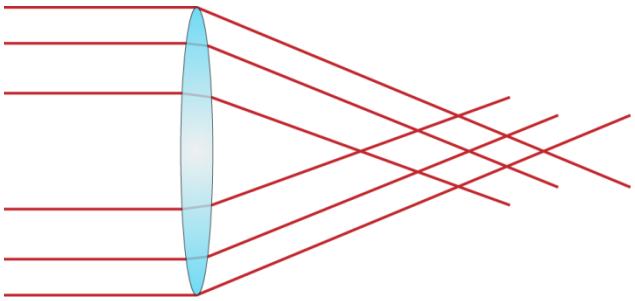

Figure 4.7: Example of spherical aberrations, where light passing through the periphery of the lens is focused to a different point than light passing through the lens' periphery.

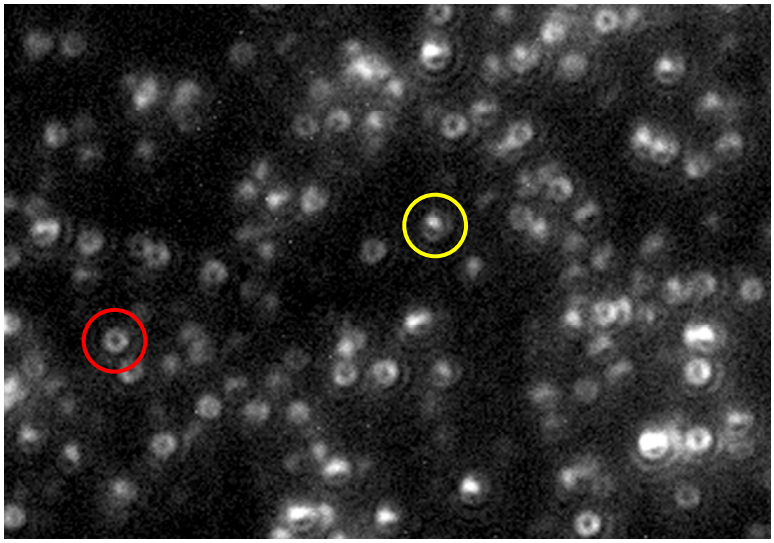

Figure 4.8: Single molecule image collected using out-of-focus PTIRF-M. The anisotropic fluorescence emission of the reporter molecule leads to the observed patterns.

fluorescence image. The pattern circled in red exhibits a donut-like shape which corresponds to an emission dipole oriented perpendicular to the collection surface. This pattern results from emission collected at high angles as seen in Fig. 4.5. The emission pattern circled in yellow exhibits a wing-like shape, with a greater intensity in the center and weaker fluorescence observed on the edges of the feature. This pattern corresponds to an emission dipole oriented parallel with the imaging surface where most of the fluorescence intensity is collected at low angles as seen in Fig. 4.5. These emission patterns can therefore be used as a marker for molecular orientation. By comparing collected information to calculated data, any arbitrary orientation can be discerned using this method. An example of this type of comparison can be seen in Figure 4.9. The tilt of the emission dipole away from the surface normal is termed the polar (Φ) angle, and the rotation about its axis the azimuthal (θ) angle. A graphic representation of this convention is shown in Figure 4.10.

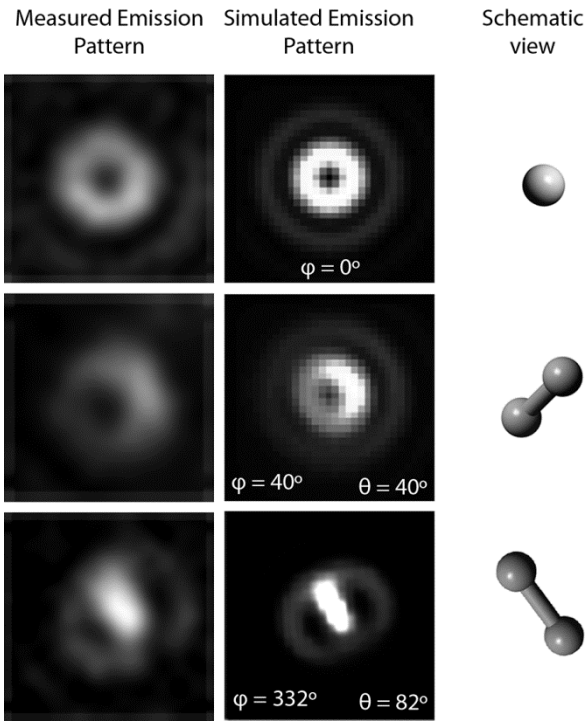

Figure 4.9: At left are experimentally collected single molecule emission patterns. Comparison of these patterns with simulated data at center allows for the calculation of the three-dimensional orientation listed which is shown schematically at right.[4]

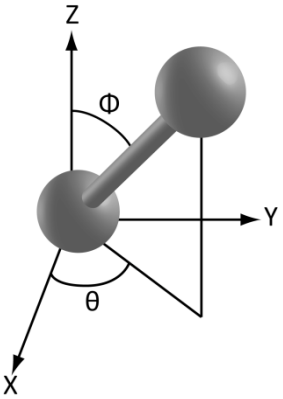

Figure 4.10: Polar coordinates used for assigning molecular orientations.

In order to probe fluorophores at any arbitrary orientation, the evanescent wave must have a field which can excite all possible orientations of the absorption dipole with respect to the substrate surface. This is

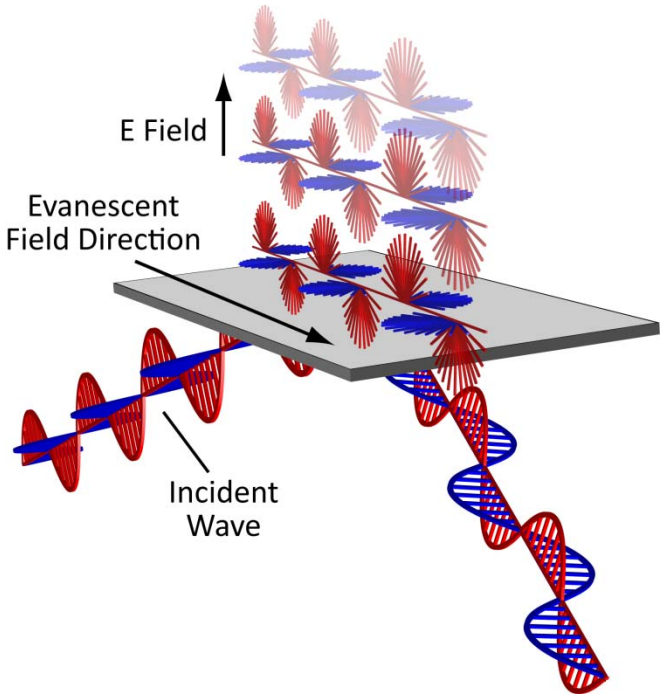

Figure 4.11: Schematic illustration of p-polarized total internal reflection.[3]

achieved through utilizing p-polarized light in TIRF-M; a representation of the evanescent wave produced from this type of excitation is shown in Figure 4.11. In Fig. 4.11, the electric field (red) from p-polarized light produces a "cartwheel" type effect when undergoing total internal reflection, enabling the excitation of any arbitrary fluorophore orientation.

This fluorescence approach enables the three-dimensional orientation of single molecules to be directly measured. By doping fluorescent probes into substrate supported systems therefore, the structural properties of these systems can be measured at the molecular level. Before applying the technique to immobilized antibody systems, however, this fluorescence method must first be validated in a well-characterized test system where molecular level structure is known and can be controllably changed. An ideal system for validating this approach includes the use of monolayer lipid membranes fabricated using Langmuir-Blodgett deposition. This technique enables precise control over the molecular structure of deposited films, and is well-suited to test and characterize the single-molecule fluorescence technique.

4.3 Langmuir-Blodgett Membrane Deposition

The Langmuir-Blodgett process allows for the precise control and deposition of lipid films on target substrates and thus provides an excellent system for exploring the effects of composition, temperature, and surface pressure on membrane systems.[24, 25] In this technique, amphipathic lipids are dissolved in a volatile solvent then deposited onto a water subphase as seen in Figure 4.12. The polar, hydrophilic headgroups are solvated by water molecules in the subphase and the nonpolar acyl tails are pushed out of the aqueous phase due to hydrophobicity, leaving the lipid molecules trapped at the air-water interface. The tendency of the lipids to spread on the subphase is countered by a movable

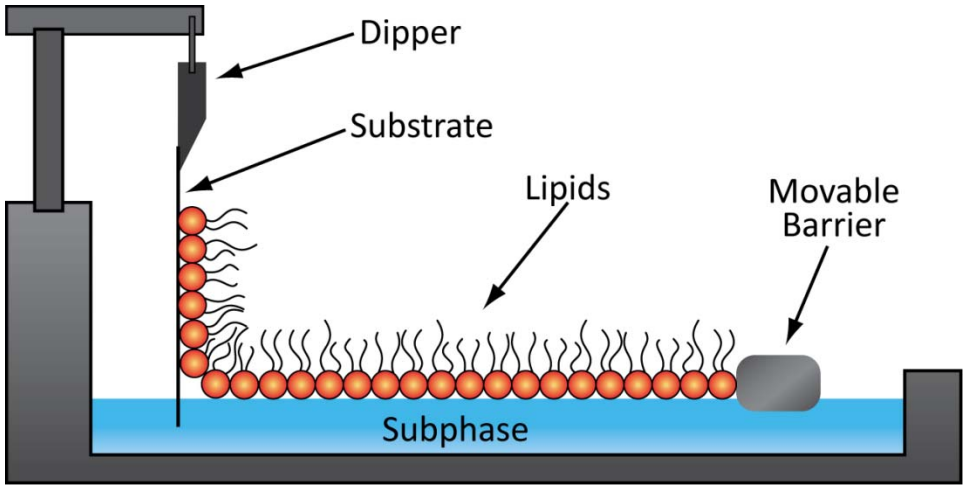

Figure 4.12: Schematic illustration of a Langmuir-Blodgett (LB) trough.

barrier. As the barrier is compressed it reduces the area of each lipid molecule, causing an increase in surface pressure of the monolayer confined to the subphase surface. The lipids can be compressed to a specified surface pressure and deposited evenly onto a substrate using a dipping mechanism. This ability to alter the surface pressure of the monolayer allows for precise thermodynamic control of the model system.

The test system we will employ for exploring the single molecule orientation measurements involves the amphipathic molecule dipalmitoylphosphatidylcholine (DPPC), a phospholipid which is a

major component of cellular membranes. Shown in Figure 4.13 is a pressure-area isotherm produced from compressing DPPC in a Langmuir-Blodgett trough. When the lipid film is under low compression

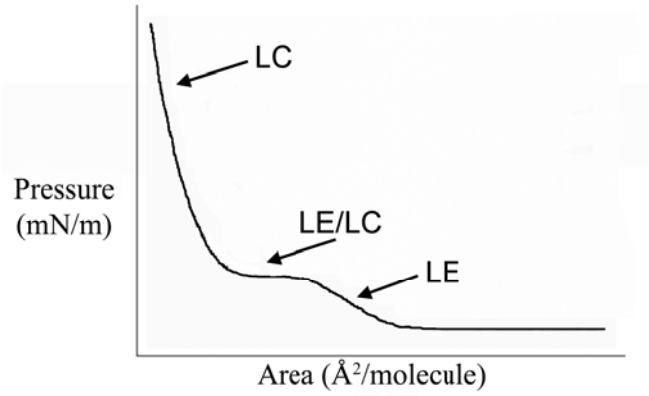

Figure 4.13: Representative isotherm of a DPPC monolayer undergoing compression on a Langmuir-Blodgett trough.

(<3mN/m), the lipids exist in a liquid-expanded (LE) phase, where the lipid film adopts a disordered state at the molecular level. Compressing the monolayer results in a plateau region in which the LE phase coexists with a liquid-condensed (LC) region where lipid packing and molecular order is elevated. Shown in Figure 4.14 is a confocal microscopy image of a DPPC monolayer doped with a fluorescent dye in the coexistence region.[5] The image shows bright and dark regions corresponding to the LE and LC phases,

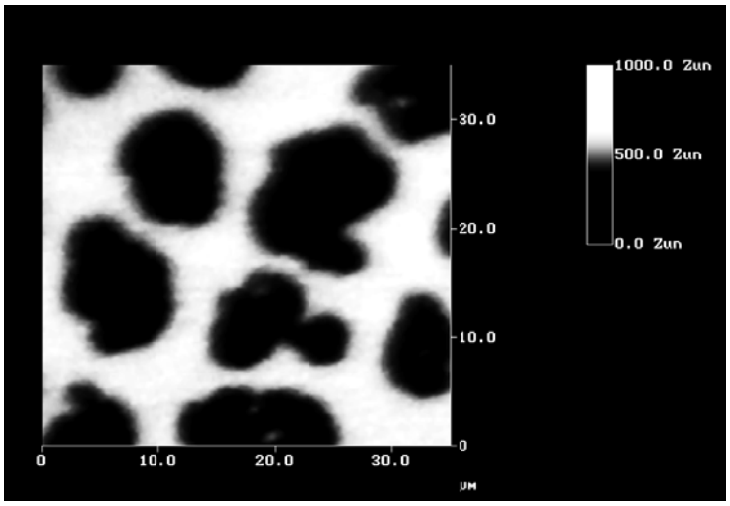

Figure 4.14: Confocal microscopy image of a DPPC monolayer deposited in the coexistence region.[5]

respectively, as the dye entropically partitions into the liquid-expanded region. As the monolayer is further compressed, the lipid molecules become tightly packed and exist in a highly ordered state dominated by the LC phase. Further compression leads to a solid-condensed (SC) phase before the monolayer eventually buckles and collapses into the subphase. Using the LB technique, therefore, monolayers can be deposited at any point along the pressure/area isotherm, thus allowing for very precise control of membrane structure at the molecular level.

LB monolayers of DPPC will serve as initial our test system to validate the single-molecule approach. A fluorescent lipid analog, BODIPY-PC, is doped into DPPC films at trace amounts. Previous studies have shown that this probe preferentially partitions into the less ordered phases present and has been used extensively in phase partitioning studies such as that shown in Fig. 4.14.[5, 26] For the single molecule studies, BODIPY-PC will serve as the reporter molecule as it is structurally similar to DPPC and contains its fluorophore in the acyl chain region of the lipid, where its orientation is most susceptible to changes in membrane structure. Through measuring the emission patterns of this reporter molecule as a function of surface pressure, we can use their orientations as a measure of molecular order in the system. The following chapters encompass the validation of the single-molecule approach through studying model membrane films as a function of surface pressure, additive concentration, and atmospheric conditions. Future goals for this technique include the direct measurement of immobilized antibodies to measure and subsequently optimize the efficacy of preparation protocols.

References

1. Seurynck-Servoss, S. L.; Baird, C. L.; Rodland, K. D.; Zangar, R. C., *Front. Biosci.* **2007,** *12*, 3956-3964.
2. Jung, Y.; Jeong, J. Y.; Chung, B. H., *Analyst* **2008,** *133* (6), 697-701.
3. Olympus Microscopy Primer. http://www.olympusmicro.com/primer/ (accessed Mar 2, 2012).
4. Armendariz, K. P.; Huckabay, H. A.; Livanec, P. W.; Dunn, R. C., *Analyst* **2012,** *137* (6).
5. Hollars, C. W.; Dunn, R. C., *Biophys. J.* **1998,** *75* (1), 342-353.
6. Herron, J. N. W., H.-K.; Janatova, V.; Durtschi, J.D.; Christensen, D.A.; Caldwell, K.D.; Chang, I.N.; Huang, S.-C., Orientation and Activity of Immobilized Antibodies. In *Biopolymers at Interfaces*, 2 ed.; Malmstein, M., Ed. Marcel Dekker: New York, 2003; pp 115-163.
7. Plant, A. L.; Locasciobrown, L.; Haller, W.; Durst, R. A., *Appl. Biochem. Biotech.* **1991,** *30* (1), 83-98.
8. Chen, H. X.; Huang, J. Y.; Lee, J.; Hwang, S.; Koh, K., *Sensor. Actuat. B-Chem.* **2010,** *147* (2), 548-553.
9. Kausaite-Minkstimiene, A.; Ramanaviciene, A.; Kirlyte, J.; Ramanavicius, A., *Anal. Chem.* **2010,** *82* (15), 6401-6408.
10. Bae, Y. M.; Oh, B.-K.; Lee, W.; Lee, W. H.; Choi, J.-W., *Biosens. Bioelectron.* **2005,** *21* (1), 103-110.
11. Caruso, F.; Rodda, E.; Furlong, D. N., *J. Colloid. Interf. Sci.* **1996,** *178* (1), 104-115.
12. Pei, Z. C.; Anderson, H.; Myrskog, A.; Duner, G.; Ingemarsson, B.; Aastrup, T., *Anal. Biochem.* **2010,** *398* (2), 161-168.
13. San Paulo, A.; Garcia, R., *Biophys. J.* **2000,** *78* (3), 1599-1605.
14. Xu, H.; Zhao, X. B.; Grant, C.; Lu, J. R.; Williams, D. E.; Penfold, J., *Langmuir* **2006,** *22* (14), 6313-6320.
15. Wang, H.; Castner, D. G.; Ratner, B. D.; Jiang, S. Y., *Langmuir* **2004,** *20* (5), 1877-1887.
16. Xu, H.; Zhao, X. B.; Lu, J. R.; Williams, D. E., *Biomacromolecules* **2007,** *8* (8), 2422-2428.
17. Axelrod, D., *Method. Cell Biol.* **1989,** *30*, 245-270.
18. Axelrod, D., *Method. Cell Biol.* **2008,** *89*, 169-221.
19. Bartko, A. P.; Dickson, R. M., *J. Phys. Chem. B* **1999,** *103* (51), 11237-11241.
20. Bartko, A. P.; Dickson, R. M., *J. Phys. Chem. B* **1999,** *103* (16), 3053-3056.
21. Forkey, J. N.; Quinlan, M. E.; Goldman, Y. E., *Biophys. J.* **2005,** *89* (2), 1261-1271.
22. Patra, D.; Gregor, I.; Enderlein, J., *J. Phys. Chem. A* **2004,** *108* (33), 6836-6841.
23. Toprak, E.; Enderlein, J.; Syed, S.; McKinney, S. A.; Petschek, R. G.; Ha, T.; Goldman, Y. E.; Selvin, P. R., *P. Natl. Acad. Sci. USA* **2006,** *103* (17), 6495-6499.
24. Langmuir, I., *J. Am. Chem. Soc.* **1917,** *39*, 1848-1906.
25. Blodgett, K. B., *J. Am. Chem. Soc.* **1935,** *57* (1), 1007-1022.
26. Juhasz, J.; Davis, J. H.; Sharom, F. J., *Biochem. J.* **2010,** *430*, 415-423.

Chapter 5: Exploring the Effects of Sterols in Model Lipid Membranes using Single-Molecule Orientations

As mentioned in Chapter 4, a well-characterized test system is needed for properly examining and developing the single-molecule orientation approach. LB films of lipids provide an ideal platform for these studies since these systems have been thoroughly characterized and enable a high degree of systematic control over the molecular level structure. This chapter will discuss the motivation for utilizing a simplified model system in single-molecule fluorescence measurements, and how these measurements can be used to characterize the molecular structure present in model membrane systems. The effects of thermodynamic properties and additives are also used to compare monolayer and bilayer membrane systems using this approach.

5.1 Introduction

The complexity of biological membranes often makes direct studies of membrane properties difficult in intact tissues. The number and distribution of membrane components is highly variable and not easily controlled, complicating both the experimental approaches and interpretation of the resulting data. These difficulties have led to the development of model membrane systems, using both lipid monolayers and bilayers. These simplified models provide much more control over parameters such as membrane composition, but questions remain regarding their utility in understanding the vastly more complex natural biomembranes. Regardless, it is clear that these model systems have been invaluable for understanding, for instance, the phase behavior of lipid films and the physical effects of membrane additives such as cholesterol.

Bilayers formed from vesicle fusion onto substrates provide a conceptually appealing mimic of biomembranes while monolayers fabricated using the Langmuir-Blodgett (LB) technique offer the advantage that the surface pressure can be precisely controlled. In the LB

technique, the propensity of lipids to spread at the air-water interface is countered by an external mechanical pressure provided by a moving barrier. This enables the precise measurement and control over film lateral surface pressure (Π) which is the first derivative of free energy with respect to surface area. These measurements, therefore, provide a direct link between surface pressure and film thermodynamics which can be studied over a wide range of pressures, temperatures and film compositions.

For model bilayers, surface pressure is not well defined at equilibrium, since the films exist in a tension free state. For bilayers it is the lateral compressibility that is the useful parameter when discussing such properties as protein insertion or conformational changes. In monolayers, lateral compressibility can be directly measured from the slope of the pressure-area isotherm. This illustrates the utility of comparative studies done with both monolayers and bilayers. While monolayers often provide a more direct measure of quantities such as surface pressure and compressibility, bilayers provide a more faithful representation of biological membranes. This necessitates a need for measurable parameters which establish corresponding states between monolayers and bilayers.

While surface pressure in monolayers is a thermodynamically precise quantity, for bilayers a more relaxed quantity, termed the equivalent surface pressure, is often discussed. The equivalent surface pressure is the collective interactions that balance the cohesive bilayer pressure that arises from the hydrophobic interactions between the lipid acyl chains and water.[3] Quantifying an equivalent surface pressure in bilayers is obviously important for studies comparing properties of monolayers and bilayers and for establishing conditions under which monolayers can be used as bilayer mimics.

While direct measures of surface pressure in bilayers is not possible, the monolayer-bilayer equivalence pressure can be established through indirect studies comparing their

properties. For example, the partitioning of dibucaine, a local anesthetic, with monolayers of 1-palmitoyl-2-oleoyl phosphatidylcholine (POPC) at a surface pressure of 30.7-32.5 mN/m closely matched that in bilayers, suggesting similar surface pressures.[7] A similar study found that the partitioning of myristic acid into phosphatidylcholine bilayers closely matched that of monolayers compressed to a surface pressure of 35 mN/m.[1] Finally, the partitioning of the small 22 residue peptide, phosphotransferase glucitol permease, into POPC vesicles was found to be similar to POPC monolayers compressed to a surface pressure of 32 mN/m.[5] Assuming that the insertion of species is similar in monolayers and bilayers, these partitioning studies suggest that bilayers have an equivalent surface pressure of ~30-35 mN/m.

Equilibrium spreading experiments have also been used to estimate the bilayer equivalence pressure. Vesicles in a subphase are allowed to form bilayers across an opening separating two solutions and form a monolayer at the air/subphase interface. When these films reach equilibrium, measurement of the surface pressure at the air/subphase interface yields insight into the equivalent surface pressure of the suspended bilayer. Using vesicles from the *Torpedo* electroplax, an equivalence bilayer pressure was estimated to be ~34 mN/m using this technique.[6]

Previous studies in our group have shown out-of-focus single-molecule fluorescence measurements can be used to quantify the orientation of single dye molecules doped into lipid monolayers of DPPC.[11] Several groups have shown that polarized total internal reflection fluorescence microscopy (PTIRF-M) can be used to quantify the three-dimensional orientation of dye molecules in samples when spherical aberrations are introduced into the optics train through defocusing.[12-16] Using this approach, it was shown that the orientation of fluorescent lipid analogs doped into LB monolayers of DPPC could be used to track membrane order. Here these measurements are extended to fully explore the single-molecule orientation of BODIPY-PC

doped in DPPC monolayers as a function of surface pressure. Results from these measurements are used to find the equivalent surface pressure in DPPC bilayers formed through vesicle fusion onto a substrate. Single-molecule orientation measurements suggest that supported DPPC bilayers formed from both giant unilamellar vesicles (GUVs) and small unilamellar vesicles (SUVs) exhibit equivalent surface pressures of ~23 mN/m. This value is somewhat smaller than the currently accepted value of ~30 to 35 mN/m.[1-7]

Having established a corresponding surface pressure between monolayers and bilayers of DPPC, single-molecule orientation measurements are used to compare the effects of biologically relevant sterols added to the lipid films. Cholesterol is an essential component of biological membranes that contributes up to 40-50 mol % of the plasma membrane in eukaryotic cells and leads to a well known condensing effect when added to membranes containing saturated lipids such as DPPC.[17-19] In general, this condensation of the lipids leads to an increase in lateral packing and ordering of the hydrocarbon chains, a reduction in the area per molecule, decreased membrane permeability, and an increase in membrane mechanical strength.[17-21]

Ergosterol is a plant sterol similar in structure to cholesterol which differs by an extra double bond in the acyl chain. The effects of ergosterol on membrane properties is less clear with some studies suggesting it has a greater condensing effect than cholesterol while others suggest the opposite.[8,22,23] Finally lanosterol, a biological precursor to cholesterol, is known to induce little condensing effects when added to model membranes.[8,22,23] These sterols therefore demonstrate a range of effects on membrane properties that are explored at the single-molecule level using defocused PTIRF-M measurements.

5.2 Materials and Methods

1,2-dipalmitoyl-*sn*-glycero-3-phosphocholine (DPPC) (Avanti Polar Lipids, Alabaster, AL), cholesterol (>99%), ergosterol (≥98), and lanosterol (≥97%) (Sigma Aldrich, St Louis, MO) were obtained and used without further purification. The fluorescent lipid analog 2-(5-butyl-4,4-difluoro-4-bora-3a,4a-diaza-*s*-indacene-3-nonanoyl)-1-hexadecanoyl-*sn*-glycero-3-phosphocholine (β-C_4-BODIPY 500/510 C_9 HPC) (BODIPY-PC) (Invitrogen Corporation, Carlsbad, CA, B3794) was doped into lipid films at a concentration of $\sim 10^{-8}$ mol %.

5.2.1 Langmuir-Blodgett Preparation of Lipid Monolayers

For the preparation of monolayers, DPPC was dissolved in chloroform (1mg/ml stock solutions) and the desired amount of sterol was added. The solutions were doped with $\sim 10^{-8}$ mol % BODIPY-PC reporter dye, and dispersed onto a subphase of ultra-pure water (18 MΩ) in a Langmuir-Blodgett trough (Type 611, Nima Technology, Coventry, England). Once dispersed on the subphase, the chloroform was allowed to evaporate for 15 minutes. DPPC monolayers were compressed at a speed of 100 cm^2/min to approximately 45 mN/m and then expanded at a speed of 80 cm^2/min. The compression/expansion cycles were repeated twice to anneal the monolayer. The monolayer film was then compressed to the target pressure, held for approximately 15-20 minutes, and then transferred in a headgroup down geometry onto a Piranha cleaned glass substrate at a dipping speed of 25 mm/min. All monolayers were prepared at a temperature of $\sim 21^{o}$C.

5.2.2 DPPC Bilayer Formation Through Vesicle Fusion

For the preparation of supported DPPC bilayers, the appropriate mol% of each sterol was added into a 5mg/mL chloroform solution of DPPC. After doping each solution with $\sim 10^{-8}$ mol % BODIPY-PC reporter dye, 380 μL of DPPC / sterol solution was added to a separate vial, evaporated to dryness with nitrogen, and placed under vacuum for ~1hr to remove residual

solvent. The DPPC/sterol mixtures were reconstituted in a buffer solution containing 20 mM HEPES, 100 mM NaCl, and 0.02 wt % NaN_3 adjusted to neutral pH. The vials were capped and incubated at ~60 ^{o}C for 1hr to hydrate the phospholipids. The suspensions were vortexed and sonicated to clarity, yielding small unilamellar vesicles (SUVs). The SUV suspensions were incubated in PDMS wells on Piranha cleaned glass for 30 min at 60 ^{o}C. The wells were thoroughly washed with nanopure water to remove unruptured vesicles, and the excess water was removed immediately before imaging.

Supported lipid bilayers were also formed using giant unilamellar vesicles (GUVs) prepared by electroformation. Briefly, 50 µL of a 5 mg/mL chloroform solution of DPPC/sterol with ~10^{-8} mol% BODIPY-PC reporter dye was deposited on two microscope slides coated with indium tin oxide (ITO). The solution was dried onto the slides under vacuum for ~1 hr. The coated slides were rehydrated with ~1 mL of 18 MΩ water and sandwiched together with a 1.5 mm thick PDMS gasket. The slide assembly was placed on a temperature-controlled stage set to 50 °C and the lipids were allowed to hydrate for ~20 minutes. Following hydration, a function generator was used to apply a 10 Hz, 1 V sine wave across the ITO coated slides for ~3hr to produce giant unilamellar vesicles. The GUVs were detached from the surface by reducing the frequency to 1Hz for ~30 min, after which the suspension was isolated.

5.2.3 Imaging Approach

All films were imaged using a total internal reflection fluorescence microscope (TIRF-M) (Olympus IX71, Center Valley, PA) equipped with a 100x objective (1.45 NA achromat). The 514 nm line from an argon ion laser (Coherent Innova 70 Spectrum, Santa Clara, CA) was directed through half-wave and quarter-wave plates (Newport, Irvine, CA) to generate p-polarized excitation. Excitation was directed through the objective and fluorescence collected in an epifluorescence geometry with the optics defocused ~500 nm. The fluorescence was filtered

with a combination of a dichroic mirror and long pass filters (Chroma, Rockingham, VT) and imaged onto a CCD camera (Cascade 650, Roper Scientific, Tucson, AR). Image collection was controlled with Slidebook software (Version 4.2, Intelligent Imaging Innovations, Denver, CO) and analyzed using MatLab software (Natick, MA).

5.3 Results and Discussion

Initial work in our group has shown that single-molecule fluorescence measurements using PTIRF-M can reveal insight into membrane structure at the molecular level.[11] Here we expand those initial studies to characterize the equivalent surface pressure in bilayers and compare both monolayers and bilayers doped with the biologically important sterols cholesterol, ergosterol, and lanosterol. Figure 5.3.1 shows the structures of DPPC and the sterols studied along with the fluorescent lipid analogue, BODIPY-PC that was doped into the membranes to act as the reporter probe.

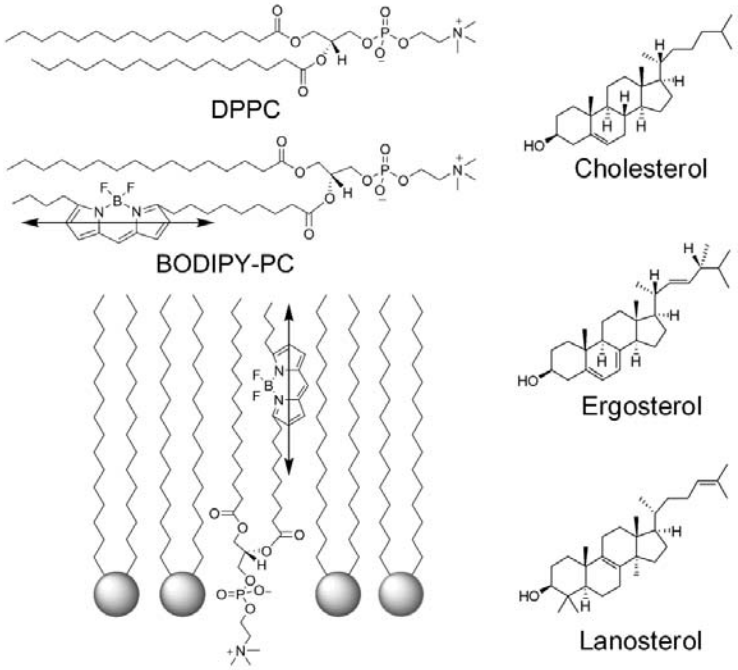

Figure 5.1: Structures of DPPC and the sterols studied in both monolayers and bilayers. Also shown is the fluorescent lipid analog BODIPY-PC along with a schematic representation of its insertion into a monolayer membrane.

Other studies have shown that unique single-molecule emission patterns are observed in slightly defocused PTIRF-M images, which reflect the orientation of the dye in the sample.[12-16,24] Analysis of the emission patterns, therefore, enables the three-dimensional orientation of each dye molecule doped into the lipid film to be characterized. BODIPY-PC was chosen as the fluorescent reporter dye due to its placement of the fluorophore in the tailgroup, which has been shown to be sensitive to membrane order.[11] The absorption and emission dipoles of BODIPY-PC lie along the long axis of the chromophore with ~13˚ between the two.[25]

5.3.1 Surface Pressure Studies

Figure 5.2 shows representative single-molecule emission images of ~10^{-8} mol% BODIPY-PC doped into DPPC monolayers, which were transferred onto glass substrates at surface pressures of 3 mN/m, 25mN/m, and 40 mN/m using the Langmuir-Blodgett (LB) technique. As the surface pressure of the LB monolayers is increased, an evolution towards donut-shaped emission features is observed which arise from emission dipoles oriented normal to the membrane plane. As shown by others, these emission patterns can be modeled to quantitatively extract the three-dimensional orientation of the emission dipoles in the sample.[12-16] Using this approach, each emission feature is analyzed to extract the tilt angle (Φ) away from the membrane normal. Figure 5.2 shows representative tilt angle histograms for monolayers prepared at five different surface pressures along with the number of molecules analyzed at each pressure.

At a surface pressure of 3 mN/m, the single-molecule tilt histogram reveals most of the dye probes are oriented in the plane of the film (≥81˚), reflecting the disorder in the DPPC monolayer at low surface pressures. This is seen in the corresponding emission image which contains mostly single-molecule features consisting of bright spots surrounded by wings that are characteristic of molecules oriented with large tilt angles. The tilt angle histogram, therefore,

reveals a large population of emission dipoles oriented in the plane of the film with a smaller population spread through the remaining angles. The average tilt angle calculated from the histogram is 67.4 ± 5˚ (N = 711) at a surface pressure of 3 mN/m.

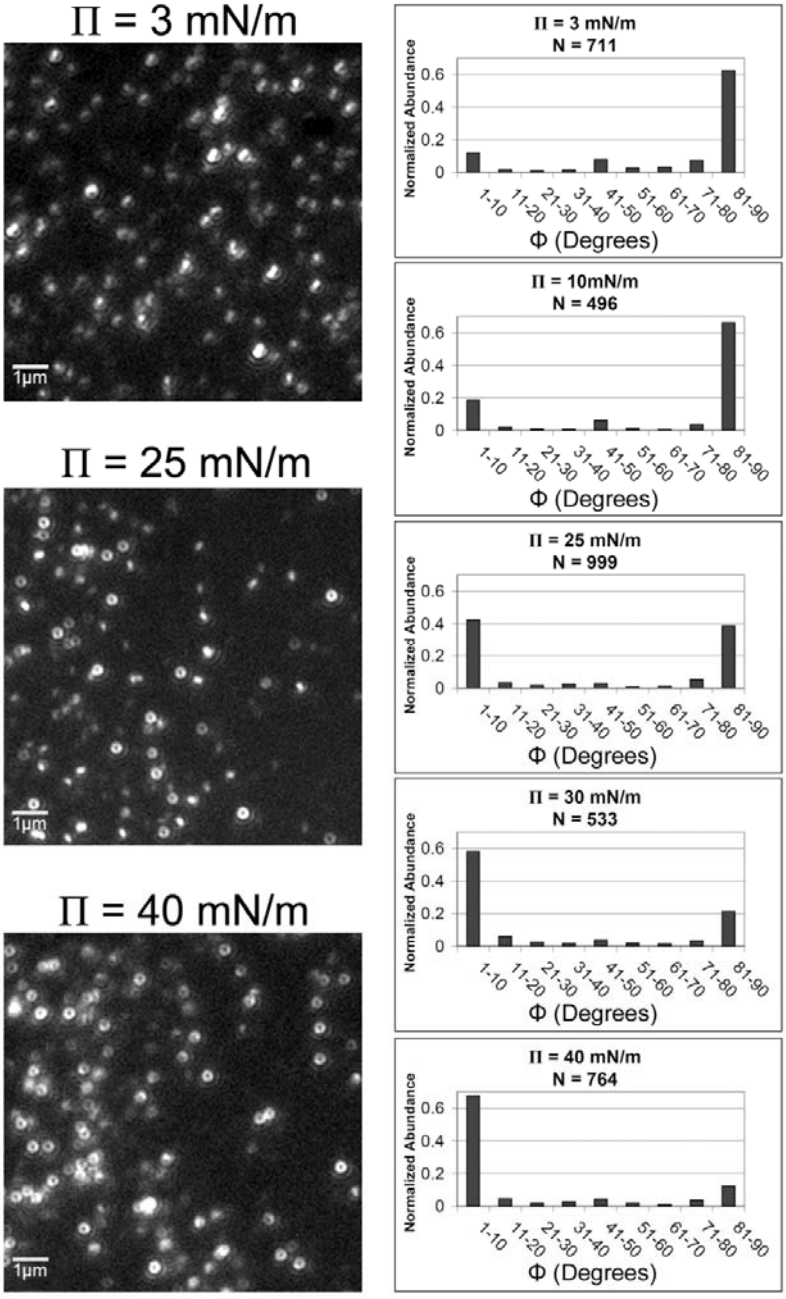

Figure 5.2: Representative single molecule fluorescence images of BODIPY-PC reporter molecules doped into DPPC monolayers at left, with their corresponding orientation histograms shown at right.

At the other surface pressure extreme, the single-molecule emission image for DPPC transferred at 40 mN/m reveals a large population of donut-like features reflecting emission dipoles that are oriented normal to the membrane surface. The corresponding tilt angle histogram shown in Fig. 5.2 reveals that most of the dye population have tilt angles ≤10˚ at this elevated surface pressure. This reflects the increased membrane order in the lipid monolayer at 40 mN/m, which reduces the average tilt angle to 22.4 ± 5˚ (N = 764).

At intermediate surface pressures, Fig. 5.2 reveals bimodal tilt distributions with the majority of molecules adopting orientations either normal or parallel to the membrane plane, with fewer adopting intermediate tilts. The bimodal distribution in tilt angles reflects BODIPY-PC partitioning into the lipid phases in the DPPC monolayer. At intermediate surface pressures, DPPC monolayers partition into domains of less ordered liquid-expanded (LE) phase and more ordered liquid-condensed (LC) phase leading to the observed bimodal tilt distribution.

As shown in Fig. 5.2 there is a steady rise in the population of molecules oriented normal to the DPPC monolayer as the surface pressure of the film is increased. A plot of the population of molecules oriented normal to the surface ($\Phi \leq 10^{\circ}$) as a function of surface pressure is shown in Fig. 3. DPPC monolayers were transferred onto glass substrates at eight different surface pressures between 3 mN/m and 45 mN/m with the results plotted in Fig. 5.3. The linear dependence with surface pressure provides a convenient marker of membrane order and a useful calibration for characterizing the surface pressure in bilayers. Also shown in Fig. 5.3 is the percent LC area in the monolayers as a function of surface pressure.

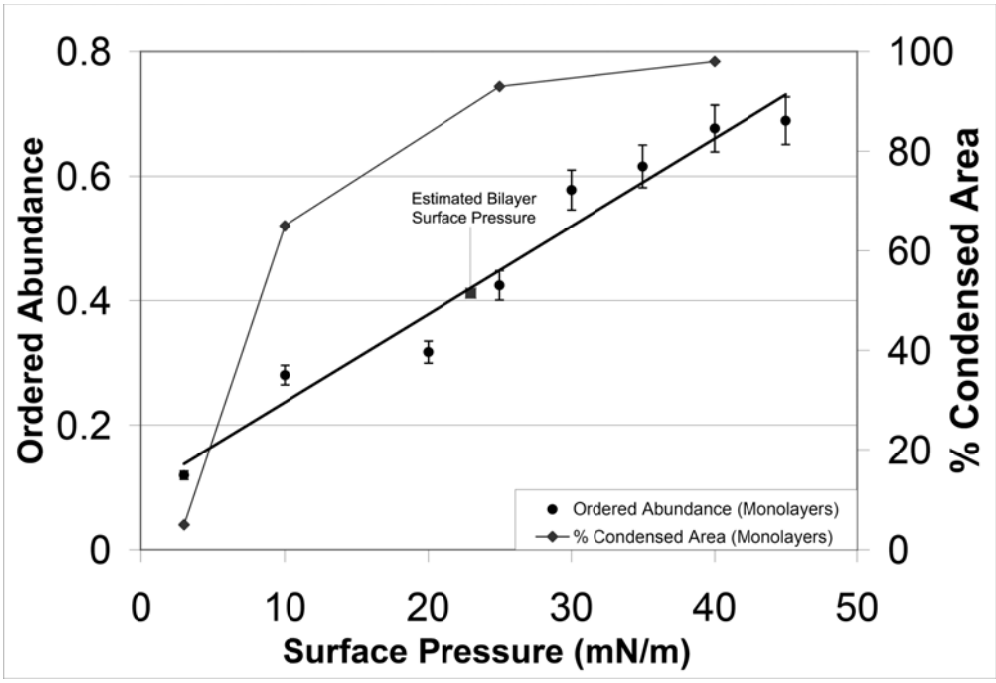

Figure 5.3: Percentage of BODIPY-PC probes oriented normal ($\Phi \leq 10^{o}$) to the membrane plane in DPPC monolayers as a function of surface pressure.

5.3.2 Determination of the Monolayer-Bilayer "Equivalence" Pressure

Supported bilayers formed from vesicle fusion onto a substrate are often used to mimic natural membranes. While bilayers provide a more realistic model of biological membranes, they enable less control than monolayers over external parameters such as surface pressure. Since bilayers are generally in a tension free state, parameters such as surface pressure are not well defined and direct comparisons with LB monolayers can become ambiguous. Determining the equivalent surface pressure of bilayers is therefore important for defining corresponding states between LB monolayers and bilayers. The linear dependence of single-molecule tilt with surface pressure shown in Fig. 5.3, therefore, provides a useful calibration for determining the equivalent surface pressure of bilayers.

Figure 5.4 (top panel) shows a defocused single-molecule PTIRF-M fluorescence image of a supported DPPC bilayer doped with $\sim 10^{-8}$ mol% BODIPY-PC. Analysis of the single-molecule emission patterns leads to the emission dipole orientations shown in the middle panel. Analysis

of 743 individual molecules from several bilayers results in the tilt angle histogram shown in the bottom panel of Fig. 5.4. As observed with DPPC monolayers formed with the LB technique, there is a bimodal distribution in the tilt angle histogram of the BODIPY-PC doped into the DPPC bilayers. From the histogram, the average tilt angle for the BODIPY-PC dye doped into DPPC bilayers is measured to be 45.2˚ ± 5˚.

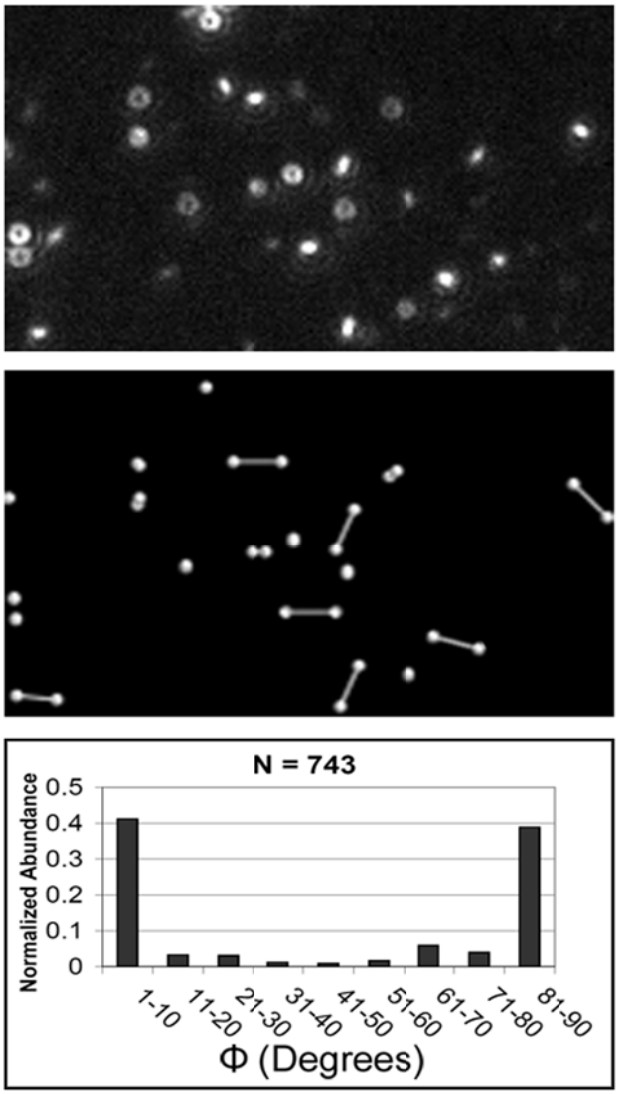

Figure 5.4: Representative single-molecule fluorescence image of a DPPC bilayer doped with ~10^{-8} mol% BODIPY-PC. Analysis of the single-molecule emission patterns results in the orientations shown schematically in the middle panel. Analysis of emission features from several bilayers results in the tilt angle histogram shown in the bottom panel.

The tilt angle histogram measured for supported bilayers in Fig. 5.4 can now be used to estimate the equivalence surface pressure of the bilayer using the data plotted for monolayers in Fig. 5.3. From the histogram in Fig. 5.4, the percentage of emission dipoles oriented normal to the membrane plane ($\Phi \leq 10^{\circ}$) in supported bilayers of DPPC is 41%. This point is shown in Fig. 5.3 and translates into an equivalent surface pressure of ~23 mN/m. Single-molecule measurements on supported bilayers formed from both small unilamellar vesicles (SUV's) and giant unilamellar vesicles (GUV's) resulted in statistically identical results. This equivalent surface pressure is somewhat smaller than the values obtained from other experiments (~30-35 mN/m).[1-7]

5.3.3 Additive Effects on Membrane Structure

Having established the equivalent surface pressure for supported DPPC bilayers, the influence of sterol additives were compared in both LB monolayers transferred at 23 mN/m and DPPC bilayers. Cholesterol is widely distributed in biological membranes and exerts a well-known condensing effect.[17-20,26,27] The profound influence of cholesterol on membrane properties can be traced to its structure, which is shown in Fig. 5.1. Cholesterol consists of a fused ring structure that is responsible for its rigid, planar geometry. There is a single hydroxyl group located at the C_3 position and an iso-octyl acyl chain extending from the opposite side of the ring at position C_{17}. Two methyl groups extend from the same side of the ring structure as the acyl chain, forming a β-configuration. When cholesterol inserts into lipid monolayers and bilayers, it orients with its polar hydroxyl group lying towards the hydrophilic phospholipid headgroups and the hydrophobic ring structure aligned along the lipid acyl chains. The cohesive interactions between cholesterol and the lipid acyl chains are strongly linked with the degree of lipid saturation, making these interactions particularly important for lipids such as DPPC.

Figure 5.5 compares the effects of cholesterol on monolayers and bilayers of DPPC as probed through single-molecule orientation measurements. LB monolayers were transferred onto a glass substrate at a surface pressure of ~23 mN/m, which corresponds to the equivalent surface pressure of pure DPPC bilayers measured previously. Shown in Fig. 5.5 are the tilt angle histograms for monolayers and bilayers incorporating 0 mol%, 5 mol%, 10 mol%, and 33 mol% cholesterol. With no added cholesterol, the tilt angle histograms for both monolayers and bilayers are bimodal and closely agree with one another, as expected from their corresponding surface pressures. The population of BODIPY-PC molecules oriented normal to the film plane (Φ ≤10˚) is approximately 42% and 41% for the monolayers and bilayers, respectively.

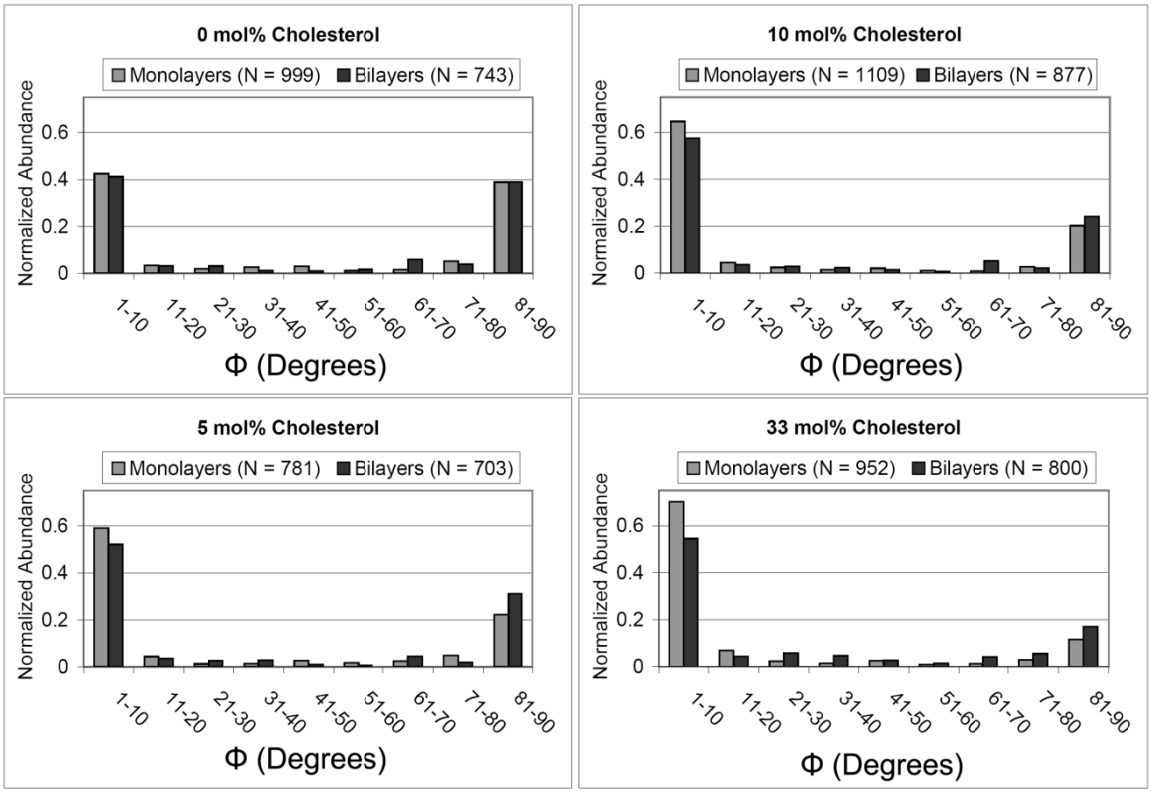

Figure 5.5: Comparison of tilt angle (Φ) histograms for DPPC monolayers (deposited at ~23 mN/m) and bilayers doped with increasing concentrations of cholesterol.

As shown in Fig. 5.5, the addition of even small amounts of cholesterol (5 mol%) leads to a dramatic shift in the single-molecule tilt histograms. Upon the addition of 5 mol% cholesterol,

the ordered abundance (Φ ≤10˚) increases from 42% to 59% in monolayers and from 41% to 52% in bilayers. The single-molecule tilt histograms summarized in Fig. 5.5 reveal a steady increase in the ordering of the acyl chains with increasing cholesterol content for both monolayers and bilayers. As cholesterol is increased, a steady rise in the number of BODIPY-PC molecules oriented normal to the plane (Φ ≤ 10˚) is observed with an associated drop in the population oriented in the membrane plane (Φ ≥ 81˚).

Ergosterol and lanosterol provide useful structural analogs of cholesterol that can help clarify the unique role of cholesterol in modifying membrane properties. Ergosterol is generally found in the membranes of plants, while lanosterol predates cholesterol in the evolutionary pathway. As shown in Fig. 5.1, ergosterol is very similar to cholesterol and only differs slightly with a carbon-carbon double bond in the second steroid ring, an unsaturated side chain, and methylation at position C_{24}. Both cholesterol and ergosterol lead to condensing effects in membranes, although there is some disagreement regarding which has a larger effect.[8,22,23] Lanosterol, on the other hand, has three extra methyl groups on the α-surface of the ring system that are believed to increase the steric costs associated with membrane insertion (Fig. 5.1). Although lanosterol still has a condensing effect on membranes, studies agree that the effect is much smaller than that of either cholesterol or ergosterol.[8,22,23]

Figure 5.6 summarizes the results from defocused single-molecule PTIRF-M studies on monolayers and bilayers incorporating cholesterol, ergosterol, and lanosterol as a function of sterol concentration. Sterol concentrations of 0 mol%, 5 mol%, 10 mol%, and 33 mol% sterol are compared. Once again, LB monolayers were transferred at a surface pressure of ~23 mN/m to match the bilayer equivalent surface pressure determined earlier. The results are summarized in Fig. 5.6 which plots the percentage of BODIPY-PC molecules oriented normal to the membrane plane (Φ ≤ 10˚) as a function of sterol concentration. The plot in Fig. 5.6-A shows

that for both monolayers and bilayers, the population of dyes ordered normal to the membrane increases rapidly with cholesterol concentration and levels off at higher concentrations.

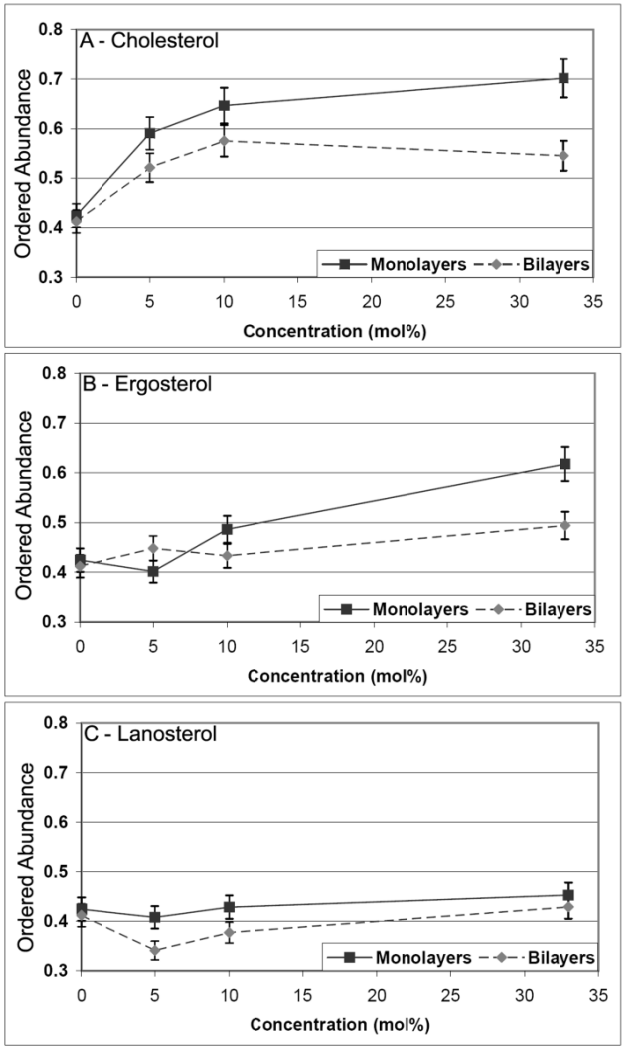

Figure 5.6: A comparison of the effects of **(A)** cholesterol, **(B)** ergosterol, and **(C)** lanosterol on the ordered abundance ($\Phi \leq 10^{o}$) of BODIPY-PC reporter molecules doped into DPPC monolayers and bilayers.

The results for ergosterol, shown in Fig. 5.6-B, indicate a more subtle increase in membrane order with sterol concentration. Both monolayers and bilayers reveal an increase in order in the single-molecule PTIRF-M images, with monolayers being slightly more sensitive to ergosterol addition. Unlike the results for cholesterol, little effect on membrane ordering is

observed at low ergosterol concentrations and only becomes significant in the single-molecule results at higher ergosterol concentration. For lanosterol, single-molecule orientation measurements reveal little influence on membrane ordering. Figure 5.6-C shows that the percentage of single-molecules oriented normal to the plane remains essentially constant for both monolayers and bilayers throughout the concentrations studied.

The bimodal distribution of single-molecule orientations observed in DPPC bilayers suggest coexisting lipid phases are present in both pure DPPC bilayers and those in which cholesterol has been added. Bulk fluorescence measurements on similar films find no evidence for coexisting domains on the sub-micron length scale.[28] However, both energy transfer measurements and some NMR studies have found evidence for coexisting domains in these systems.[9,29-31] These differences are often ascribed to the different length/time scales that are probed by the different techniques. The results shown here suggest single-molecule orientation measurements can provide a unique view of model lipid film properties that compliments other well established approaches.

The influence of cholesterol on high melting temperature lipids such as DPPC has been widely studied, yet a clear picture of its effects has yet to emerge. Different phase diagrams have been constructed based on results using different techniques, but most agree that these mixed bilayers can exist in the gel phase (S_o), liquid-crystalline (L_α), and liquid-ordered (L_o) states. The latter is a cholesterol induced state whose name summarizes the combination of structural order with liquid-like dynamics in this state. The well-known condensing effects of cholesterol lead to extended acyl chains in this state, while translational diffusion and rotational motion remain liquid-like.[17-21]

5.3.4 Order Parameter Measurements

The single-molecule orientation measurements can be compared with previous bulk measures of membrane structure through the use of the order parameter, S. The order parameter is defined as

$$S = \tfrac{1}{2}\,(3\langle\cos^2\theta\rangle - 1)$$

where θ is the angle with respect to the membrane normal. Order parameters have been characterized in DPPC films as a function of cholesterol using techniques such as nuclear magnetic resonance (NMR), fluorescence anisotropy, and X-ray scattering.[8-10] The trends from these studies are summarized in Figure 5.7 along with the results from our single-molecule measurements.

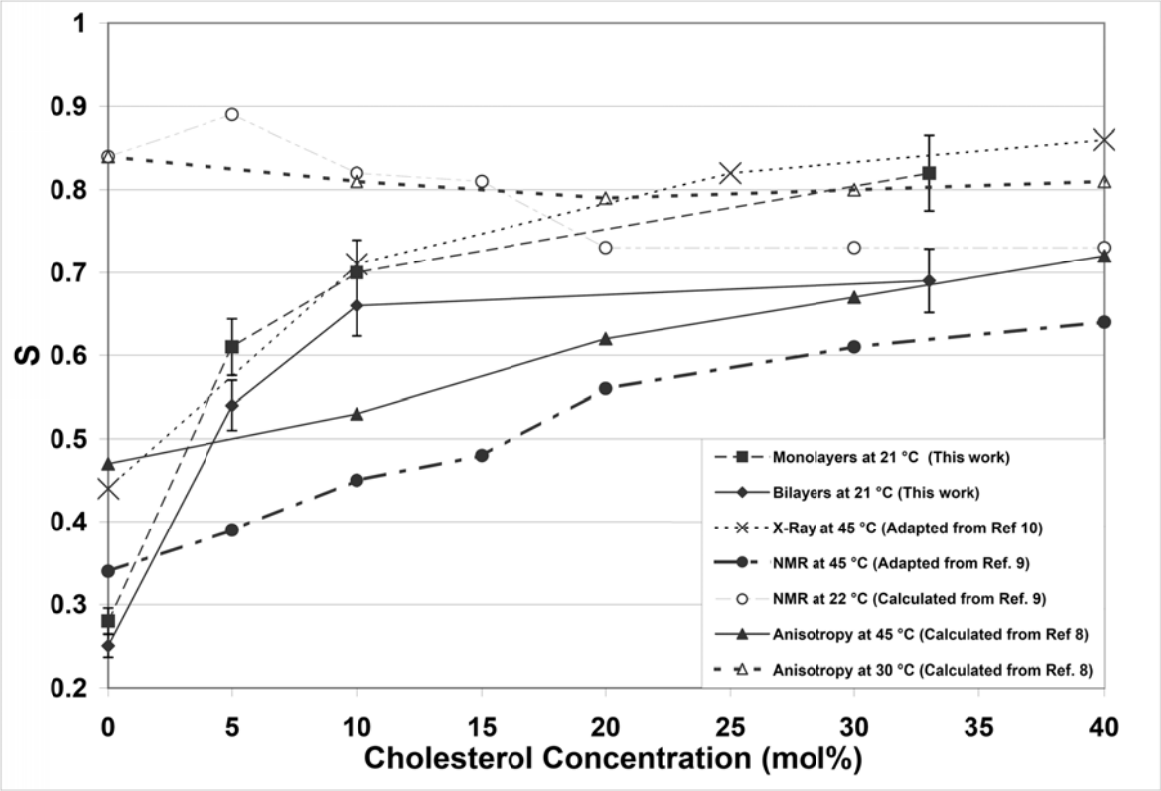

Figure 5.7: The order parameter, S, calculated from the average tilt angle found from the single-molecule tilt histograms is plotted as a function of cholesterol concentration. Also shown are trends in S found previously using NMR, fluorescence anisotropy, and X-ray measurements below and above the transition temperature for DPPC.

There is a striking similarity in the trends that are observed from our room temperature single-molecule studies and previous studies done above the transition temperature. Order parameters calculated using the average tilt angle from the single-molecule histograms show a sharp rise in S at low cholesterol concentration that levels off at higher concentrations. As shown in Fig. 5.7, this agrees closely with S values calculated from X-ray studies done at 45 ^{o}C.[10] Similar trends are also observed in the NMR and fluorescence studies carried out at 45 ^{o}C.

Also plotted in Fig. 5.7 are the results from NMR and fluorescence anisotropy studies done at room temperature that reveal high initial S values that decrease with cholesterol content.[8,9] These changes do not track the changes we find in the single-molecule measurements which can be understood by recognizing that different techniques measure different aspects of membrane order. For example, S values derived from the NMR experiments provide a measure of the orientational freedom around the acyl chain axis. These measurements, therefore, provide insight into membrane packing. At room temperature, below the melting temperature for DPPC, NMR measurements of pure DPPC films yield high values for the order parameter. This results from the small degree of rotational freedom around the acyl chains and the high degree of lateral packing in the S_o phase. Upon the addition of cholesterol, however, the S values decrease due to the disruption of the gel state packing and increase in acyl chain freedom. Additional cholesterol further disrupts the lateral packing of the film and leads to the formation of the L_o phase, which has a greater degree of rotational freedom and thus a smaller S as compared to the gel phase.

Above the melting temperature, NMR studies of pure DPPC films in the fluid state yield S values that are small. The low S values arise from the increased freedom around the disordered acyl chains in this state. The addition of cholesterol, which has a condensing effect on DPPC, therefore, increases the order parameter as the L_o phase is formed. This transition is

accompanied by a gel-like lateral packing with diffusional characteristics similar to the fluid phase.

For the single-molecule measurements summarized here at room temperature, the acyl chains in pure DPPC films have a high lateral packing and large tilt angles with respect to the membrane normal which leads to the low calculated S values. The addition of cholesterol, which induces L_o phase formation, increases acyl chain order which is reflected in the PTIRF-M images as an increase in donut-like single-molecule emission features. This results in the large increase in S values calculated from the single-molecule measurements as cholesterol is increased. Since the NMR measurements track the lateral packing and rotational freedom of the acyl chains and the single-molecule measurements quantify the orientation of the acyl chains with respect to the membrane normal, the differences observed at room temperature in Fig. 5.7 are expected. At elevated temperature, however, the onset of the L_o phase increases lateral packing and decreases acyl chain tilt with respect to the membrane normal. This explains why the room temperature single-molecule measurements closely agree with previous studies done at 45 ^{o}C. Therefore, despite the differences in temperature between these studies, Fig. 5.7 reveals very good agreement between the single-molecule results and bulk measures of cholesterol added to DPPC membranes.

While the average single-molecule orientations leads to agreement with previous studies characterizing S in model mixed membranes of DPPC and cholesterol, the bimodal distribution observed illustrates the detailed information available from measuring the entire orientation distribution. Using single-molecules as probes of lipid environments can complement other more established techniques and provides a new tool for understanding these complicated systems at the molecular level.

5.4 Conclusions

Single-molecule fluorescence measurements taken using out-of-focus PTIRF-M are used to characterize the three-dimensional orientation of single BODIPY-PC dye molecules doped into model films of DPPC. For LB monolayers of DPPC, characterization of single-molecule orientation histograms as a function of surface pressure reveals an evolution in membrane order. At all surface pressures studied, a bimodal orientation histogram is observed which reflects the coexisting LE and LC phases present in the monolayer. There is a linear dependence in the number of BODIPY-PC molecules with transition dipoles oriented normal to the surface with surface pressure which is used to find the equivalent surface pressure in supported bilayers. Comparison of the single-molecule orientation histogram from DPPC bilayers with the results from the LB monolayers suggests an equivalent surface pressure of ~23 mN/m for bilayers. This is somewhat lower than the currently accepted value of ~30-35 mN/m.[1-4,6,7]

With the equivalent surface pressure for bilayers established, single-molecule studies comparing the effects of cholesterol, ergosterol, and lanosterol on membrane properties are compared between DPPC bilayers and LB monolayers transferred at ~23 mN/m. Single-molecule orientation as a function of sterol content tracked closely between monolayers and bilayers. Cholesterol had the largest effect on membrane order, increasing the number of BODIPY-PC molecules oriented normal to the surface even at low cholesterol content. Lanosterol had essentially no effect on the single-molecule orientations while ergosterol did affect orientations, but to a lesser extent than cholesterol. Using the average orientation from the histograms as a function of cholesterol content, the order parameter S was calculated and compared with previous NMR and X-ray studies.[9,10] Close agreement is observed between the room temperature single-molecule results and previous bulk measures of membrane order done at higher temperatures.

These studies show that single-molecule fluorescence orientation measurements can be used to track the molecular level structure in model membrane systems. These studies, however, were all performed on dry samples that were exposed to the atmosphere. In order to further explore the ability of this single-molecule method to examine model systems approaching aqueous conditions, Chapter 6 is centered on the roles that hydration and the underlying substrate play in affecting the structure and dynamics of model membrane systems.

References

1. Boguslavsky, V.; Rebecchi, M.; Morris, A. J.; Jhon, D. Y.; Rhee, S. G.; Mclaughlin, S. *Biochemistry* **1994**, *33*, 3032-3037.
2. Gershfeld, N. L.; Tajima, K. *Nature* **1979**, *279*, 708-709.
3. Marsh, D. *Biochim. Biophys. Acta* **1996**, *1286*, 183-223.
4. Miller, C. E.; Majewski, J.; Watkins, E. B.; Mulder, D. J.; Gog, T.; Kuhl, T. L. *Phys. Rev. Lett.* **2008**, *100*, 058103.
5. Portlock, S. H.; Lee, Y.; Tomich, J. M.; Tamm, L. K. *J. Biol. Chem.* **1992**, *267*, 11017-11022.
6. Schindler, H.; Quast, U. *Proc. Natl. Acad. Sci.* **1980**, *77*, 3052-3056.
7. Seelig, A. *Biochim. Biophys. Acta* **1987**, *899*, 196-204.
8. Bernsdorff, C.; Winter, R. *J. Phys. Chem. B* **2003**, *107*, 10658-10664.
9. Scheidt, H. A.; Huster, D.; Gawrisch, K. *Biophys. J.* **2005**, *89*, 2504-2512.
10. Mills, T. T.; Toombes, G. E. S.; Tristram-Nagle, S.; Smilgies, D. M.; Feigenson, G. W.; Nagle, J. F. *Biophys. J.* **2008**, *95*, 669-681.
11. Livanec, P. W.; Dunn, R. C. *Langmuir* **2008**, *24*, 14066-14073.
12. Bartko, A. P.; Dickson, R. M. *J. Phys. Chem. B* **1999**, *103*, 11237-11241.
13. Bartko, A. P.; Dickson, R. M. *J. Phys. Chem. B* **1999**, *103*, 3053-3056.
14. Forkey, J. N.; Quinlan, M. E.; Goldman, Y. E. *Biophys. J.* **2005**, *89*, 1261-1271.
15. Patra, D.; Gregor, I.; Enderlein, J. *J. Phys. Chem. A* **2004**, *108*, 6836-6841.
16. Toprak, E.; Enderlein, J.; Syed, S.; McKinney, S. A.; Petschek, R. G.; Ha, T.; Goldman, Y. E.; Selvin, P. R. *Proc. Natl. Acad. Sci.* **2006**, *103*, 6495-6499.
17. Silvius, J. R. *Biochim. Biophys. Acta* **2003**, *1610*, 174-183.
18. Yeagle, P. L. The Roles of Cholesterol in the Biology of Cells. In *The Structure of Biological Membranes*; 2nd ed.; CRC Press LLC, 2005.
19. Mouritsen, O. G.; Zuckermann, M. J. *Lipids* **2004**, *39*, 1101-1113.
20. Ohvo-Rekila, H.; Ramstedt, B.; Leppimaki, P.; Slotte, J. P. *Prog. Lipid Res.* **2002**, *41*, 66-97.
21. Quinn, P. J.; Wolf, C. *BBA-Biomembranes* **2009**, *1788*, 33-46.
22. Cournia, Z.; Ullmann, G. M.; Smith, J. C. *J. Phys. Chem. B* **2007**, *111*, 1786-1801.
23. Sabatini, K.; Mattila, J. P.; Kinnunen, P. K. J. *Biophys. J.* **2008**, *95*, 2340-2355.
24. Hellen, E. H.; Axelrod, D. *J. Opt. Soc. Am. B.* **1987**, *4*, 337-350.
25. Karolin, J.; Johansson, L. B. A.; Strandberg, L.; Ny, T. *J. Am. Chem. Soc.* **1994**, *116*, 7801-7806.
26. McMullen, T. P. W.; Lewis, R. N. A. H.; McElhaney, R. N. *Curr. Opin. Colloid Interface Sci.* **2004**, *8*, 459-468.
27. Ege, C.; Ratajczak, M. K.; Majewski, J.; Kjaer, K.; Lee, K. Y. C. *Biophys. J.* **2006**, *91*, L1-L3.
28. Keller, S. L. *J. Phys.-Condens. Mat.* **2002**, *14*, 4763-4766.
29. Brown, A. C.; Towles, K. B.; Wrenn, S. P. *Langmuir* **2007**, *23*, 11180-11187.
30. Silvius, J. R. *Biophys. J.* **2003**, *85*, 1034-1045.
31. Polozov, I. V.; Gawrisch, K. *Biophys. J.* **2006**, *90*, 2051-2061.

Chapter 6: Hydration Effects on Membrane Structure Probed by Single Molecule Orientations

Our single-molecule studies to this point have been employed on static systems in a dry atmosphere. As our future goals encompass single-molecule studies used to determine antibody orientations in a dynamic, fluid environment, it is important to explore the time-resolved capabilities of this approach and its feasibility in conditions approaching fluid environments. The following study examines the structural and dynamic effects that hydration has on model membrane films at the molecular level.

6.1 Introduction

Supported lipid monolayer and bilayer membranes have provided useful test systems to study lipid phase behavior, probe the role of membrane constituents such as cholesterol, and for the development of biosensing platforms.[1-11] Numerous techniques have been developed to create and deposit lipid films onto substrates where they are amenable for study with high resolution techniques. These studies have been largely aimed at understanding the role of lipids in biological membranes, the structures lipids form, and how different constituents interact with or insert into membrane structures.[2-3, 6-8, 12-19]

For supported lipid membranes, extensive studies have been devoted to understanding and characterizing the influence that the substrate can have on membrane properties.[20-26] These studies can take many forms but usually revolve around understanding the role that the substrate plays in influencing membrane structure, fluidity, and in modifying the activity of membrane incorporated species.[20-26] These studies are important from both fundamental and practical viewpoints. For applied applications of supported model membranes in devices such as sensor platforms, characterizing the underlying effects of the substrate on membrane stability and responsiveness is of obvious importance. For fundamental studies where supported membranes are used to mimic natural membranes, the influence of substrate and environmental condition on membrane properties must be understood to put

the results in the proper context. Factors such as ionic strength, pH, temperature, and substrate identity can all have a profound influence on membrane orientation, integrity, and fluidity.[21-22, 24, 27-28]

Previous studies have helped define the significant role that relative humidity (RH) can play in influencing the structure of supported lipid films.[20, 29-34] On the macroscopic scale, RH levels have been found to influence the lateral diffusion of supported lipid films. For example, fluorescence recovery after photobleaching (FRAP) measurements on multilayer films of egg phosphatidylcholine found an 8-fold increase in the diffusion coefficients of NBD-PE with increasing RH.[33] In general, increasing lateral diffusion with RH has also been observed for monolayer lipid films, with the extent strongly tied to the nature of the underlying support. Monolayers of DMPC and DphyPC deposited onto polysaccharide cushions exhibit greater lateral diffusion than, for example, monolayers transferred directly onto glass.[20] The emerging picture from these and other studies suggests that lateral diffusion is an activated process in which the activation energy is linked to the extent of lipid headgroup hydration level. Increasing the hydrated radius of the headgroup decreases the electrostatic interactions with the substrate, thus lowering the barrier height for lateral diffusion.

At the molecular level, spectroscopic measurements of lipid membranes have provided insight into the structural changes that accompany changes in the RH.[27, 35-40] Polarized IR studies of acyl chain tilt angle found decreasing order parameters with increasing hydration, suggesting a reorientation of the acyl chain towards the supporting surface.[27, 35-36] Similar studies on bilayer membranes using a number of lipid compositions generally found reorientation of the acyl chains with increasing RH. Raman measurements on multilamellar DMPC membranes found evidence for both small and dramatic changes in acyl chain order with increasing RH.[39-40] The small shifts in acyl chain order were assigned to reorientations of the lipids in the membrane with RH while the larger shifts were attributed to phase changes in the membrane. Differential scanning calorimetry studies have also found evidence for phase changes in supported lipid membranes with RH.[41-43] For example, the gel phase transition temperature

for DPPC has been reported to increase from ~ 41 °C in the completely hydrated state to ~102 °C in the fully dehydrated state.[42]

X-ray studies on model membranes have also found evidence for increasing acyl tilt angle with increasing RH.[28, 44-50] Several studies have shown that the tilt angle in multilayer DPPC films increases from a lower limit of 17-22° in the dehydrated state to an upper limit of ~32° in a fully hydrated membrane.[44-45, 51] Similar trends with smaller magnitudes were observed for DMPC multilayers in which tilt angles increased from 26° to 30° as the membrane was hydrated.[28] At elevated RH, water uptake by the lipid headgroups correlates with increasing tilt angles again suggesting that headgroup hydration can effect overall membrane structure.

Clearly, supported membrane systems are appreciably influenced by ambient RH and further studies are warranted to characterize its influence on membrane structure and fluidity. The recent emergence of single molecule fluorescence measurements offers a new approach for probing membrane properties at the molecular level. Single molecule fluorescence measurements can characterize the three-dimensional orientation of individual fluorescent markers doped into lipid films at trace levels.[52-61] Orientational changes of fluorescent lipid probes have been shown to be sensitive to membrane organization and have been used to characterize changes in membrane structure with surface pressure and membrane composition.[15, 62-65] The method is minimally perturbative since only trace amounts of a fluorescent lipid analog are needed and, since measurements are made on individual molecules in the sample, it does not suffer from the loss of information due to ensemble averaging. This is especially useful for model membranes which often exhibit structural heterogeneity.[1, 3-5, 7, 10, 13-14, 18-19, 66-67]

Here we use single molecule orientation measurements to characterize the response of LB films of DPPC to changes in relative humidity. Single molecule orientation measurements reveal that DPPC films transferred at both low (23 mN/m) and high (40 mN/m) surface pressures reveal changes in single

molecule orientations with RH. Comparison with films fabricated using the vesicle fusion method shows that structural changes as a function of RH more closely track changes seen in LB films transferred at 23 mN/m. Finally, single molecule orientation measurements with time reveal changes in the orientational freedom around fluorescent lipid analogs as a function of RH. These changes in orientational freedom are not associated with long range translational changes observed in bulk measures of diffusion, illustrating the complementary nature of single molecule measurements with ensemble averaged techniques.

6.2 Materials and Methods

1,2-dipalmitoyl-*sn*-glycero-3-phosphocholine (DPPC) (Avanti Polar Lipids, Alabaster, AL) was obtained and used without further purification. The fluorescent analog, 2-(5-butyl-4,4-difluoro-4-bora-3a,4a-diaza-*s*-indacene-3-nonanoyl)-1-hexadecanoyl-*sn*-glycero-3-phosphocholine (BODIPY-PC, B3794) (Invitrogen Corporation, Carlsbad, CA) was doped into the lipid films at 10^{-8} mol% concentration.

6.2.1 Bilayer Fabrication Through Vesicle Fusion

The preparation of supported lipid bilayers using vesicle fusion was carried out as described elsewhere.[15] Briefly, a 5mg/mL solution of DPPC in chloroform was doped with 10^{-8} mol% of BODIPY-PC. 380µL of this solution was placed in a separate vial and evaporated to dryness with nitrogen, after which the film was placed under vacuum for ~1hr to remove residual solvent. A 20mM HEPES, 100mM NaCl, 0.02 wt% NaN_3 buffer solution adjusted to neutral pH was used to rehydrate the lipid films at 60°C for 1hr. The solution was then sonicated to clarity to yield small, unilamellar vesicles (SUVs). The SUV suspension was incubated in PDMS wells on piranha-cleaned glass slides for 30 min at 60°C and allowed to cool to room temperature. In order to form bilayers labeled in the distal leaflet only, a solution of BODIPY-PC sonicated in buffer was incubated over bilayers formed without dye for 10 min. The PDMS wells were thoroughly rinsed, the excess water was removed, and the resulting bilayer was exposed to the desired relative humidity for imaging.

6.2.2 Bilayer Fabrication by Langmuir-Blodgett/Langmuir-Schäfer Transfer

Supported bilayers were also fabricated using the Langmuir-Blodgett/Langmuir-Schäfer (LB/LS) technique. Unlabeled DPPC was dissolved in chloroform and spread onto a 18MΩ water subphase in a Langmuir-Blodgett trough (Nima Type 611, Coventry, England). Two compression-expansion cycles were carried out before compressing the film to the desired surface pressure. Once compressed to the desired surface pressure the monolayer was allowed to equilibrate for 15 min before depositing onto a piranha-cleaned glass substrate in a headgroup down geometry. The monolayer on the subphase was then replaced with DPPC doped with 10^{-8} mol% BODIPY-PC. Following the same compression protocol, a second monolayer was deposited on the first using the Langmuir-Schäfer technique. The resulting bilayer was allowed to equilibrate for 10 minutes at the desired RH before imaging.

6.2.3 Imaging Approach

The bilayer films were imaged using a total internal reflection microscope (TIRF-M) (Olympus IX71, Center Valley, PA) equipped with a 100x objective (1.45 NA Achromat, Olympus). The 514 nm line from an argon ion laser (Coherent Innova 90, Santa Clara, CA) was directed through half-wave and quarter-wave plates (Newport, Irvine, CA) to control the polarization before being coupled into the microscope. P-polarized excitation was used and the fluorescence collected, filtered, and imaged on a cooled CCD camera (Cascade 650, Roper Scientific, Tuscon, AZ). To measure single molecule orientations, the optics were defocused ~500nm. Image collection was controlled by Slidebook software (Intelligent Imaging Innovations, Denver, CO) and analyzed using MATLAB (Natick, MA).

6.3 Results and Discussion

It has been previously shown that defocused single molecule emission measurements obtained with PTIRF-M can be used to track changes in lipid film structure at the molecular level.[15, 62] Using the reporter dye BODIPY-PC doped into DPPC films in trace amounts, it was shown that orientation changes in the membrane probe tracked changes in film surface pressure and the presence of film additives such

as cholesterol. These results showed that at both high surface pressures and high cholesterol content, single molecule emission patterns from BODIPY-PC doped into DPPC reflected a more ordered environment consistent with the condensing effects expected under these conditions. Here we expand these studies to probe the role that relative humidity (RH) has on supported model DPPC bilayers formed through vesicle fusion and the Langmuir-Blodgett/Langmuir-Schäfer (LB/LS) techniques.

6.3.1 Static Effects of Hydration on Membrane Structure

The top panel in Fig. 6.1 shows a typical single molecule emission image of a DPPC bilayer measured using defocused PTIRF-M. Each bright feature in the fluorescence image represents the emission from a single BODIPY-PC fluorescent lipid analog doped into the bilayer. The supported bilayer was formed using the LB/LS method, with each leaflet transferred at a surface pressure of 23 mN/m. This surface pressure has been shown previously to approximate the "equivalent surface pressure" for bilayers formed using the vesicle fusion method.[15, 68]

As others have shown, the distinct shapes observed in defocused single molecule P-TIRF images such as that in Fig. 6.1 reflect the orientation of each dye molecule.[52-55, 58-61, 68-70] Donut-like shapes arise from emission dipoles oriented normal to the membrane plane while more complicated patterns with wings are observed at larger tilt angles. These patterns can be analyzed to extract both the polar (Φ) and azimuthal (θ) angles of the emission dipole as shown schematically in the middle panel of Fig. 6.1. [52-55, 58-61, 68-70]

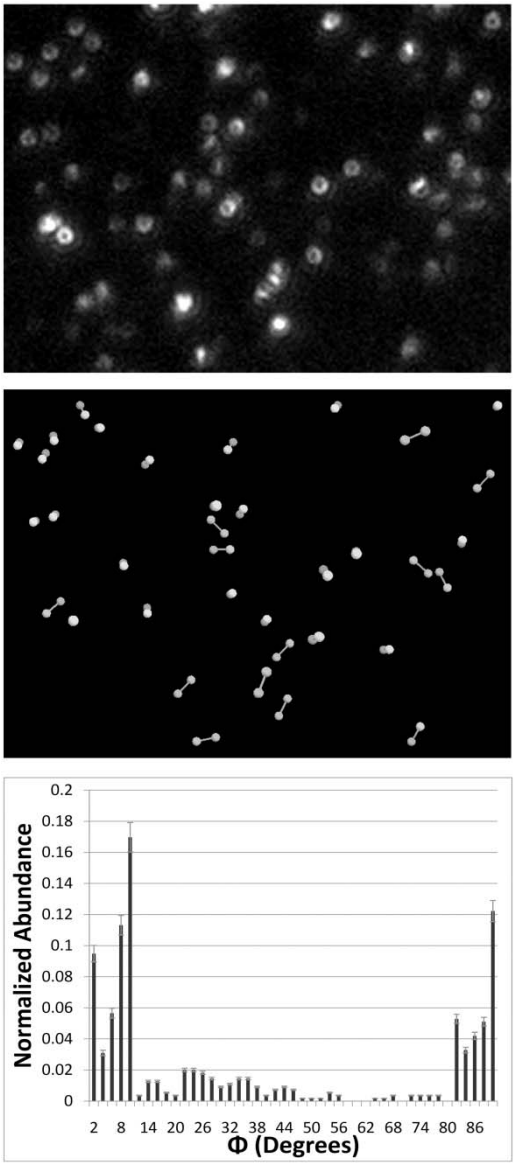

Figure 6.1: Top panel: Representative single molecule image of a DPPC bilayer transferred using the Langmuir-Blodgett/Langmuir-Schäfer technique at 23 mN/m and 13% relative humidity. Middle panel: Schematic diagram illustrating the three-dimensional orientation of emission dipoles collected from the image in the top panel. Bottom panel: Orientation histogram representing the polar angle distribution of 547 single molecule orientations collected at the stated conditions.

Analysis of 547 single molecule dipole orientations is used to develop the tilt angle (Φ) histogram shown in the bottom panel of Fig. 6.1. The polar or tilt angle of the emission dipoles away from the membrane normal is most sensitive to changes in membrane structure and will be used here to follow changes associated with increasing RH.[15, 62] The tilt angle histogram reveals a bimodal distribution with most of the population found in either in upright orientations (≤10^{o}) or lying nearly

parallel with the membrane surface (≥81^{o}). The population histogram in Fig. 6.1 reveals that 47% and 30% of the single molecule population are oriented normal (≤10^{o}) and parallel (≥81^{o}) with the membrane surface, respectively. The bimodal distribution likely reflects the well-known propensity of BODIPY-PC to insert into membranes with the chromophore oriented either along the acyl chains or bent back towards the headgroup.[71-76] It may also reflect the coexisting lipid phases present in these membranes. Regardless, previous studies have shown that the orientation distribution is sensitive to membrane surface pressure and the incorporation of membrane additives such as cholesterol, making single molecule orientations a sensitive marker of membrane structure.[15, 62]

The single molecule tilt angle distribution can be used to compare the effects of increasing RH as shown in Fig. 6.2. Figure 6.2 shows the results of single molecule measurements on LB/LS bilayers of DPPC doped with 10^{-8} mol% BODIPY-PC as a function of RH. For these measurements only the outer leaflet was doped with the BODIPY-PC reporter dye and both leaflets were transferred at a surface pressure of 23 mN/m. The left panels show representative single molecule emission measurements taken on supported LB/LS bilayers under conditions of 13%, 45%, 75%, and 95% relative humidity. The panels on the right display the corresponding population histograms generated from the analysis of individual single molecule emission patterns from over 500 molecules at each condition. At each RH, a minimum of three films were fabricated and measurements were taken in at least three different regions of interest to assure that the histograms reflect average properties of the films.

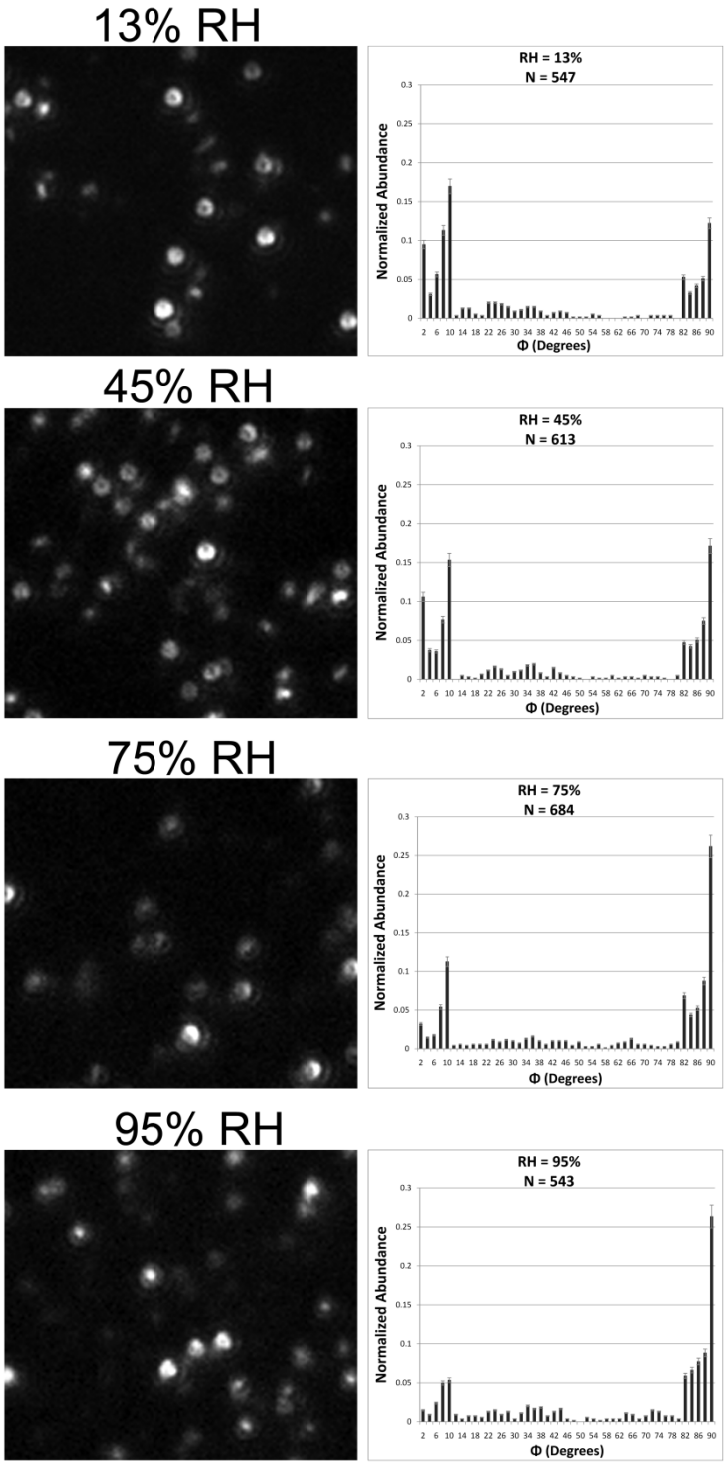

Figure 6.2: Left panel: Single molecule fluorescence images from DPPC bilayers obtained via LB/LS deposition at increasing hydration levels. Analysis of the fluorescence patterns collected is used to build up the histograms shown in the right panel. The histograms for each hydration level show an increase in emission dipoles oriented parallel to the membrane surface with increasing humidity, with a corresponding decrease in those oriented perpendicular to the membrane.

Figure 6.2 reveals a general trend in the single molecule orientations as a function of increasing RH that leads to a shift in population towards molecules oriented parallel to the membrane plane. As RH increases, a decrease in population of molecules oriented normal to the surface is observed that is correlated with a rise in population with those molecules oriented parallel to the membrane. At RH values of 13%, 45%, 75%, and 95% the population of molecules oriented normal to the membrane is 47, 41, 23, and 15%, respectively. This drop coincides with an increase in those oriented parallel to the surface of 30, 39, 51, and 55%, respectively. Interestingly, the percentage of molecules oriented between these extremes remains fairly constant at 23, 20, 25, and 28%, respectively.

As a comparison, Fig. 6.3 summarizes similar single molecule measurements taken on DPPC bilayers formed using the vesicle fusion method. For these measurements, the fluorescent lipid analog BODIPY-PC was doped into the outer leaflet at 10^{-8} mol%. These measurements, taken at the same RH values, reveal a similar dependence in the single molecule orientations with RH as bilayers formed using the LB/LS method (Fig. 6.2). At low relative humidity, the single molecule population histograms reveal a bimodal distribution with slightly more molecules oriented normal to the membrane plane than those parallel to the plane. At 13% RH, 42% are oriented with tilt angles between 0^{o} and 10^{o} while 35% are oriented with tilt angles between 81^{o} and 90^{o}. As RH increases, the number of molecules oriented normal to the membrane decreases while those oriented in the plane increases until finally at 95% RH, 15% are oriented normal and 64% are oriented parallel to the membrane plane.

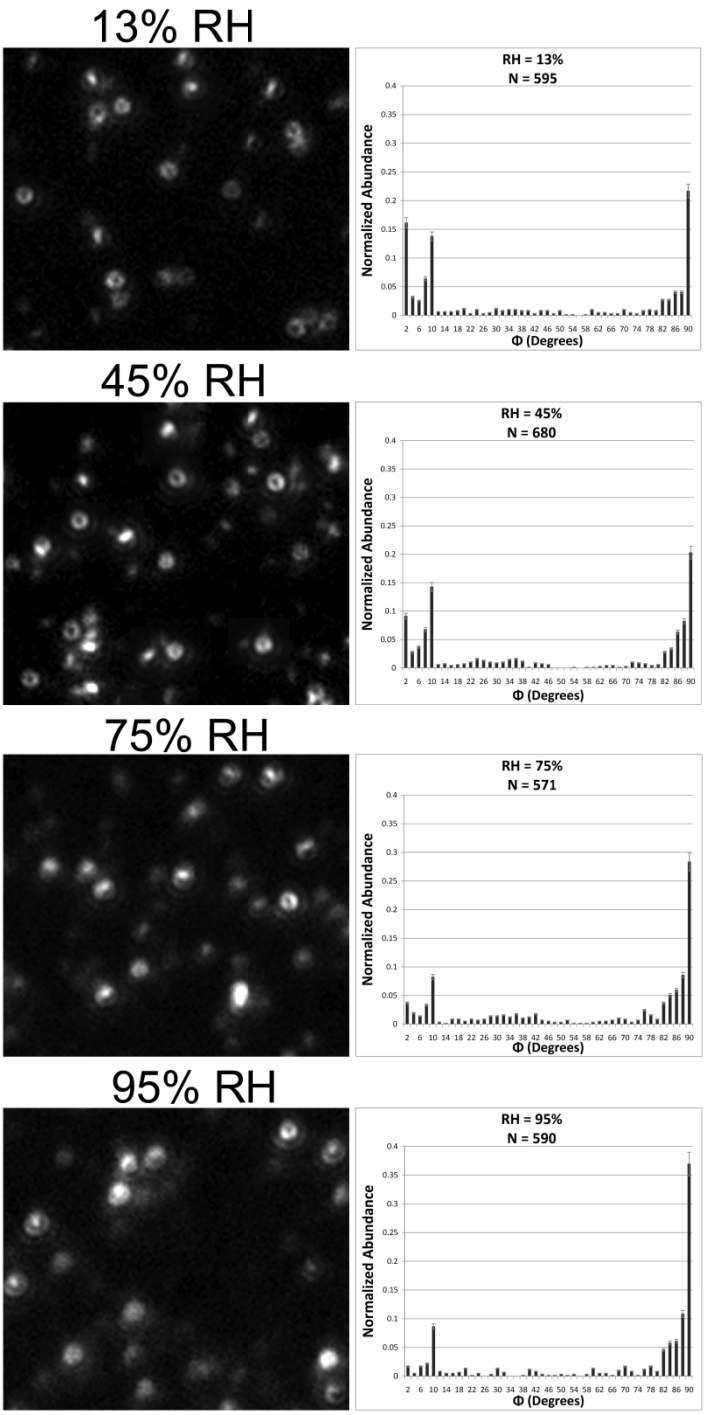

Figure 6.3: Similar single molecule fluorescence images as Fig. 6.2 obtained from DPPC bilayers formed by vesicle fusion and labeled in the distal leaflet. The histograms obtained from the analysis of a representative population of single molecule fluorescence patterns for each condition show a similar trend as those seen in LB/LS bilayers, with an increase in emission dipoles oriented parallel to the membrane as hydration is elevated. Emission dipoles oriented perpendicular to the membrane also follow a similar trend as those seen in the Langmuir method, decreasing as the activity of water is elevated.

A quantitative comparison between the RH dependence of bilayers formed using the LB/LS method (23 mN/m) and vesicle fusion can be seen in Fig. 6.4. The graph in Fig. 6.4 compares the population of BODIPY-PC dye molecules oriented normal to the surface as a function of RH for bilayers formed using the two methods. Also plotted in Fig. 6.4 are results for LB/LS bilayers transferred at a higher surface pressure of 40 mN/m. As seen in Fig. 6.4, for all bilayers the population of normal

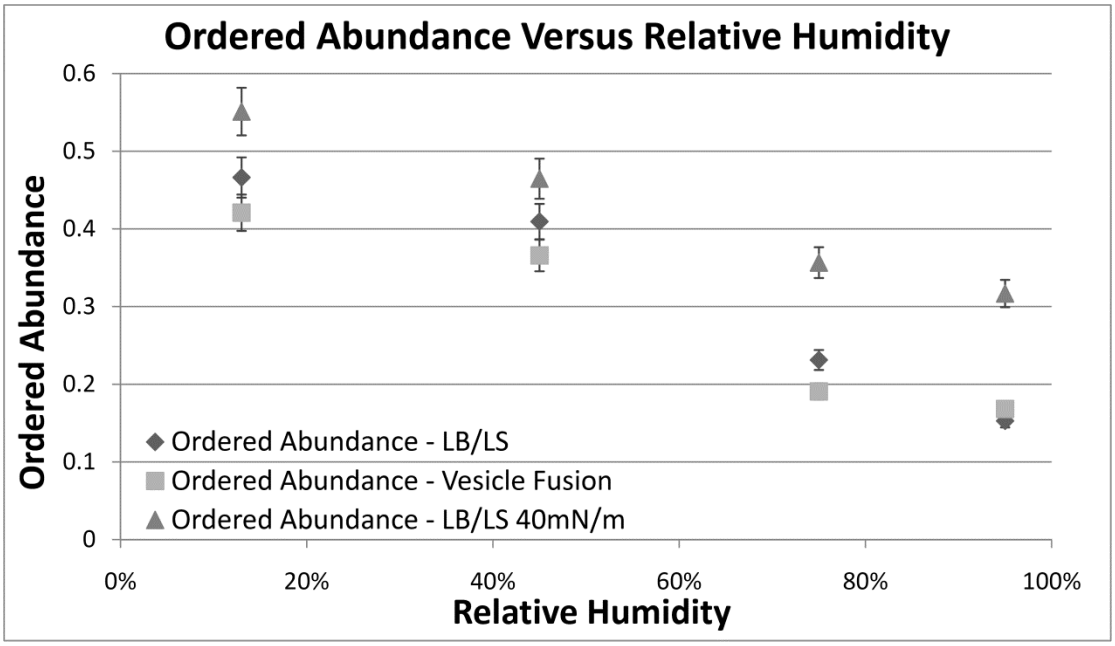

Figure 6.4: Comparison of the ordered abundance of emission dipoles at each bilayer condition studied, comprised of all emission dipoles oriented ≤10° with the membrane normal, including membranes formed by vesicle fusion and the LB/LS technique at 23 and 40 mN/m.

oriented fluorophores generally decreases as a function of increasing RH. The trends also reveal the close correspondence between bilayers formed from vesicle fusion and LB/LS bilayers transferred at 23 mN/m. The trend with RH for LB/LS bilayers transferred at 40 mN/m, however, clearly deviates from the others and is less sensitive to RH changes as expected for layers with higher lipid packing. The close agreement in trends seen in Fig. 6.4 for LB/LS bilayers transferred at 23 mN/m and those fabricated from vesicle fusion further supports the assignment of an "equivalent surface pressure" for membranes formed through vesicle rupture of ~23 mN/m.[15]

For all films studied, analysis of the single molecule emission patterns reveal an increasing population of large tilt angles associated with elevated RH. Previous studies have shown that headgroup hydration levels can strongly affect the lipid packing in supported lipid membranes which is consistent with the single molecule orientation trends.[27-28, 35-36, 39-40, 44-49, 77] As the water content of the membrane is increased, there is an increase in the apparent tilt angle of the BODIPY-PC probe, suggesting a relaxation of the acyl chains in the membrane.

At low RH, the dehydrated headgroups exhibit a reduced intermolecular distance, increasing pressure between each phospholipid. This elevated pressure causes a greater packing effect in the film. As water activity is increased with elevated humidity, the hydrated radius of the hydrophilic headgroups increases and a swelling effect occurs, raising the intermolecular distance in the film. This reduction in intermolecular pressure results in a relaxation of the acyl chains in the membrane which increases their tilt angle. These trends agree with those seen in the single molecule orientations shown in Fig. 6.2.

For the supported membranes studied here, we find negligible changes in the bulk distribution of the dye marker BODIPY-PC with RH. At high dye loading (0.25 mol % BODIPY-PC), plots of the dark, condensed phase regions of the membranes as a function of RH reveal negligible changes for all supported films studied (data not shown). These measurements show that large scale bulk rearrangements of the dye marker are not taking place as the RH increases. These results also show that the changes observed in the single molecule measurements reflect local changes taking place in the membranes which are not associated with large scale changes in dye location.

6.3.2 Dynamic Effects of Hydration on Supported DPPC Membranes

The single molecule measurements, however, do reveal that a small percentage of the individual dye molecules in the supported films do become laterally mobile as the RH increases. Figure 6.5 plots the percent of BODIPY-PC molecules that visibly translate in the films as a function of RH. As seen in the figure, the DPPC films studied exhibit an exponential increase in the population of BODIPY-PC molecules

that are mobile as RH increases. Even at the highest RH studied here, however, the population of translationally active molecules remains less than 6%. These trends are consistent with previous bulk measurements of diffusion made using fluorescence recovery after photobleaching (FRAP).[20, 33]

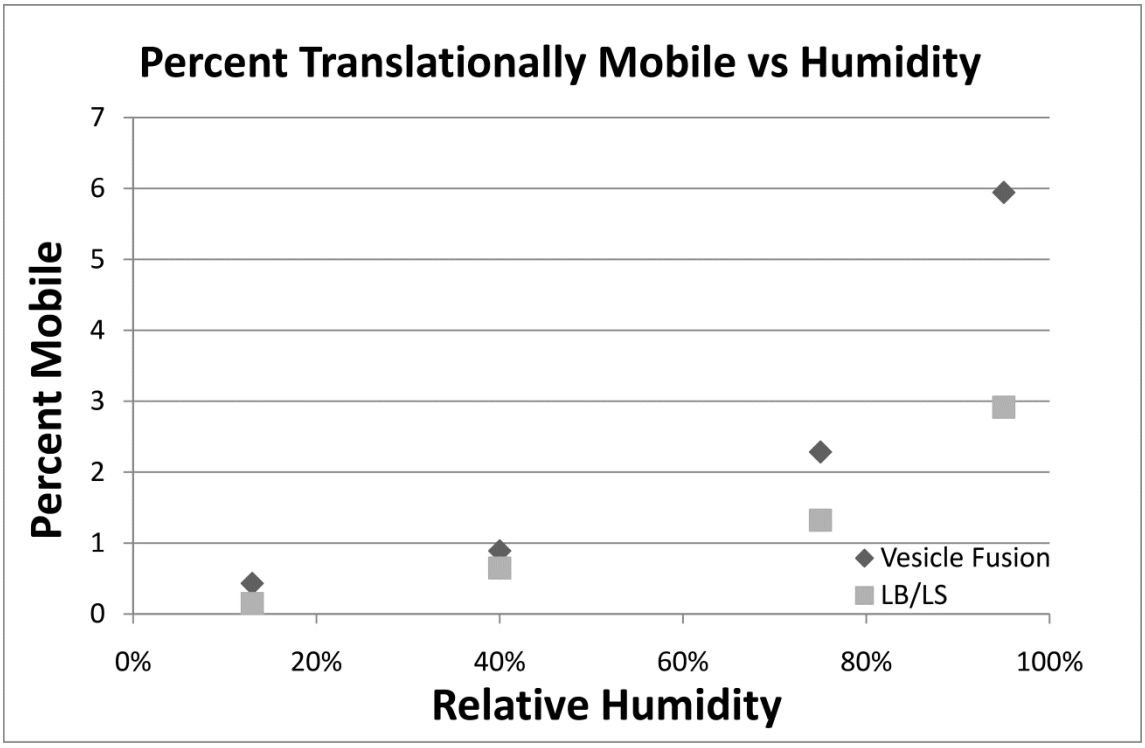

Figure 6.5: Comparison of the population of single molecule probes exhibiting lateral motion versus RH in bilayers formed by the LB/LS (23mN/m) and vesicle fusion methods. The population of single molecule probes laterally diffusing increases exponentially with relative humidity, reaching a maximum of ~6% for bilayers formed using vesicle fusion.

Baumgart and Offenhäusser used FRAP measurements to characterize the diffusion of the fluorescent analog NBD-PC in LB monolayers of DMPC and DphyPC as a function of RH.[20] Generally, they found an increase in diffusion with RH for monolayers transferred onto supported polymer cushions of chitosan or agarose and those deposited directly onto glass. When monolayers were deposited directly onto glass, however, the diffusion was dramatically reduced. Only at the highest RH levels studied were they able to resolve measurable diffusion signals above their detection threshold. This is consistent with the relatively small population of mobile molecules observed here in the single molecule measurements at low RH levels.

As discussed previously, the influence of RH on lateral diffusion is an activated process, with the height of the activation barrier linked to headgroup hydration and the properties of the specific surface and lipid. In general, at elevated RH levels where the headgroup is sufficiently hydrated, the lipid can overcome the electrostatic attraction with the surface and laterally diffuse. Therefore, as shown in Fig. 6.6, as RH increases the population of translationally active single molecules also increases.

In addition to the lateral movement of single molecules in the lipid films, polar and azimuthal angle dynamics can also be resolved in a small population of dye molecules. As an example, Fig. 6.7 shows a series of single molecule emission images taken from the same 5 μm x 6 μm region of a supported DPPC bilayer formed from vesicle fusion. Each sequential frame was collected using a 1 second integration time with the RH of the film held constant at 13%. Each frame shows 5 fluorescent features that arise from 5 BODIPY-PC molecules in the field of view. None of the fluorescent features change location from frame to frame showing that, within our spatial resolution, they are not diffusing. Moreover, all the molecules, with the exception of the one in the center marked by an arrow, have distinct emission shapes that do not evolve with time. This shows that their emission dipole orientation is not changing on this time scale. The single molecule emission feature in the center of the frames, however, is clearly changing shape from frame to frame reflecting changes in its orientation on the time scale of the experiment. The middle and bottom panels in Fig. 6.7 display the simulated emission pattern and schematic orientation, respectively, for the molecule in each frame.

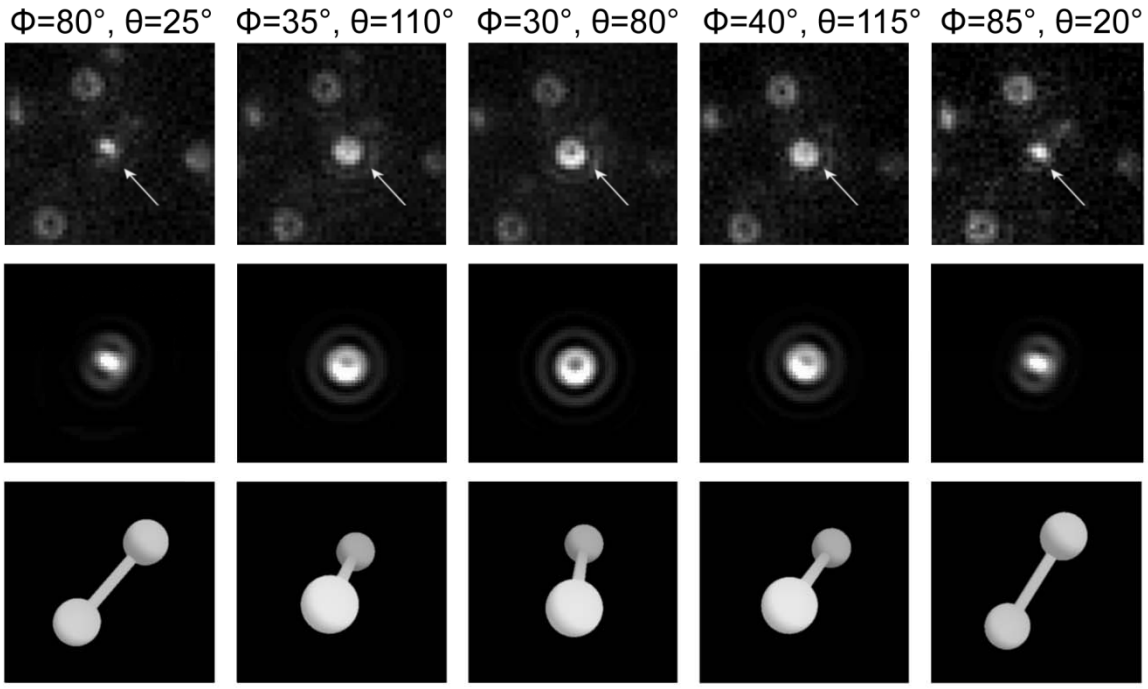

Figure 6.7: Top panel: Timelapse images of a 5 μm x 6 μm region in a DPPC bilayer formed by vesicle fusion at 13% RH at 1s integration time, with the corresponding polar (Φ) and azimuthal (θ) angles extracted from the fluorophore in the center. While the dye does not exhibit lateral movement through the capture, reorientation of the emission dipole is resolved and extracted. The middle panel shows the simulated emission pattern used to determine the three-dimensional orientation in each capture. A schematic illustration of the emission dipole orientation is displayed in the bottom panel.

This shows that even at low membrane hydration levels, acyl chain fluidity is at least partially maintained and may be detected in real time using the single molecule orientation measurements. As the RH is elevated further, the hydrodynamic radius of the headgroup becomes sufficient to overcome the activation barrier for diffusion and some lipids can laterally diffuse in the plane of the membrane. These results suggest that single molecule orientation measurements offer a minimally invasive view into membrane structure and dynamics that are complementary to other bulk measures of membrane properties.[20, 30, 33] One can envision measurements such as these providing further insight into biologically important processes such as membrane fusion. Membrane fusion is thought to proceed through localized dehydration events that may be reflected in changes in single molecule orientation and dynamics.[78-85]

6.4 Conclusions

Single molecule fluorescence measurements of BODIPY-PC doped into membranes in trace amounts have been used to probe the structure and dynamics of DPPC bilayers as a function of RH. Bilayers formed from vesicle fusion and the LB/LS method are compared and found to follow similar trends when the LB/LS bilayers are transferred at a surface pressure of 23 mN/m. This agrees with previous studies suggesting supported bilayers formed from vesicle fusion have an equivalent surface pressure of ~23 mN/m.[15] At all hydration levels studied, bimodal distributions of emission dipole orientations are observed which shifts as a function of RH. As the RH increases, the population of molecules oriented normal to the membrane plane decreases while the population lying in the plane increases. These shifts are consistent with an increase in the hydrated radius of the lipid headgroup as RH is elevated, increasing the area per lipid.

At all RHs studied, a small population of the BODIPY-PC dye molecules laterally diffuse in the membrane plane. The population of diffusing molecules increases exponentially with RH reaching a maximum of 6 % of the population at a RH of 95%. Even at low RH levels where lateral diffusion is rare, orientation dynamics can still be observed through changes in the single molecule emission pattern. Single molecule orientation measurements, therefore, are shown to be a complementary new technique for probing changes in both membrane structure and dynamics. Since only trace amounts of the fluorescent lipid probe are required, this approach introduces a minimal perturbation to the membranes under study. Moreover, since these are single molecule measurements, the method does not suffer from loss of information due to ensemble averaging that may complicate bulk measures of membrane properties. This seems especially useful for biological membranes that are characterized by their inherent heterogeneity.

These studies have validated the single-molecule technique for measuring orientations and probing molecular level structure. Now that the method is well-characterized, this approach can be

applied for determining antibody orientations as a function of immobilization protocol. Future studies will be directed toward gaining a better understanding of how immobilization protocol affects antibody orientation and how these processes may be optimized to provide maximal binding kinetics in immunosensor assays.

References

1. McConlogue, C. W.; Vanderlick, T. K., *Langmuir* **1997,** *13* (26), 7158-7164.
2. Hung, W. C.; Lee, M. T.; Chen, F. Y.; Huang, H. W., *Biophys. J.* **2007,** *92* (11), 3960-3967.
3. Johnston, L. J., *Langmuir* **2007,** *23* (11), 5886-5895.
4. Nakashima, H.; Furukawa, K.; Kashimura, Y.; Sumitomo, K.; Shinozaki, Y.; Torimitsu, K., *Langmuir* **2010,** *26* (15), 12716-12721.
5. Oreopoulos, J.; Epand, R. F.; Epand, R. M.; Yip, C. M., *Biophys. J.* **2010,** *98* (5), 815-823.
6. Hianik, T., *Acta. Phys. Slovaca* **2006,** *56* (6), 687-806.
7. Giocondi, M.-C.; Yamamoto, D.; Lesniewska, E.; Milhiet, P.-E.; Ando, T.; Le Grimellec, C., *Biochim. Biophys. Acta, Biomembr.* **2010,** *1798* (4), 703-718.
8. Henriksen, J.; Rowat, A. C.; Brief, E.; Hsueh, Y. W.; Thewalt, J. L.; Zuckermann, M. J.; Ipsen, J. H., *Biophys. J.* **2006,** *90* (5), 1639-1649.
9. Mouritsen, O. G.; Zuckermann, M. J., *Lipids* **2004,** *39* (11), 1101-1113.
10. Stottrup, B. L.; Keller, S. L., *Biophys. J.* **2006,** *90* (9), 3176-3183.
11. Braguglia, C. M., *Chem. Biochem. Eng. Q.* **1998,** *12* (4), 183-190.
12. Edmiston, P. L.; Lee, J. E.; Wood, L. L.; Saavedra, S. S., *J. Phys. Chem.* **1996,** *100* (2), 775-784.
13. Brosseau, C. L.; Leitch, J.; Bin, X.; Chen, M.; Roscoe, S. G.; Lipkowski, J., *Langmuir* **2008,** *24* (22), 13058-13067.
14. Simons, K.; Gerl, M. J., *Nat. Rev. Mol. Cell Biol.* **2010,** *11* (10), 688-699.
15. Livanec, P. W.; Huckabay, H. A.; Dunn, R. C., *J. Phys. Chem. B* **2009,** *113* (30), 10240-8.
16. Dickenson, N. E.; Armendariz, K. P.; Huckabay, H. A.; Livanec, P. W.; Dunn, R. C., *Anal. Bioanal. Chem.* **2010,** *396* (1), 31-43.
17. Miao, L.; Nielsen, M.; Thewalt, J.; Ipsen, J. H.; Bloom, M.; Zuckermann, M. J.; Mouritsen, O. G., *Biophys. J.* **2002,** *82* (3), 1429-1444.
18. Miersch, S.; Mutus, B., *Curr. Anal. Chem.* **2007,** *3* (1), 81-92.
19. Shaw, A. S., *Nat. Immunol.* **2006,** *7* (11), 1139-1142.
20. Baumgart, T.; Offenhauser, A., *Biophys. J.* **2002,** *83* (3), 1489-1500.
21. Goksu, E. I.; Hoopes, M. I.; Nellis, B. A.; Xing, C.; Faller, R.; Frank, C. W.; Risbud, S. H.; Satcher, J. H.; Longo, M. L., *Biochim. Biophys. Acta, Biomembr.* **2010,** *1798*, 719-729.
22. Scomparin, C.; Lecuyer, S.; Ferreira, M.; Charitat, T.; Tinland, B., *Eur. Phys. J. E: Soft Matter Biol. Phys.* **2009,** *28*, 211-220.
23. Tero, R.; Ujihara, T.; Urisu, T., *Proc. SPIE-Int. Soc. Opt. Eng.* **2007,** *6769*, 67690J/1-67690J/12.
24. Tanaka, M.; Sackmann, E., *Nature* **2005,** *437*, 656-663.
25. Liang, Q.; Chen, Q. H.; Ma, Y. G., *J. Phys. Chem. B* **2010,** *114* (16), 5359-5364.
26. Wong, J. Y.; Park, C. K.; Seitz, M.; Israelachvili, J., *Biophys. J.* **1999,** *77* (3), 1458-1468.
27. Binder, H., *Vib. Spectrosc.* **1999,** *21* (1-2), 151-163.
28. Smith, G. S.; Sirota, E. B.; Safinya, C. R.; Plano, R. J.; Clark, N. A., *J. Chem. Phys.* **1990,** *92* (7), 4519-4529.
29. Acosta, E. J.; Gitiafroz, R.; Zuo, Y. Y.; Policova, Z.; Cox, P. N.; Hair, M. L.; Neumann, A. W., *Resp. Physiol. Neurobi.* **2007,** *155* (3), 255-267.
30. Filippov, A.; Oradd, G.; Lindblom, G., *Langmuir* **2003,** *19* (16), 6397-6400.
31. Jendrasiak, G. L.; Smith, R. L.; Shaw, W., *Biochim. Biophys. Acta, Biomembr.* **1996,** *1279* (1), 63-69.
32. Lim, J. C.; Neuman, R. D.; Park, S., *Langmuir* **2002,** *18* (16), 6125-6132.
33. McCown, J. T.; Evans, E.; Diehl, S.; Wiles, H. C., *Biochemistry (Mosc).* **1981,** *20* (11), 3134-3138.
34. Parsegian, V. A.; Rand, R. P.; Colombo, M.; Rau, D. C., *Adv. Chem. Ser.* **1994,** *235*, 177-196.
35. Binder, H.; Gawrisch, K., *J. Phys. Chem. B* **2001,** *105* (49), 12378-12390.

36. Binder, H., *Appl. Spectrosc. Rev.* **2003,** *38* (1), 15-69.
37. Binder, H.; Pohle, W., *J. Phys. Chem. B* **2000,** *104* (50), 12039-12048.
38. Pohle, W.; Sass, M.; Selle, C.; Wolfrum, K.; Lobau, J., *Vib. Spectrosc.* **1999,** *19* (2), 321-327.
39. Kint, S.; Wermer, P. H.; Scherer, J. R., *J. Phys. Chem.* **1992,** *96* (1), 446-452.
40. Scherer, J. R.; Kint, S.; Bolton, B. A.; Bailey, G. F., *J. Mol. Struct.* **1990,** *224*, 245-257.
41. Janiak, M. J.; Small, D. M.; Shipley, G. G., *Biochemistry (Mosc).* **1976,** *15* (21), 4575-80.
42. Mansour, H. M.; Zografi, G., *J. Pharm. Sci.* **2007,** *96* (2), 377-396.
43. Ruocco, M. J.; Shipley, G. G., *Biochim. Biophys. Acta* **1982,** *691* (2), 309-320.
44. Katsaras, J., *Biochem. Cell Biol.* **1995,** *73* (5-6), 209-218.
45. Katsaras, J., *J. Phys. Chem.* **1995,** *99* (12), 4141-4147.
46. Katsaras, J.; Yang, D. S. C.; Epand, R. M., *Biophys. J.* **1992,** *63* (4), 1170-1175.
47. Sun, W. J.; Suter, R. M.; Knewtson, M. A.; Worthington, C. R.; Tristram-Nagle, S.; Zhang, R.; Nagle, J. F., *Phys. Rev. E* **1994,** *49* (5), 4665-4676.
48. Torbet, J.; Wilkins, M. H. F., *J. Theor. Biol.* **1976,** *62* (2), 447-458.
49. Tristram-Nagle, S.; Zhang, R.; Suter, R. M.; Worthington, C. R.; Sun, W. J.; Nagle, J. F., *Biophys. J.* **1993,** *64* (4), 1097-1109.
50. Wiener, M. C.; Suter, R. M.; Nagle, J. F., *Biophys. J.* **1989,** *55* (2), 315-325.
51. Tardieu, A.; Luzzati, V.; Reman, F. C., *J. Mol. Biol.* **1973,** *75* (4), 711-&.
52. Bartko, A. P.; Dickson, R. M., *J. Phys. Chem. B* **1999,** *103* (51), 11237-11241.
53. Bartko, A. P.; Dickson, R. M., *J. Phys. Chem. B* **1999,** *103* (16), 3053-3056.
54. Bohmer, M.; Enderlein, J., *J. Opt. Soc. Am. B: Opt. Phys.* **2003,** *20* (3), 554-559.
55. Dedecker, P.; Muls, B.; Deres, A.; Uji-i, H.; Hotta, J.-i.; Sliwa, M.; Soumillion, J.-P.; Müllen, K.; Enderlein, J.; Hofkens, J., *Adv. Mater.* **2009,** *21* (10-11), 1079-1090.
56. Forkey, J. N.; Quinlan, M. E.; Goldman, Y. E., *Biophys. J.* **2005,** *89* (2), 1261-1271.
57. Forkey, J. N.; Quinlan, M. E.; Shaw, M. A.; Corrie, J. E. T.; Goldman, Y. E., *Nature* **2003,** *422* (6930), 399-404.
58. Hellen, E. H.; Axelrod, D., *J. Opt. Soc. Am. B: Opt. Phys.* **1987,** *4* (3), 337-350.
59. Lieb, M. A.; Zavislan, J. M. Z.; Novotny, L., *Abstr. Pap. Am. Chem. S.* **2004,** *227*, U261-U261.
60. Patra, D.; Gregor, I.; Enderlein, J., *J. Phys. Chem. A* **2004,** *108* (33), 6836-6841.
61. Patra, D.; Gregor, I.; Enderlein, J.; Sauer, M., *Appl. Phys. Lett.* **2005,** *87* (10).
62. Livanec, P. W.; Dunn, R. C., *Langmuir* **2008,** *24* (24), 14066-73.
63. Oreopoulos, J.; Yip, C. M., *J. Struct. Biol.* **2009,** *168* (1), 21-36.
64. Oreopoulos, J.; Yip, C. M., *Biophys. J.* **2009,** *96* (5), 1970-1984.
65. Tronin, A.; Xu, T.; Blasie, J. K., *Langmuir* **2005,** *21* (17), 7760-7767.
66. Burns, A. R.; Frankel, D. J.; Buranda, T., *Biophys. J.* **2005,** *89* (2), 1081-1093.
67. Cruz, A.; Vazquez, L.; Velez, M.; Perez-Gil, J., *Langmuir* **2005,** *21* (12), 5349-5355.
68. Toprak, E.; Enderlein, J.; Syed, S.; McKinney, S. A.; Petschek, R. G.; Ha, T.; Goldman, Y. E.; Selvin, P. R., *Proc. Natl. Acad. Sci.* **2006,** *103* (17), 6495-6499.
69. Toprak, E.; Enderlein, J.; Mckinney, S. A.; Syed, S.; Petschek, R. G.; Ha, T.; Goldman, Y. E.; Selvin, P. R., *Biophys. J.* **2005,** *88* (1), 664a.
70. Uji-i, H.; Deres, A.; Muls, B.; Melnikov, S.; Enderlein, J.; Hofkens, J., In *Fluorescence of Supermolecules, Polymers, and Nanosystems*, Springer: New York, 2008; pp 257-284.
71. Boldyrev, I. A.; Zhai, X.; Momsen, M. M.; Brockman, H. L.; Brown, R. E.; Molotkovsky, J. G., *J. Lipid Res.* **2007,** *48* (7), 1518-32.
72. Boldytev, I. A.; Molotkovsky, I. G., *Bioorg. Khim.* **2006,** *32* (1), 87-92.
73. Kaiser, R. D.; London, E., *Biochim. Biophys. Acta* **1998,** *1375* (1-2), 13-22.
74. Menger, F. M.; Keiper, J. S.; Caran, K. L., *J. Am. Chem. Soc.* **2002,** *124* (40), 11842-11843.

75. Omel'kov, A. V.; Pavlova, Y. B.; Boldyrev, I. A.; Molotkovsky, J. G., *Russ. J. Bioorg. Chem.* **2007,** *33* (5), 505-510.
76. Sachl, R.; Boldyrev, I.; Johansson, L. B. A., *Phys. Chem. Chem. Phys.* **2010,** *12* (23), 6027-6034.
77. Birrell, G. B.; Griffith, O. H., *Arch. Biochem. Biophys.* **1976,** *172* (2), 455-462.
78. Cevc, G.; Richardsen, H., *Adv. Drug Del. Rev.* **1999,** *38* (3), 207-232.
79. Cho, S. J.; Kelly, M.; Rognlien, K. T.; Cho, J. A.; Horber, J. K. H.; Jena, B. P., *Biophys. J.* **2002,** *83* (5), 2522-2527.
80. Furber, K. L.; Churchward, M. A.; Rogasevskaia, T. R.; Coorssen, J. R., In *Mechanisms of Exocytosis*, 2009; Vol. 1152, pp 121-134.
81. Jeremic, A., Cho, W.J., Jena, B.P., *J. Biol. Phys. Chem.* **2004,** *4*, 4.
82. Jeremic, A.; Kelly, M.; Cho, J. A.; Cho, S. J.; Horber, J. K. H.; Jena, B. P., *Cell Biol. Int.* **2004,** *28* (1), 19-31.
83. Leabu, M., *J. Cell. Mol. Med.* **2006,** *10* (2), 423-427.
84. Potoff, J. J.; Issa, Z.; Manke, C. W.; Jena, B. P., *Cell Biol. Int.* **2008,** *32* (4), 361-366.
85. Wheatley, D., *Cell Biol. Int.* **2008,** *32* (4), 359-360.

Chapter 7: Future Directions

7.1 Introduction

Through the studies discussed in Chapters 5 and 6, a single-molecule fluorescence orientation method has been adapted to examine well-characterized model membrane systems. These test systems assisted in further characterizing the technique while at the same providing insight into heterogeneous lipid film structure at the molecular level. The next step for this work is to utilize the single-molecule approach to monitor the effect that different preparation chemistries have on the orientations of immobilized antibodies. Understanding the effects of immobilization protocols on antibody orientation and capture efficiency is paramount for improving sensor performance.

Sensing performance may also be improved by using a shorter wavelength excitation in the WGM approach. Evidence suggests that shorter wavelengths will reduce the mode volume of the confined field and subsequently increase sensitivity to analyte binding on the WGM resonator. In addition, dye loading, functionalization chemistry, and substrate properties are all known to influence resonator Q-factors, and each property should be examined to improve sensor performance.

7.2 Characterization of the Orientation and Function of Surface Immobilized Antibodies

Having tested and validated the single-molecule orientation approach, this approach can now be extended to measure the effect of immobilization protocol on antibody orientation.

7.2.1 Antibody Binding to Fluorophore Probe for Direct Orientation Measurement

Initial work to determine absolute antibody orientation has begun using the antibody 4-4-20 as the model system. This antibody has a strong binding affinity towards flourescein and will therefore be useful for probing the bound complex by measuring single molecule orientations.[2-7] An advantage to using this as the model system is that the 4-4-20 antibody is readily available for purchase and has been studied extensively.[4, 5] Moreover, it belongs to the IgG class of antibodies, which are the most abundant

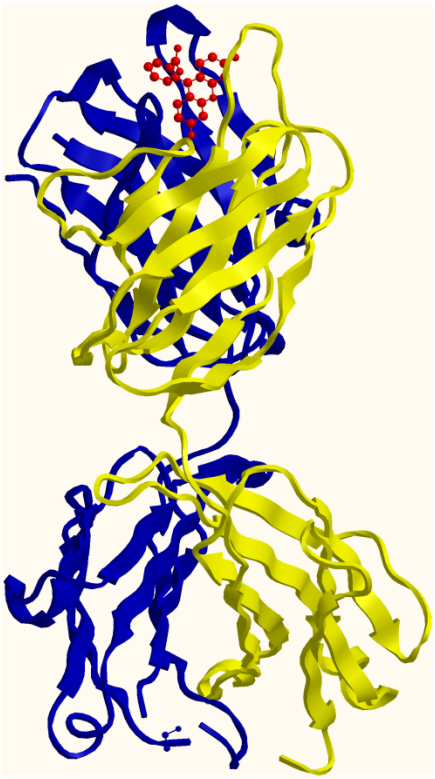

Figure 7.1: Ribbon view of the fluorescein/4-4-20 Fab complex. The heavy chain is highlighted blue and the light chain is colored yellow.[4, 5]

class in serum, making these measurements relevant to commonly employed immunoassays. This makes the 4-4-20 system an excellent model system for exploring immobilization methods, which can then be applied to future WGMI preparation protocols.

Figure 7.1 displays the crystal structure of the fluorescein-Fab complex of 4-4-20 showing the fluorescein immobilized by surrounding protein interactions.[4, 5] Having the crystal structure on hand will assist in interpreting the resulting data, as the exact orientation of the binding site is known. One complication of this work is that the florescein is quenched ~95% when complexed with the antibody due to nearby aromatic residues.[2, 3] This would make single-molecule measurements problematic given the reduced emission. Fortunately, the 4-4-20 monoclonal antibody raised against flourescein is known to cross-react with dyes of similar structure, which have shown reduced quenching following binding.[8] One potential marker is Fluo-3, which exhibits <32% quenching while bound thus enabling single

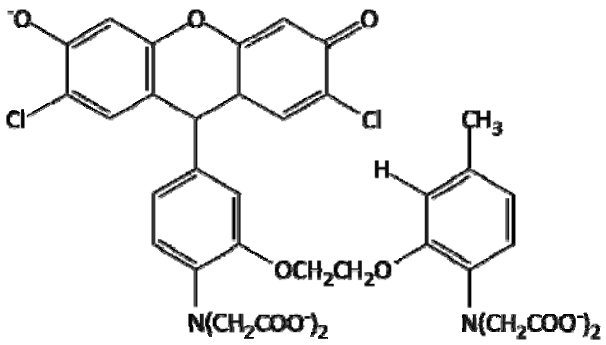

Figure 7.2: Chemical structure of the Fluo-3 fluorescent dye.

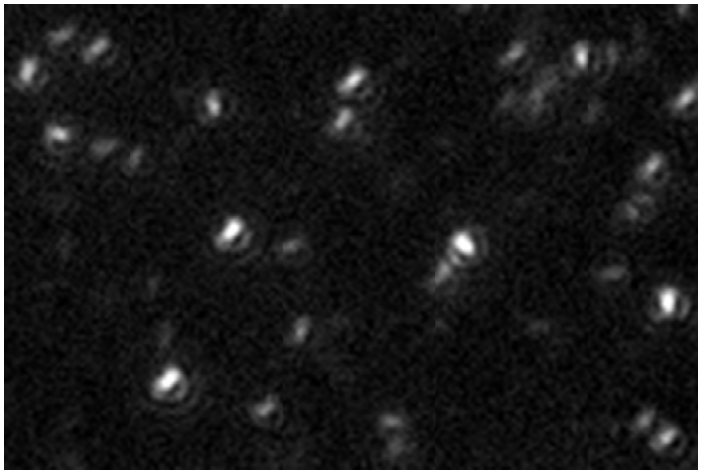

Figure 7.3: A defocused PTIRF-M single-molecule image of the Fluo-3 reporter molecule displaying orientation-specific emission patterns.[1]

molecule fluorescence measurements. The structure of this reporter molecule is shown in Fig. 7.2. Initial experiments on Fluo-3 alone indicate that this is an excellent probe for single molecule orientation studies. Figure 7.3 shows single molecule fluorescence measurements on Fluo-3 molecules dispersed on a glass substrate.[1] The dye exhibits excellent single molecule signal-to-noise levels and favorable photobleaching characteristics, enabling orientation measurements. Future studies with the 4-4-20/Fluo-3 complex will include the exploration of various antibody immobilization techniques starting with the nonspecific adsorption method. After tightly binding the reporter molecule, the resulting orientation of the fluorophore will be used as an indicator of the orientation of the complex. A schematic representation of what these results may look like is shown in Figure 7.4.

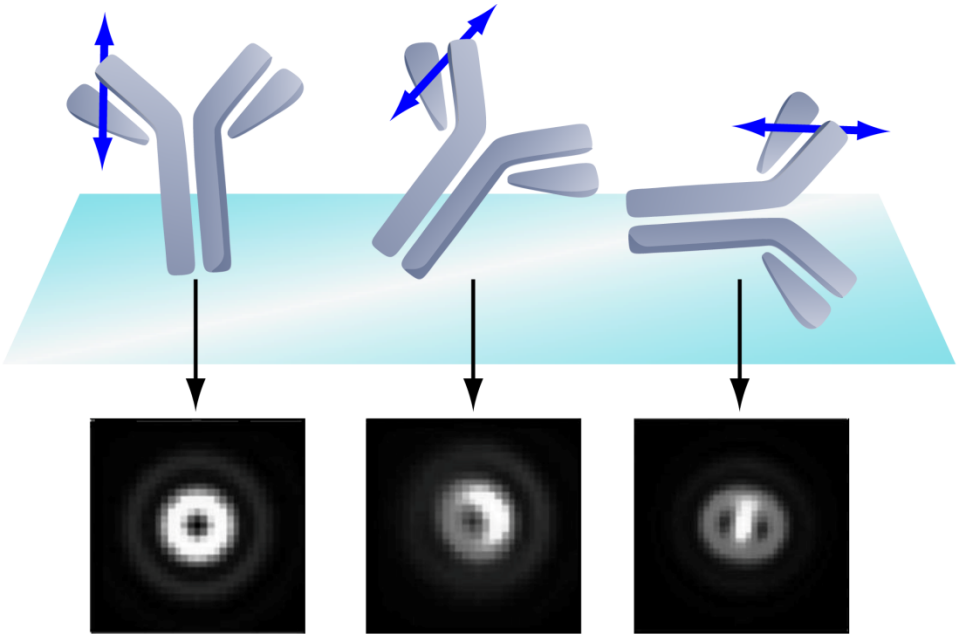

Figure 7.4: Schematic representation of the 4-4-20/Fluo-3 complex in various orientations and the resulting single molecule fluorescence emission patterns. The emission dipole of the reporter is indicated by the blue double arrow.

This technique will be used to examine various immobilization strategies to determine their effect on antibody binding efficiency and orientation. The advantage to this approach is that the reporter molecule used for antibody measurement is bound by the immunogen. An absence of fluorescence after immobilization chemistry will therefore indicate antibody denaturation. This advantage will allow us to not only determine the absolute orientation of bound antibodies as a function of immobilization protocol, but also distinguish between techniques that result in loss of biomolecule function due to denaturing conditions. Using this information, we will employ the functionalization techniques found to be most efficient in our whispering gallery sensors to assist in maximizing sensor performance.

7.3 Additional Experiments to Improve Sensor Performance

In addition to exploring optimal antibody immobilization protocols, sensing performance can be improved through modifications that alter the mode volume and increase Q. This section discusses some of these strategies and how they may increase analytical performance of the WGMI approach.

7.3.1 Mode Volume Reduction

One major difference between our WGM measurements and previous work in WGM detection revolves around the excitation wavelength employed. The tunable laser used in this work is centered at 633 nm, however most studies in this field utilize longer wavelengths for WGM excitation, ranging from 980-1550 nm.[9-14] Our approach leads to a significant reduction in the resonator mode volume which may be responsible for the enhanced sensitivity discussed in Chapter 2. The mode volume (*V*) for a spherical resonator as estimated by Matsko and Ilchenko is:[15]

$$V = 3.4 * \pi^{3/2} \left(\frac{\lambda}{2\pi n}\right)^3 * \nu^{11/6}\sqrt{\nu - m + 1} \qquad \text{Eq. 7.1}$$

where ν is the angular momentum number for a sphere, n is the refractive index, m is the mode number, and λ is the wavelength confined within the resonator. What is important to note in this equation is the cubed dependence of mode volume on the excitation wavelength. As this wavelength decreases, therefore, a significant reduction in the mode volume is observed. Armani et al. has reported that the resonant wavelength shift experienced by optical resonators has an inverse dependence on the mode volume.[16] This suggests that small decreases in excitation wavelength, therefore, can have a significant effect on sensor response.

Future work will explore this effect using identical immunoassay procedures as performed in previous chapters while measuring resonant wavelength changes with spectrally separated excitation sources. If the increase in sensor response is significant as expected, this provides a straightforward approach for substantially improving WGM sensitivity and detection limits.

7.3.2 Dye Loading Effects on Q-Factor

An inherent issue that limits the resonator Q-factor in the WGMI design is that the microspheres are functionalized with a fluorescent dye. Light stored within the resonator cavity experiences an additional loss due to absorption by the bound fluorophore. In the case of labeled resonators the

dependence of Q-factor on material attenuation, Q_{mat} becomes more important. The relationship is given by Eq. 7.2:[17]

$$Q_{mat} = \frac{2\pi n}{\alpha\lambda} \quad \text{Eq. 7.2}$$

where n is the refractive index of the resonator, α is the material attenuation, and λ is the wavelength supported within the cavity. Normally, this attenuation is only dependent on the resonator material, however the introduction of a fluorescent dye will increase these effects. Since the current fluorescence signals obtained from the microsphere resonators are more than sufficient to characterize a resonance (S/N ranges from 5-50), a reduction in dye loading could assist in increasing the Q-factor and improving sensor performance.

7.4 Summary

We have demonstrated in chapters 2 & 3 that the WGM technique can be utilized for refractive index measurements and biomarker measurement in both buffered systems and clinical human sera. With the current design, the WGMI technique has already exhibited detection limits in human serum that are improved over traditional ELISA methods (~2 U/mL CA-125 using WGMI versus ~5 U/mL using ELISA). Using the studies performed on optimizing antibody orientations and combining these efforts with reduced mode volume and minimized dye loading to increase resonator performance, we hope to improve these detection limits even further for a highly sensitive, multiplexed assay for biomarker detection.

References

1. Armendariz, K. P., Unpublished data.
2. Watt, R. M.; Voss, E. W., Jr., *Immunochemistry* **1977,** *14*, 533-41.
3. Kranz, D. M.; Herron, J. N.; Voss, E. W., Jr., *J. Biol. Chem.* **1982,** *257*, 6987-95.
4. Herron, J. N.; He, X. M.; Mason, M. L.; Voss, E. W., Jr.; Edmundson, A. B., *Proteins: Struct., Funct., Genet.* **1989,** *5*, 271-80.
5. Whitlow, M.; Howard, A. J.; Wood, J. F.; Voss, E. W., Jr.; Hardman, K. D., *Protein Eng.* **1995,** *8*, 749-61.
6. Wei, A.-P.; Herron, J. N., *J. Mol. Recognit.* **2002,** *15*, 311-320.
7. Midelfort, K. S.; Hernandez, H. H.; Lippow, S. M.; Tidor, B.; Drennan, C. L.; Wittrup, K. D., *J. Mol. Biol.* **2004,** *343*, 685-701.
8. Swindlehurst, C. A.; Voss, E. W., *Biophys J* **1991,** *59* (3), 619-628.
9. Hanumegowda, N. M.; Stica, C. J.; Patel, B. C.; White, I.; Fan, X., *Appl. Phys. Lett.* **2005,** *87* (20), 201107.
10. Hanumegowda, N. M.; White, I. M.; Fan, X., *Sensor. Actuat. B-Chem.* **2006,** *120* (1), 207-212.
11. Hanumegowda, N. M.; White, I. M.; Oveys, H.; Fan, X., *Sens. Lett.* **2005,** *3*, 315-319.
12. Washburn, A. L.; Gunn, L. C.; Bailey, R. C., *Anal. Chem.* **2009,** *81* (22), 9499-9506.
13. Washburn, A. L.; Luchansky, M. S.; Bowman, A. L.; Bailey, R. C., *Anal. Chem.* **2009,** *82* (1), 69-72.
14. Zhu, H.; Suter, J.; White, I.; Fan, X., *Sensors* **2006,** *6* (8), 785-795.
15. Matsko, A. B.; Ilchenko, V. S., *IEEE J. Sel. Top. Quant.* **2006,** *12* (1), 3-14.
16. Armani, A. M.; Kulkarni, R. P.; Fraser, S. E.; Flagan, R. C.; Vahala, K. J., *Science* **2007,** *317* (5839), 783-787.
17. Gorodetsky, M. L.; Savchenkov, A. A.; Ilchenko, V. S., *Opt. Lett.* **1996,** *21* (7), 453-455.